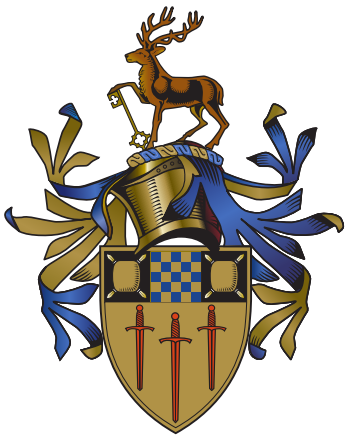

The Resolution of the CLAS12 Reconstruction Software

Adrian Saina,
Department of Physics, University of Surrey, Guildford, Surrey, GU2 7XH

submitted to the University of Surrey in partial fulfilment of the degree in Master of Physics

January, 2021

Abstract

The Thomas Jefferson National Accelerator Facility is a US National Laboratory located in Newport News, Virginia. Two linear accelerators accelerate electrons to 12 GeV and researchers in four research halls study the dynamics of quarks and gluons in nuclei by scattering the electrons off various targets. The CEBAF Large Acceptance Spectrometer at 12 GeV (CLAS12) in Hall B is a mass spectrometer capable of detecting both charged and neutral particles over a large fraction of the full solid angle. The data that is produced by the subsystems of CLAS12 is processed by the CLAS12 Analysis and Reconstruction Architecture, CLARA. The processed signals from different detectors are matched together into a trajectory through CLAS12: this is referred to as a reconstructed event. The aim of this study was to obtain the resolution of the event reconstruction software in simulation. To compute the resolutions, simulated and reconstructed track parameters of the beam particles were used as starting points and directions for a particle swimmer, a software package that uses numerical integration to propagate particles through the CLAS12 magnetic fields. The two tracks were propagated to the surfaces of the subsystems comprising the CLAS12 Forward Detector. The differences in positions and angles of the two tracks at the detector surfaces were computed and plotted in histograms. The histograms were then fitted, with the width of the fit functions being a measure of the resolutions. The dependence of the resolutions on particle species and energy, the torus field polarity and the detector geometry was investigated, along with the effects of the new version of the simulation software. The resolution calculations will provide benchmark values when future upgrades are made to the software and hardware elements of the reconstruction chain. Additionally, the obtained results can be used to initialize the covariance matrix that calculates measurement uncertainties in the Kalman Filter tracking process in the Drift Chambers.

Declaration

This dissertation and the work to which it refers are the results of my own efforts. Any ideas, data, images or text resulting from the work of others (whether published or unpublished) are fully identified as such within the work and attributed to their originator in the text, bibliography or in footnotes. This dissertation has not been submitted in whole or in part for any other academic degree or professional qualification. I agree that the University has the right to submit my work to the plagiarism detection service TurnitinUK for originality checks. I own the copyrights.

Adrian Saina

Acknowledgements

I would like to thank my mentor, Professor Gerard Gilfoyle, for all the support and guidance that he provided during the course of this research year. I would also like to thank Dr. Veronique Ziegler, my supervisor at Jefferson Lab who devised this project and provided valuable input that helped complete this study. Lastly, I would like to express my gratitude to all the members of the CLAS Collaboration, especially the members of the Software Working Group who were very helpful in giving advice and suggestions whenever it was needed.

Abbreviations

CEBAF	The Continuous Electron Beam Accelerator Facility
GPDs	Generalized Parton Distributions
CLAS12	The CEBAF Large Acceptance Spectrometer at 12 GeV
HTCC	High Threshold Cherenkov Counter
PMT	Photomultiplier Tube
DCs	Drift Chambers
FTOF	Forward Time-Of-Flight system
PCAL	Pre-shower Calorimeter
EC	Electromagnetic Calorimeter
HBT	Hit-Based Tracking
COATJAVA	The CLAS Offline Analysis Tools
CLARA	The CLAS Analysis and Reconstruction Architecture
CCDB	Calibration Constants Database
GEMC	The Geant4 Monte Carlo Software
Geant4	Geometry and Tracking
CED	CLAS Event Display
TSCS	Tilted Sector Coordinate System
RGA	Run Group A
RGB	Run Group B
TDCs	Time-to-Digital Converters
DOCA	Distance Of Closest Approach

Contents

Chapter 1

Introduction

1.1 The History of Jefferson Lab

The Thomas Jefferson National Accelerator Facility, referred to as JLab, is a US National Laboratory situated in Newport News, Virginia. Researchers in four research halls study the quark-gluon structure of nucleons by observing the products of electron scatterings. The facility operates with a continuous electron beam and the halls feature detectors that track both charged and neutral particles at a rate of over a thousand events per second. The facility was built in the aftermath of the discovery of quarks at the Stanford Linear Accelerator [1][2]. The construction was completed in 1994 and the scientific program started with the delivery of the first beam to the experimental halls [3][4]. Some of the more interesting experiments conducted during the 6 GeV era studied the EMC effect [5], the excitation amplitudes of nuclear resonances [6][7], nucleon structure functions [8], the form factors of the nucleon and more [9][10][11]. After 178 completed experiments, the lab ceased operations in 2012 as the installation of the 12 GeV upgrade began. The upgrade was completed and the four halls started performing experiments again in 2018. An experiment in Hall A that was recently completed and presented measured the neutral weak form factor of lead [12]. When an electron interacts weakly with a lead nucleus at a small momentum transfer of scattering, the Z^0 boson emitted by the beam electrons couples primarily to neutrons that form a skin on the surface of the nucleus [13]. If polarized electrons are scattered off lead nuclei and the electron helicity is varied, the projection of their spin onto the direction of momentum, there will be an inequality in the cross sections of electrons that scatter on either side of the target [12]. The parity-violating asymmetry is acquired from the two measured cross sections, and the thickness of the neutron skin on the surface of the nucleus can be obtained from this asymmetry [12]. This neutron skin thickness can be used to constrain properties of rich nuclear matter such as the radii of neutron stars and the baryon density of the lead nucleus

[12]. An experiment that was most recently conducted at Hall B, the hall that offers research opportunities for Surrey students, was the Bonus12 experiment [14]. This experiment attempts to measure the free neutron structure function at large values of Bjorken x, the fraction of the nucleon momentum carried by the struck quark [14]. The structure function was measured by scattering electrons off neutrons in deuterium. The scattered electrons were measured with the Forward Detector, and the recoiled protons that are spectators of the reaction and scatter at backward angles with low momentum were detected with a radial time projection chamber [14]. The kinematics of the neutron are obtained from the observation of the proton. The low momentum and backward scattering angles of spectators allows researchers to obtain structure functions for free neutrons while minimizing uncertainties such as off-shell effects (binding modifies the structure functions of the nucleons in nuclei) and final state interactions (struck neutron interacts with spectator proton) [14]. Additionally, these structure functions shed light on neutron form factors, on the u and d quark distribution ratio and on quark-hadron duality [15].

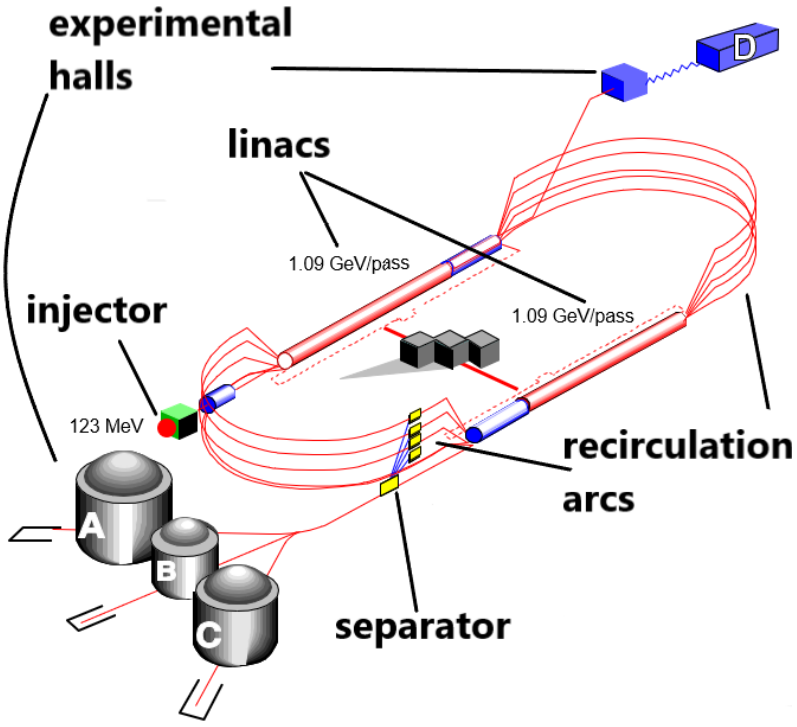

Figure 1.1: A visual representation of the injector, the linear accelerators (linacs), recirculation arcs and the research halls at Jefferson Lab. Picture adopted from [16] and edited.

1.2 Accelerator overview

The continuous wave recirculating electron accelerator at the CEBAF facility delivers an 11 GeV beam to four research halls: A, B, C, and D. The electrons are produced in the injector (Figure 1.1) by illuminating polarized laser light of $\lambda = 780$ nm on a Gallium-Arsenide semiconductor, which emits bunches of electrons that are spin-polarized up to $\sim 85\%$ by photoemission [17]. Four lasers produce beam electrons destined for the four halls, and the electrons form interleaved bunches before they're injected into the accelerator. The two linear accelerators (linacs, shown in Figure 1.1) accelerate electrons with Superconducting Radio Frequency cavities [4][18]. The beam gets accelerated by an oscillating electric field within the cavities. In order to accelerate each electron that enters the cavity, the field oscillates at a frequency that's equal to the frequency of the incoming beam electrons [18]. As the beam exits a linac, it encounters the spreader that deflects electrons in recirculation arcs according to their momentum (Figure 1.1). At the fifth pass around the accelerator, a separator separates the beam destined for Hall D and directs it for an additional pass through the North linac. The interleaved beam destined for halls A-C enters the extraction region where the beam electrons are guided to their destined halls with magnets.

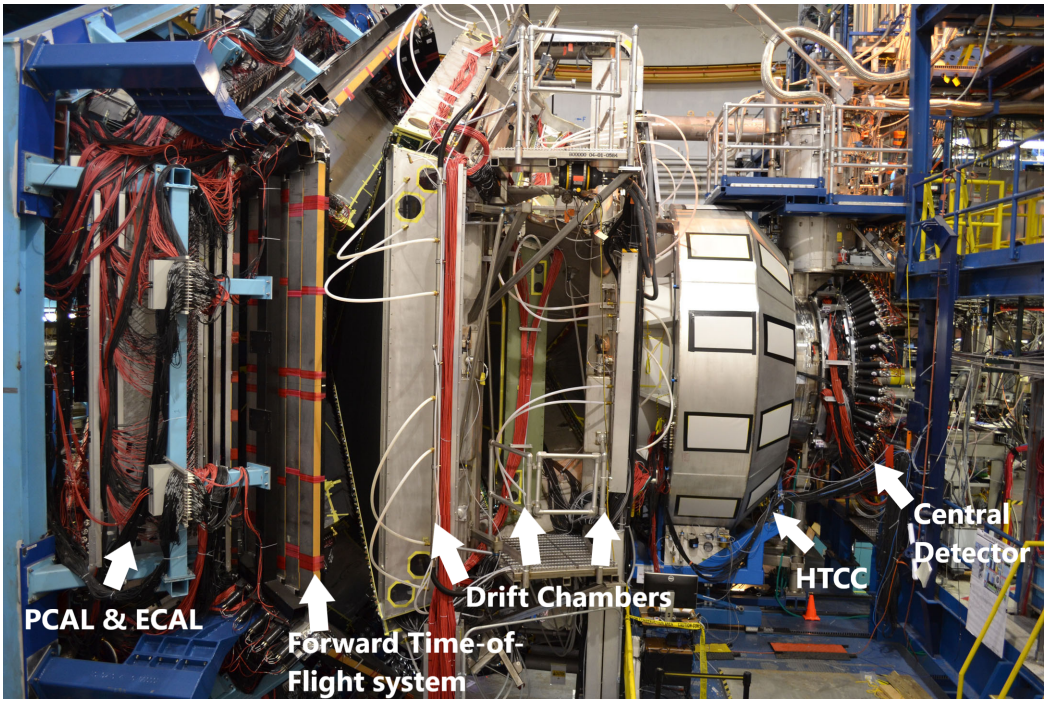

Figure 1.2: The entire CLAS12 detector. The beam is incident from the right onto the target, located within the Central Detector. Picture adopted from [19] and edited.

1.3 Overview of the CLAS12 Detector

Hall B at Jefferson Lab houses the CEBAF Large Acceptance Spectrometer at 12 GeV, CLAS12 (Figure 1.2) [19]. The detector tracks both charged and neutral particles over a large fraction of the full solid angle, allowing the researchers to capture almost all of the scattering products. The detector consists of two sub-detectors built around two superconducting magnets, the torus and solenoid [20]. The solenoid is placed at the center, surrounding the target. It deflects particles with low recoil momentum that scatter at $40° < \theta < 135°$ [20]. The momentum of charged particles is obtained from the amount of deflection in the magnetic field. The Central Detector is placed around the target to map trajectories of particles that are deflected by the solenoid [19]. It's shown in Figure 1.3. It provides coverage over the full range of the azimuthal angle.

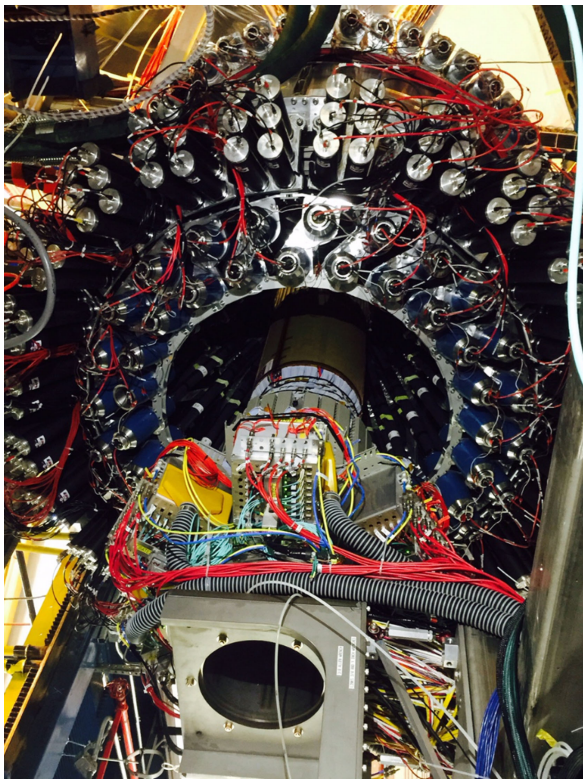

Figure 1.3: The CLAS12 Central Detector. The Central Vertex Tracker is retracted from its position for a better view. Around it are the two rings of PMTs and light guides of the Central-Time-of-Flight System, while the three outermost rings of PMTs are from the Central Neutron Detector. Picture adopted from [19].

Tracking is provided by the Central Vertex Tracker, which has 12 active detection layers that are separated into two subsystems: the Silicon Vertex Tracker and the

Barrel Micromegas Tracker [21][22]. The Central Time-of-Flight detector identifies particles from flight time measurements, it achieves a time resolution of $\sigma_t = 80$ ps [23]. The Central Neutron Detector detects low momentum neutrons by measuring their time of flight with scintillator paddles that achieve a resolution of $\sigma_t = 150$ ps, which allows up to 10% neutron detection efficiency [24]. The Back Angle Neutron Detector extends the ability to detect neutrons to polar angles $155° < \theta < 175°$ [19].

The torus magnet is placed a few meters downstream from the target, it deflects

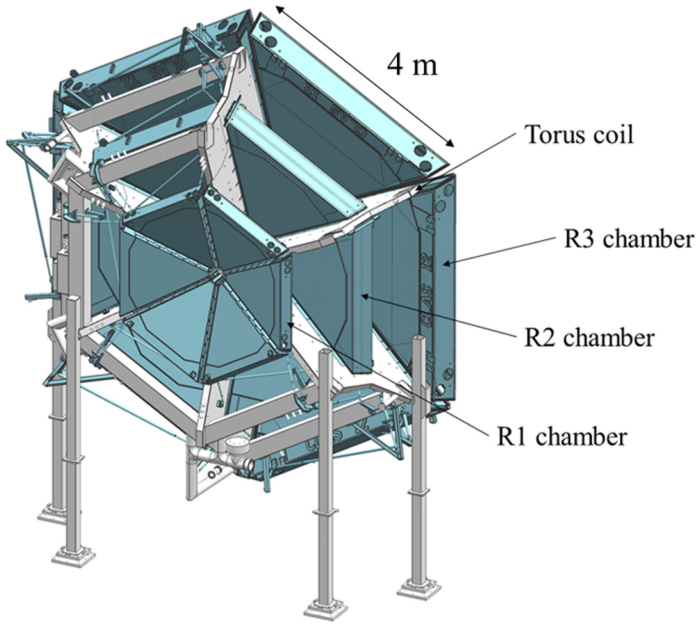

Figure 1.4: The CLAS12 Drift Chambers. The three regions are marked along with one torus coil. Picture adopted from [25].

particles that scatter at forward angles, $5° < \theta < 40°$ [20]. It consists of six superconducting coils that are arranged symmetrically around the beam axis (Figure 1.4 shows the placement of the coils) to approximate a toroidal field: charged particles are bent inward or away from the beam axis, the amount of bending providing a measure of particle momentum. There is a non-zero change in the azimuthal angle due to field imperfections. The Forward Detector measures the trajectories of particles that scatter at forward angles. The main subsystems of the detector are shown in Figure 1.2. The six torus coils divide the Forward Detector into six identical detection sectors on the xy-plane. Particle identification is provided by three Cherenkov counters that have different momentum thresholds for electron discrimination [26] [27] [28]. The High Threshold Cherenkov Counter (HTCC) is placed between the torus and solenoid. It identifies electrons below momenta of 4.9 GeV/c using dry CO_2 as the active medium: at this momentum, heavier charged particles do not emit Cherenkov radiation in CO_2

[26]. The HTCC consists of an entry and exit window and a mirror constructed from 48 facets placed radially around the beamline to focus the Cherenkov light onto 48 photomultiplier tubes (PMTs) [26]. It provides full coverage in the azimuthal angle. The Drift Chambers (DCs) map particle trajectories as they curve in the torus field with a cell resolution of $\sigma_r = 250$ μm [25]. There are 3 separate DC plates for each sector, referred to as regions. The regions are arranged around the torus coils as seen in Figure 1.4. Due to the placement of the coils, the azimuthal coverage varies from 50% at $\theta = 5^\circ$ to 90% at $\theta = 40^\circ$ [25]. Each region has 2 groupings of wire layers, superlayers, spaced apart by a few centimeters and strung at different stereo angles, $\pm 6^\circ$. This setup provides good resolution of both the polar and azimuthal angle [25]. Each superlayer consists of 6 layers of wires, the layers consist of 112 hexagonal cells placed in a brick-wall arrangement [25]. The cells contain a mixture of 90% Ar and 10% CO_2 and a central anode sense wire whose direction is perpendicular to the plane of the cells. The Forward Time-of-Flight system identifies particles by measuring their time of flight with a time resolution of $\sigma_t = 80$ ps [29]. It's constructed from three panels consisting of rectangular plastic scintillators, each panel covers a portion of the forward region. The scintillators are connected to a PMT on each end, the light produced by fluorescence of the detector material is collected at the PMTs [30]. Finally, two calorimeters absorb particles and measure their energy and the location of the energy loss [31]. They also detect neutral particles with an efficiency of $> 50\%$ [32]. The pre-shower (PCAL) and the electromagnetic calorimeter (EC) are of the sampling type, with interchanging layers of lead and scintillator strips in a triangular hodoscope layout. The electromagnetic showers produced by Bremsstrahlung radiation of charged particles, or by pair production of photons, produce photons in the scintillation material that are detected with PMTs [31]. There are 15/15/24 active layers for the PCAL, the inner EC and outer EC. The scintillating layers alternate between three readout planes that are each parallel to one of the sides of the calorimeter [32]. The light from each strip in a layer is measured in sum, all strips in a layer are connected to one PMT [32]. The energy resolution equals $\frac{\sigma_E}{E} = \frac{0.1}{\sqrt{E(GeV)}}$ [32].

The resolution of the reconstruction software was computed for particles scattering at forward angles. The Forward Detector has a fractional momentum resolution of $\frac{\sigma_p}{p} = 0.5 - 1.5\%$, and an angular resolution of $\sigma_\theta = 1 - 2$mrad [19]. This study will provide a detailed analysis on how accurately the reconstruction software reconstructs events when conditions such as the beam energy and species or the torus polarity is varied. Forward tracking in the Drift Chambers will be described first; this knowledge is necessary to understand the trends seen in our results. Section 2.2 is an introduction to the software packages that were used during the course of this study. The methodology that was followed to obtain the resolutions will be described afterwards, followed by the validation of the method and the results. The paper concludes with a summary and a discussion on the future uses of the algorithm.

Chapter 2

Methods

2.1 Event Reconstruction

2.1.1 The Coordinate Systems of CLAS12

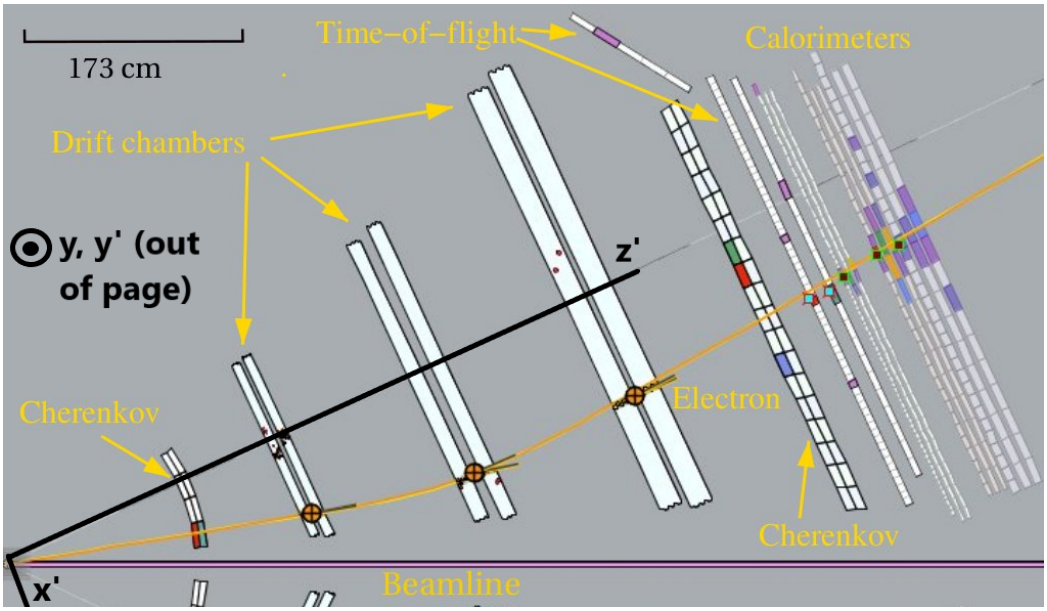

Figure 2.1: A CLAS Event Display (CED) application window showing an event in CLAS12, looking at the detector from above. The tilted x, y and z axes are shown as x', y', z' (y and y' coincide). The Lab z-axis coincides with the beamline. The origin, the target, is on the bottom left of the figure. The coloured detector elements are the elements with a signal above the threshold, and the points in orange are crosses. NOTE: The default torus configuration bends the negatively charged particles inward.

Before the event reconstruction process in the Forward Detector is described, the coordinate systems used in the calculations must be defined. The CLAS12 Lab coordinates are defined as follows: the z-axis coincides with the beam axis and the y-axis points vertically upwards, while the origin is at the center of the target (Figure 2.1). The Drift Chamber plates and the detection layers of the FTOF and the calorimeters are inclined 25° with respect to the beam axis, as seen in Figure 2.1. If a Cartesian coordinate system is defined such that one axis is rotated 25° with respect to the lab z-axis, the trapezoidal detection planes of the three detectors will be perpendicular to this axis (this rotated z-axis is marked as z' in Figure 2.1). Their detection layers will thus all be at fixed values of the z-coordinate in this Tilted Sector Coordinate System (TSCS), which simplifies the calculations in the track reconstruction process. The TSCS is restricted to one detection sector, a schematic showing how the detection sectors of CLAS12 are defined is provided in Figure 2.2.

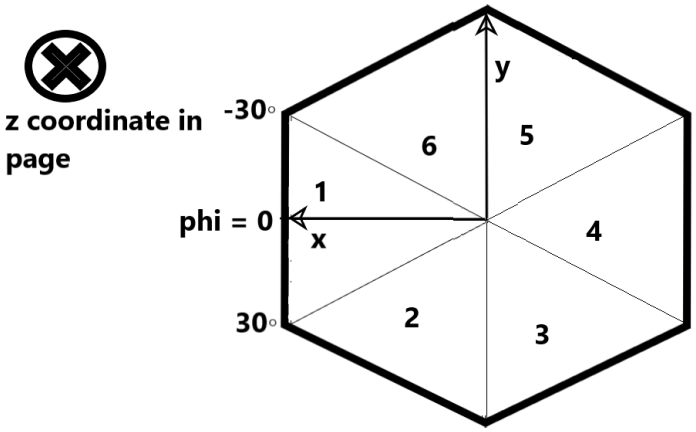

Figure 2.2: A view of the detection sectors of CLAS12, with the global phi coordinate's zero, −30, and 30 degree points highlighted. Also shown in this picture are the axes of the Lab Cartesian coordinates.

To go from lab coordinates to the TSCS, the three axes are rotated as follows (s denotes the sector):

$$x_{TSCS} = x_{Lab}*cos(25^\circ)*cos[(s-1)*60^\circ]+y_{Lab}*cos(25^\circ)*sin[(s-1)*60^\circ]-z_{Lab}*sin(25^\circ)$$

$$y_{TSCS} = y_{Lab} * cos[(s-1)*60^\circ] - x_{Lab} * sin[(s-1)*60^\circ]$$

$$z_{TSCS} = x_{Lab}*sin(25^\circ)*cos[(s-1)*60^\circ]+y_{Lab}*sin(25^\circ)*sin[(s-1)*60^\circ]+z_{Lab}*cos(25^\circ)$$

2.1.2 Forward Tracking

A charged particle travelling through the Drift Chambers (DCs) ionizes the electrons of the active medium along its trajectory. The ionized electrons drift towards the sense wires as they are accelerated by an electric field [33]. The current pulse due to the charges arriving at the wires is measured along with the time at which the ionized electrons arrived [25]. Track reconstruction happens in two stages, the first being "Hit-Based" Tracking (HBT). Only the location of the cells is used in HBT, time measurements are incorporated in the second stage of tracking. Cells with signals are identified first and are saved as "hit" objects. This is followed by a search for clusters, localised groups of hits within a superlayer. The clusters that are track candidates are then fitted with linear functions. The parameters of two fits applied to clusters in neighbouring superlayers in a region are combined to form a 6-dimensional object at the midpoint between the superlayers. These objects are called crosses, and they are shown in orange between superlayers in Figure 2.1. A parabolic function is then fitted to the crosses as a first track estimate [34]. The θ angle of the first and third cross and the path length between the crosses is then inserted for the radius ($dr = \frac{dl}{d\theta}$, formula for the arc of a circle) in the expression equating the Lorentz and centripetal force to compute the ratio $\frac{q}{p}$, where q is the charge and p the momentum magnitude of the particle:

$$\frac{q}{p} = \frac{\theta_3 - \theta_1}{\nu \int Bdl} \tag{2.1}$$

We assume $\nu \approx c$. The position and the momentum components of the particle at the first DC layer are obtained from the crosses. The track is then fitted with a Kalman Filter, a recursive algorithm used in statistics for evaluating variables from a series of measurements observed at different times, or in this case at a different z-coordinate [35]. The algorithm consists of two stages, prediction and update: the measurement at the next site is first predicted with numerical methods. The actual measurement is then corrected by taking into account the trend of the previous measurements and their uncertainties [35]. The algorithm uses 5 parameters evaluated at the first DC layer as input: x, y, tx, ty and Q, where $tx = \frac{p_x}{p_z}, ty = \frac{p_y}{p_z}, Q = \frac{q}{p}$. These parameters will be referred to as a state vector. Each measurement site is at a fixed z-coordinate in the TSCS, so the state vector parameters are expressed as derivatives with respect to z [34]. Fourth-order Runge-Kutta integration with fifth-order corrections for step size control is used to propagate the state vector and its derivatives from one measurement site to the next in the prediction step. This numerical method solves initial value problems by evaluating expressions at four increments between the two measurement sites [36]. The results are then combined in a weighted average to produce the final estimate of the variable at the end of the interval [36]. The step size control algorithm will be described in Section 2.4 as it is used to compute the reconstruction resolutions.

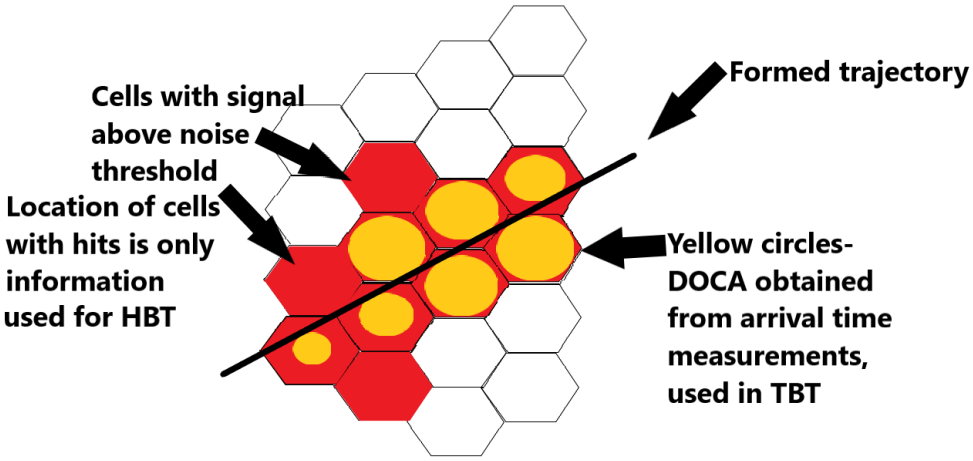

Figure 2.3: A 2D representation of a layer of cells in the Drift Chambers. The reconstructed particle track is represented by the line in the image. The red hexagons represent the wire cells with an electrical signal, and the yellow circles show the estimate of the distance of closest approach computed from the time of arrival of the signal on the wires.

The propagation of a particle trajectory through a magnetic field with numerical methods will be referred to as "swimming" from here on. A second Runge-Kutta method is employed simultaneously to swim the state vector covariance matrix. This matrix contains the uncertainties in the measurements and their correlations. To clarify, the matrix f_{k-1} propagates the state vector a_{k-1} from site $k-1$ to site k in the prediction step, the terms of this matrix are obtained with Runge-Kutta methods. The propagator matrix of the covariance matrix is then calculated as [37]:

$$F_{k-1} = \frac{\partial f_{k-1}}{\partial a_{k-1}} \tag{2.2}$$

The matrix also contains a process noise term which takes into account multiple scattering through the DC volume [34][38]. After the swimming of the state vector and the covariance matrix, the prediction is mapped onto a measurement. The weight of the measurement compared to the prediction is estimated with the Kalman gain, a term obtained from the covariance matrix [35]. The optimal measurement at each site is obtained by minimizing the increase in the χ^2 quantity, which is an estimate of the quality of the fit [37]. Once the Filter fits the trajectory through all three DC regions, the trajectory is fitted backwards using the information from all measurement sites. More information on how the terms of the different matrices and χ^2 are obtained can be found in a HERA-B note on the Kalman Filter as forward tracking in CLAS12

was modelled after the HERA-B tracking software [39]. Once the trajectory is reconstructed in the DCs, the particle is swum to the interaction vertex, the location of closest approach to the target. The swimming is repeated, this time from the vertex, to compute the track location at the surface of each of the remaining subsystems of CLAS12. The DC fitting is then redone with time-based information: the arrival of ionized electrons on the wires is measured with Time-to-Digital Converters (TDCs) with a resolution of $\sigma_t < 1$ ns [25]. If the event start time is known, the drift time of ionized electrons can be computed. The drift time can be converted into a Distance Of Closest Approach (DOCA) of the beam particle to the wire using a fourth-order time-to-distance polynomial function [34]. See Section 8.1 in [25] for a description of the calibration procedure for this polynomial. The DOCA at each cell is used to form a circle around the wire, as seen in Figure 2.3. These circles are then used in the second iteration of the Kalman Filter to further constrain the trajectory.
The Event Builder is the last service employed in reconstruction. It matches hits from different detectors to the trajectory that was formed in the DCs and swum to the remainder of CLAS12. The rejection criteria is a fixed distance between the hit cluster in the detector and the reconstructed trajectory that was swum to that detector. Time-based reconstruction proceeds after the process of hit matching. The Event Builder also identifies the species of particles. Details on how the Event Builder identifies particles, how it organizes responses from detector subsystems and saves the results of the physics analysis in data structures can be found at the following link: `https://clasweb.jlab.org/wiki/index.php/CLAS12_EventBuilder`.

2.2 The CLAS12 Software Structure

The CLAS Offline Analysis Tools (COATJAVA) is the collection of software tools used by researchers in Hall B to simulate, reconstruct and analyze event data. The tools consist of many software packages, the ones used in this study will be described in short. The software services that process raw detector signals and produce reconstructed trajectories are contained within the hall reconstruction framework, the CLAS Analysis and Reconstruction Architecture (CLARA). The software handles over a hundred thousand readout channels of the CLAS12 detector, and it achieves a live time of above 95% (time during which the detector records data) [40]. CLARA is based on a service oriented architecture: many smaller services reconstruct individual signals, application controller agents orchestrate the processed information and perform physics data analysis, and additional agents oversee the reconstructed event data in real time and ensure the functionality of parallel event reconstruction on multiple nodes [40]. Once the reconstruction of a set of events is completed, CLARA produces a High Performance Output (HIPO) file that contains the reconstructed events. One reconstructed event consists of many data banks: some banks contain reconstructed

information from one of the detectors (times, energies, etc.) and some contain general event information that's computed by the Event Builder. For example, the banks produced by the Event Builder can contain the positions and momenta of the beam at the interaction vertex, the event start time, the quality of particle identification, the trajectory coordinates at each detector surface and more. If the events were simulated with the Hall simulation software, the reconstructed event will also contain data banks that hold the simulation input parameters and banks that hold simulated raw detector outputs. The Geant4 Monte Carlo software (GEMC) is the Hall simulation software [41]. It utilizes Geant4, a software platform that simulates the passage of particles through detector materials [42]. The positions and momenta of particles at the interaction vertex are the input for the software at the start of the simulation. External event generators that employ theoretical models of the scattering can be used to obtain the inputs. The GEMC internal event generator was used to create events during the course of this study. To utilize the internal generator, the initial conditions of the scattered beam need to be defined in a text file: the number of events, the particle species, the range of the z-coordinate at the interaction vertex (target size), the angles and momenta at which the particles scatter from the target, and the detector configuration to use. The internal event generator randomizes the initial positions and momenta of the scattered particles within the constraints of this text file. GEMC then creates *Geant*4 detector objects using simulation parameters such as the detector geometries (placement of the detector in the CLAS12 coordinate system and the hierarchy of its elements), digitization constants, mirror surfaces and electromagnetic fields. These parameters are stored in external databases as tables and text files. The particles are transported from the interaction vertex through CLAS12 with a "truth information" bank that contains the kinematic information of the particle [41]. After the particle was propagated through one interval with numerical methods in the navigation step, digitazion routines calculate energy losses at appropriate locations within the detector volume and approximate detector responses with Gaussian or Landau distributions [41]. The software collects the raw output produced by the detectors in a single file which is then passed to the reconstruction framework. The Calibration Constants Database (CCDB) is a package that contains all the calibration constants of the detectors and maps of the entire CLAS12 spectrometer that are used in simulation and reconstruction [34]. The swimmer package "swims" particles in magnetic fields using the aforementioned Runge-Kutta methods. The method used to evaluate the reconstruction resolutions is based on the swimming of particles through CLAS12. The numerical methods that were used throughout this study differ from the methods used in the Kalman Filter in DC reconstruction. These methods will be described in detail in Section 2.4. The swimmer package utilizes the magnetic field package to obtain the values of the magnetic field at points in space. This package is also used in reconstruction to compute path integrals through the DCs (equation

2.1). The package creates binary field maps from software models of the torus and solenoid [20]. Event data is plotted with GROOT. This software package allows the plotting and fitting of histograms with scripts written in Java and with graphical interface tools. The former method will be used to plot the results obtained in this study. Finally, the CLAS Event Display (CED) is an application that displays events in the CLAS12 detector. The application can display reconstructed tracks, detector elements with signals above the thresholds, and the magnetic fields [34].

2.3 Overview of the Method

This project aimed to obtain the resolution of the CLAS12 reconstruction software from simulated events and to study how the resolutions change when beam conditions such as the particle energy and species are varied. The events used in the analysis are created with the aforementioned simulation software GEMC. The CLARA framework was used to reconstruct the events. The software tools that were used to manipulate the event data and compute the resolutions are all contained within COATJAVA. The COATJAVA code repository can be found at the following link: `https://github.com/JeffersonLab/clas12-offline-software`. The versions of the software changed throughout the course of this study, the most recent version that was used to compute the results was version 6.5.9. As mentioned before, the reconstructed event file consists of many data banks for each event. Two data banks containing the positions and momentum components of beam particles at the interaction vertex hold the relevant information for this study.

1. One bank contains the state vector, the position and components of momenta in Lab coordinates, of the beam particle at the vertex as created by GEMC's event generator. This is the starting point from where GEMC simulates the passage of the particle through CLAS12. This will be referred to as the generated or simulated vertex.

2. The second bank also contains the vertex state vector, but this state vector was obtained with the event reconstruction software: the raw Drift Chamber hits were processed and the trajectory was swum to the interaction vertex. This will be referred to as the reconstructed vertex.

3. The two vertex state vectors are then used as the starting positions and momentum components for the particle swimmer: one track will be propagated through CLAS12 to mimic the simulated track, the other will mimic the reconstructed track.

4. The two particles are swum with Runge-Kutta methods through CLAS12 until the surface of a detector is reached (referred to as an endpoint), where the swimmer returns the state vectors.

5. The differences in position, angles and impact parameter between the two tracks at the endpoints are computed and plotted in histograms with GROOT as $\Delta = reconstructed - generated$.

6. The histograms of differences in observables are fitted with Gaussian functions and the standard deviations of the fit functions are the reconstruction resolutions.

In this case the impact parameter is the distance between the two tracks on the surface of the detector. The generated vertex state vectors are the only track parameters produced in simulation that are present in the reconstructed event file. By propagating particles from a position generated in simulation and a position obtained from reconstruction, the swimmer algorithm allows us to recreate simulated and reconstructed tracks and thus obtain the resolution of the reconstruction software at various positions within the CLAS12 detector. The reconstruction resolutions are obtained as

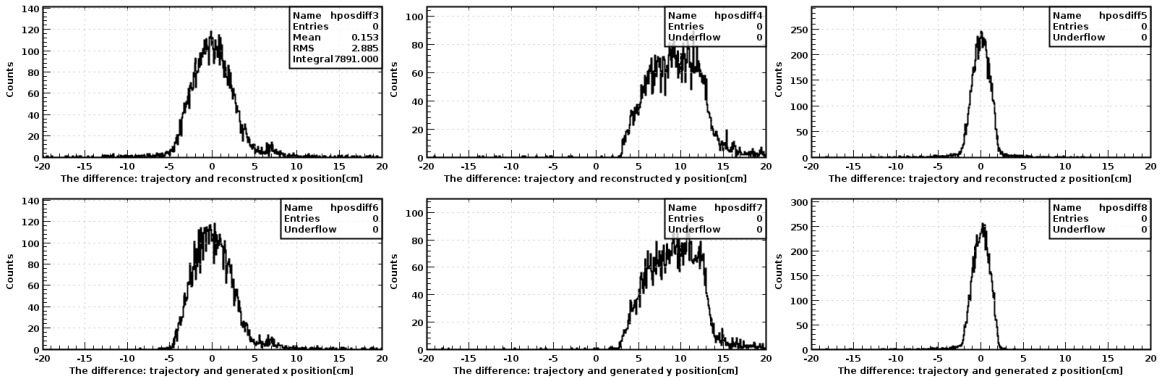

Figure 2.4: Histograms showing the differences between the reconstructed track and the swum particle tracks in cm, differences are computed as $\Delta = reconstructed - swum$. The swum tracks in the top row use the reconstructed vertices as input, bottom row uses generated vertices.

the standard deviations of the fit functions because the histograms show differences between the simulated and reconstructed tracks: the standard deviation of one histogram represents the amount of dispersion of the histogram, and hence the amount of dispersion between the simulated and reconstructed tracks. A measure of error in our estimate of the resolution is given by the uncertainty in the standard deviation:

$$\delta\sigma = \frac{\sigma}{\sqrt{2N-2}} \tag{2.3}$$

N denotes the number of events, and σ is the resolution. All histograms were plotted with a fixed bin size, the range of the data spanned from -2.5 cm to 2.5 cm ($-2.5°$ to $2.5°$ for the differences in angles) and the default number of bins was set to 800. A smaller bin size than this does not improve the accuracy of results, which is why this size was chosen.
Before results are gathered for different event files, the tracks obtained by swimming particles had to be compared to the reconstructed event trajectories. As mentioned before, the reconstructed event file contains a data bank that has the coordinates of the reconstructed trajectory at the surfaces of the detectors in the forward region. The swum tracks were compared to this trajectory at the first DC superlayer and the results of this comparison are seen in Figure 2.4. The histograms show that the differences between the tracks propagated by swimming and the reconstructed trajectory are around a few centimetres at the first region of the Drift Chambers, which is at a distance of ≈ 2.5 m from the origin. The positive tails and a non-zero y-mean are present because the swimmer does not simulate the energy losses due to interactions with detector volumes. To conclude, the swum trajectories resemble the original event trajectories enough for our resolution measurements to be valid.

2.4 The Details of the Swimmer Software Package

Two different swimmer methods were used to swim particles to the HTCC, the Drift Chambers, the FTOF system, and the inner EC. In addition to the starting positions and momentum components, the magnetic field files and the endpoint location are also inputted at the start of swimming. The exact positions where the state vectors of the two tracks are compared can be seen in the table below.

Swimmer endpoints
HTCC: 175cm from the origin
DC superlayer 1 (R1), 6th layer, $z' = 235.072$ cm
DC superlayer 2 (R1), 6th layer, $z' = 246.006$ cm
DC superlayer 3 (R2), 6th layer, $z' = 363.1623$ cm
DC superlayer 5 (R3) 6th layer, $z' = 506.05$ cm
FTOF panel 1a, $z' = 684.81$ cm
inner EC, 4th layer, $z' = 734.85$ cm

The locations of the endpoints of swimming. The letter R denotes the DC region to which the particles are swum to. The 6th wire layer is the last layer in each superlayer. The z' distances shown here are the z-coordinates of the endpoints in the TSCS.

The magnetic fields are loaded with text files, the maps contain the values of the fields in one half sector to reduce the time it takes to swim events. This neglects

possible field imperfections in some areas of the CLAS12 detector, but the effect of these imperfections is small and the loading of the full magnetic field file to swim each particle would be too time-consuming. The probe object of the magnetic field package is also utilized: this object caches nearest neighbour values within a grid cell when loading in the magnetic field at a point, thereby further reducing the time of swimming [34]. The numerical methods used in this study differ from the methods used in

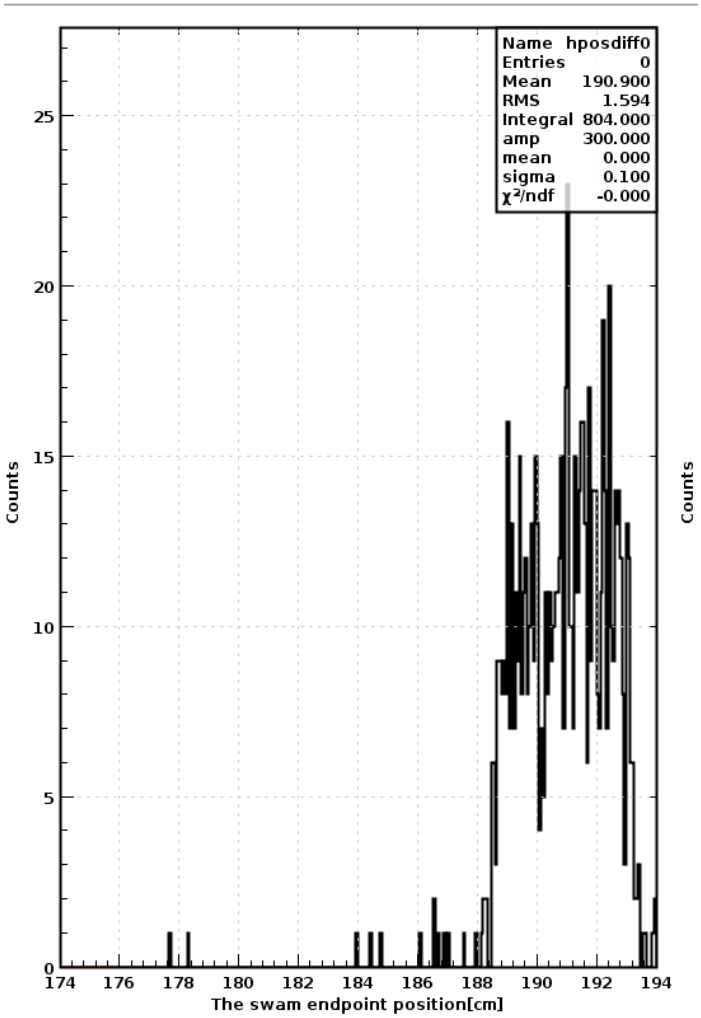

Figure 2.5: A histogram of path lengths of particles swum to the HTCC when an adaptive step size swimmer method is used. The adaptive step algorithm forces a big step size for the final step due to the low field value: the wide distribution of the endpoints extends up to 190 cm, which is 15 cm above the defined path length threshold.

reconstruction: the derivatives are evaluated with respect to the path length, not the

z-coordinate. The Ordinary Differential Equations that are numerically integrated by the swimmer are obtained from the Lorentz force equations by expressing the velocity as a derivative of the path length. These expressions are then evaluated with fourth-order Runge-Kutta methods with fifth-order corrections, but this time the state vector has six components $(x, y, z, \frac{p_x}{p}, \frac{p_y}{p}, \frac{p_z}{p})$. The fifth-order corrections allow for the use of an adaptive step size in the integration. An adaptive step size algorithm wants to implement the largest possible step size for which the solution to the equations is within the desired accuracy in order to improve the speed and efficiency of the code [36]. The error estimate is calculated as the difference between the results obtained by a fifth-order classical Runge-Kutta formula and the embedded fourth-order Runge-Kutta formula as described in section 16.2 in [36]. The error tolerance is fixed as 10^{-5}, this is an absolute difference in units of meters for the spatial components and unitless for the fractional momentum components of the state vector. In areas of weak field, the change in the elements of the state vector is small and therefore a bigger step size can be taken as the truncation errors won't increase significantly [36]. When particles were swum to the HTCC with adaptive step size methods, the resolutions were larger than the ones obtained with fixed step size methods. The adaptive step size algorithm produced better results at other detectors, so this abnormality was investigated. The HTCC is placed in an area where the magnetic field is very weak, $B \approx 10^{-3}$ T - 10^{-4} T (values obtained with CED, the field at any point can be computed in the application by simply placing the cursor on the point of interest). The detector surface is defined as being at a fixed radial distance from the target, at 175 cm. Figure 2.5 shows the path length of tracks swum to the HTCC with adaptive step size methods, 1000 electrons were swum. As the magnetic field is weak, this causes a large final step of around 15 cm (peak at 190 cm in the figure). This causes the observed increase in the resolutions compared to the fixed step size methods. The swimmer to the HTCC employs a fixed step size of 10^{-4} meters as smaller steps than this do not improve the accuracy and larger steps result in greater truncation errors. The method that swims particles to the DCs, the FTOF and the calorimeter uses an adaptive step size, and the endpoints of swimming are defined differently. All three detectors are shaped as trapezoidal planes with a polar inclination of 25° with respect to the beam axis. Therefore, the numerical integration proceeds in the aforementioned Tilted Sector Coordinate System (TSCS). The planes of the detection layers are defined only with their z-coordinate in this frame as this axis is perpendicular to the detection layers of all three detectors. The z-coordinate of endpoints is obtained by constructing *Geant4Factory* objects in the tilted frame. These software objects place the detectors and all their individual sub-components in a given coordinate system in simulation by interfacing with the Calibration Constants Database [41]. The FTOF and the EC are also in a region of a weak magnetic field, but the adaptive step size method was optimized for swimming to a fixed z-

coordinate in the TSCS. An accuracy parameter for the endpoint z-coordinate exists, this parameter defines how accurately the swimmer will stop at the endpoint. A z-coordinate accuracy of 10^{-5} m was used throughout this study. This feature is not available for the method that swims in Lab coordinates that is used to obtain results at the HTCC (numerical integration proceeds in the TSCS in reconstruction, therefore these swimmer methods are more developed and have more features). The vertex state vectors and the magnetic fields need to be rotated to the TSCS before they're inputted into the methods that swim in this frame. Once the tracks are swum, the endpoint state vectors need to be rotated back to the lab frame before the resolutions are computed. The only exception to this is the impact parameter, as this quantity represents the physical distance between the two points on the detector plane when computed in the local frame of analysis. The quantity is computed as $b = \sqrt{x^2 + y^2}$ in the TSCS, and its computed as $b = \sqrt{x^2 + y^2 + z^2}$ in the Lab coordinates at the HTCC.

2.5 Identifying the Cause of Systematic Errors

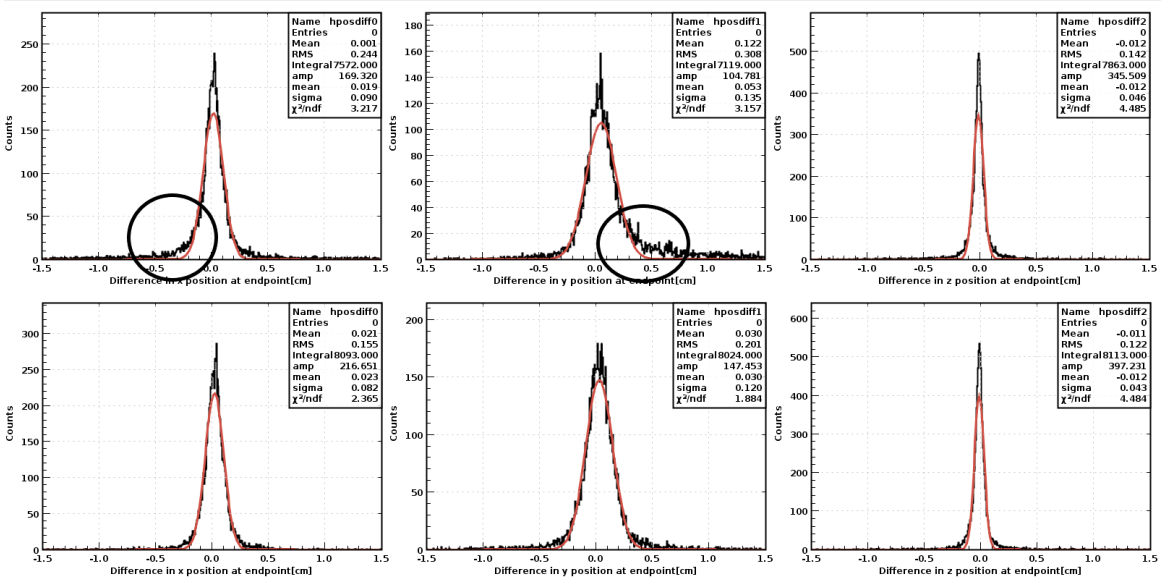

Figure 2.6: The histograms of differences in endpoint x, y, and z positions for electrons (top row) and muons (bottom row). The red line represents the Gaussian fits to the data. The circled areas show the negative tail on the x axis and positive tail on the y axis that's present for electrons, but not present for muons.

The first event file that was created to test the swimmer algorithms consisted of

10 000 monoenergetic beam electrons at 6 GeV scattered throughout sector 1 of the active detection area, $-30° < \phi < 30°$, spread through the full range of polar angle of the Forward Detector, $5° < \theta < 35°$ ($35° < \theta < 40°$ region was not included as the performance of the detector drops off at the edge of the forward region). The target size was 5 cm, so the particles had a vertex z-coordinate in the range of $-2.5 < z < 2.5$. This angular range and target size will be the standard values that will be used for all event files unless specified otherwise. The two sets of vertex positions and momenta present for each event (simulated and reconstructed) were used as input for the algorithm that swims to the HTCC. The resulting differences in position of the two tracks at the HTCC are seen in the top row of Figure 2.6. The bottom row of this figure uses a different event file and those results will be discussed later on in this paragraph. The histograms of differences in the x, y and z-coordinate are centered around zero and have widths that were expected, but the plots have one unexpected feature, the one-sided tails. The tails make the distributions asymmetric. The fitting algorithm struggles to fit symmetric Gaussian functions on these distributions so the source of these tails needs to be identified and understood. The first check that

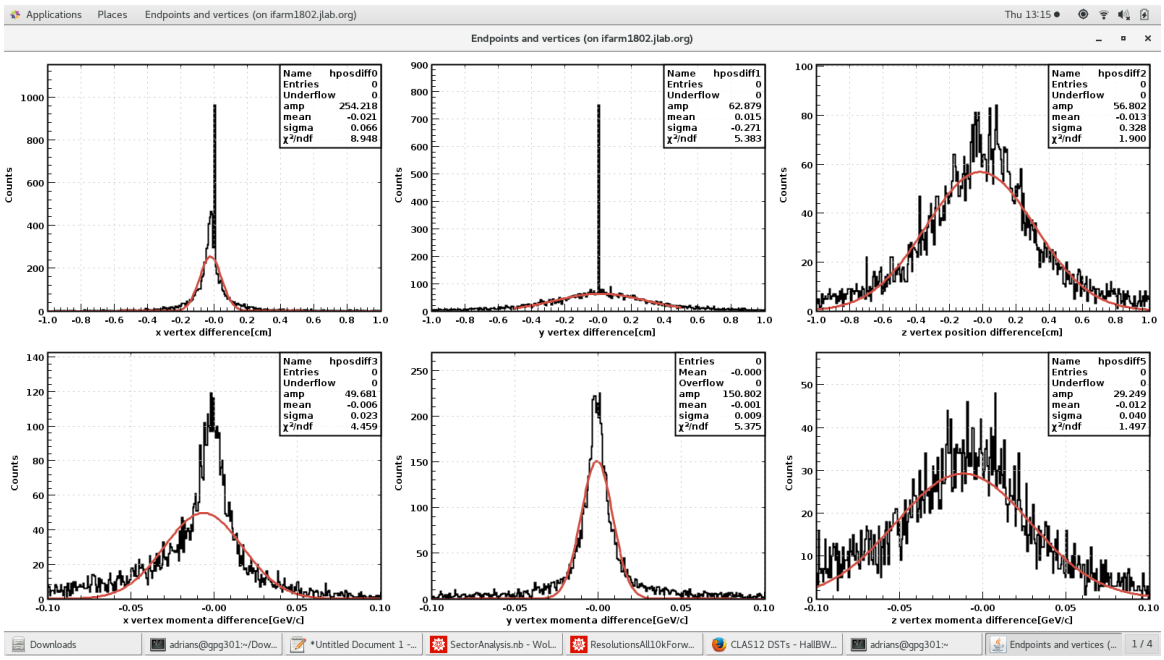

Figure 2.7: The histograms of differences in vertex x, y, and z positions are shown in the top row, while the histograms of differences in momenta at the vertex are shown in the bottom row. There is a significant tail that's seen on the plots of x and z momenta.

was conducted was the plotting of vertex distributions. To clarify, the distributions

of differences in position and momentum of the two tracks at the starting point of swimming, the vertex, could be asymmetric, which would cause asymmetries in the results at the HTCC. The differences in position and components of momenta of the two tracks at their starting points are shown in Figure 2.7. The histograms of differences in position seem symmetric, but the momentum distributions in the bottom row have significant tails that match the tails seen in the histograms of differences in position at the HTCC. Therefore, the inaccurate estimate of the vertex momentum in reconstruction causes the tails seen in our histograms of differences in observables at the HTCC. The vertex momentum is estimated in reconstruction from the amount of track curvature in the DCs (equation 2.1): this determines the momentum magnitude, and the momentum components at the vertex are obtained from the swimming and fitting of the track to the vertex. The inaccuracy in estimating the vertex momentum in reconstruction could be explained with the effect of synchrotron radiation: as an electron enters the torus field in the DCs, the bending of the trajectory causes a change in the electron velocity. The change in velocity causes an emission of radiation [43]. The emission of radiation decreases the electron momentum. This decrease in momentum causes an increase in the amount of bending of the track in the magnetic field. If this momentum loss is not taken into account, the reconstruction software will estimate a lower momentum magnitude due to the observed additional bending in the DCs (equation 2.1). The momentum differences are computed as $\Delta = reconstructed - generated$, so the negative momentum tails on the x and z axis support this hypothesis as the emission of radiation is along the direction of motion, and the track bends in the xz-plane. An expression for the power radiated by a relativistic electron due to synchrotron radiation can be obtained from the classical expression: $P = \frac{2}{3}\frac{e^2}{m^2c^3}(\frac{dp}{dt})^2$. The first step is to replace the time derivative in the expression with the derivative of proper time [43]. The squared momentum derivative with proper time is then replaced with an invariant expression as in [43]. The energy change with time is then dropped from the equation as it is negligible compared to the momentum change for a particle with centripetal acceleration [43]. The power emitted due to the radiation is then [43]:

$$P = \frac{2}{3}\omega_0 \frac{e^2}{R}\beta^3(\frac{E}{mc^2})^4 \tag{2.4}$$

A definitive test was devised to check if the radiation is the cause of inaccuracies. Equation 2.4 tells us that the power radiated by a particle depends inversely on the fourth power of the mass of the particle. If events are created in GEMC with beam particles that have the same amount of energy (6 GeV) but have much greater mass, the amount of power radiated will be negligible and the tails will disappear. The β^3 dependence is not important as $\beta > 0.99$ for all lighter particles at $E = 6$ GeV. 10 000 events with a negative muon beam were created with GEMC for this purpose. The energy (6 GeV), angular range (sector 1, forward angles) and target size matched the

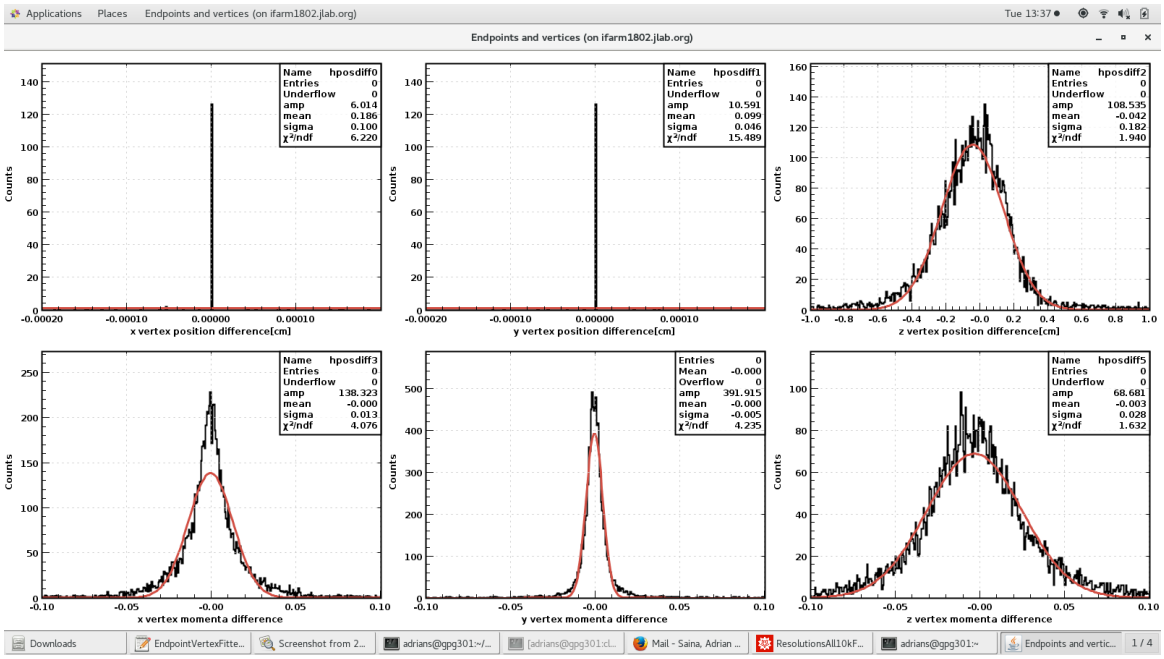

Figure 2.8: The histograms of differences in vertex x, y, and z positions (top row) and momenta (bottom row) for muons of same energy as the previously observed electrons, 6 GeV. The red line represents the Gaussian fits to the data. The tails that were present in the histograms of momentum differences of electrons do not appear in the muon plots.

electron beam events. If $m_\mu = 105.658 MeV/c^2$, the power radiated by synchrotron radiation compared to electrons ($m_e = 0.511 MeV/c^2$) of the same energy will be:

$$\frac{P_{mu}}{P_e} = (\frac{m_\mu}{m_e})^{-4} = (\frac{105.658}{0.511})^{-4} = 5.47 * 10^{-10} \tag{2.5}$$

Consequently, there will be no momentum tails at the vertex. This is exactly what is observed in Figure 2.8, which shows differences in vertex positions and momenta for the muon event file. When the muons are swum to the HTCC, the distributions of differences in position do not feature tails, as seen in the bottom row of Figure 2.6.

2.6 Histogram Fitting

The fitting algorithm uses the method of least squares to fit the endpoint distributions [44]. Initial estimates of the amplitude, mean, and width of the Gaussian function are inputted by the user, after which the algorithm finds the values of the variables for which the reduced χ^2 is minimised [45]. The algorithm struggled to fit Gaussian

functions on the histograms of differences at the endpoints due to the asymmetric tails of the distributions. All fits had a reduced chi-squared that was larger than three, which indicated that the computed standard deviations were inaccurate estimates of the widths of the distributions. In order to improve the estimation of σ, the

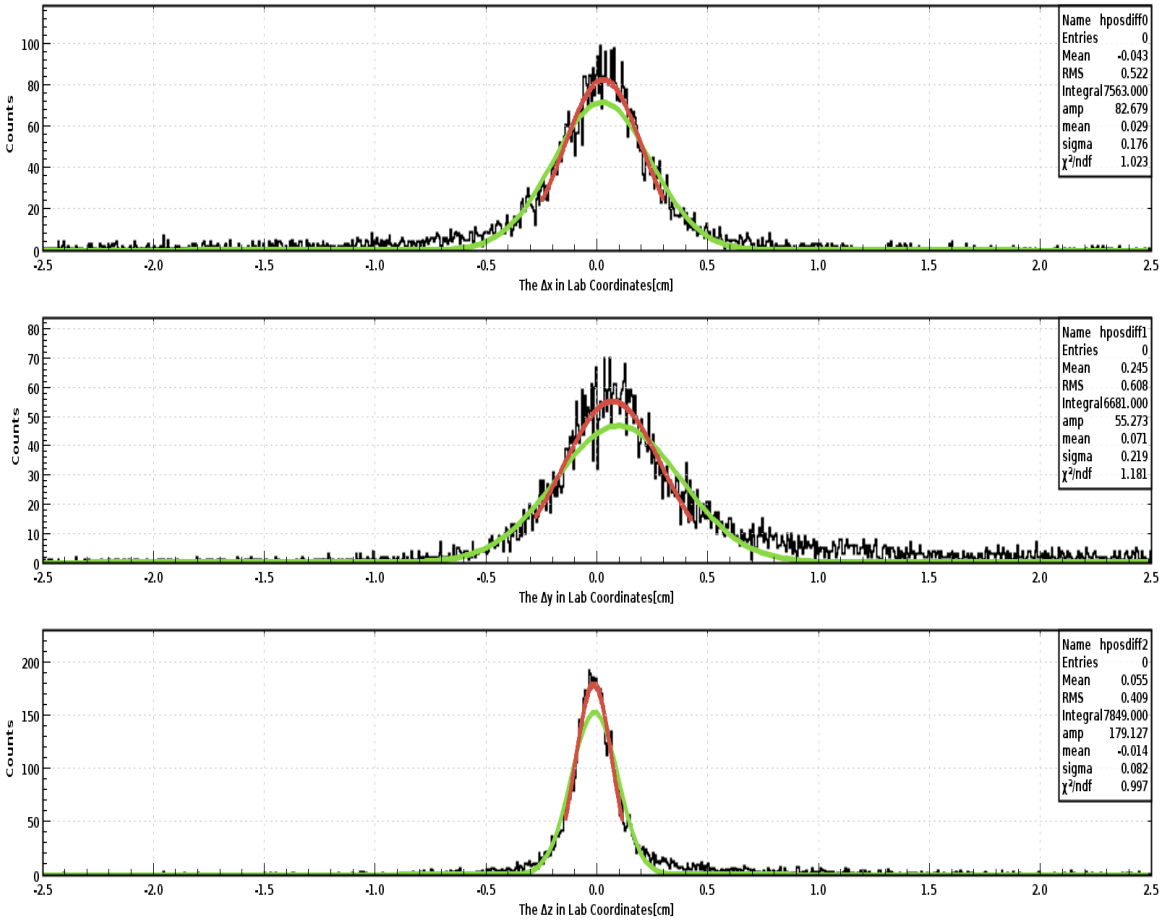

Figure 2.9: The differences in position of the two swum tracks at the first DC superlayer. The fits in green are the fits to the full range of the distribution, while the fits in red are the corrected central peak fits.

histograms were fitted with multiple Gaussian functions and the standard deviations were combined to produce an effective value. The first function fitted the data in its full range, the tails of the distribution extended up to ± 2.5 cm. The second fit was applied to the central peak of the distributions. The limits of this peak are defined by the statistical estimates of the previous fit: $\mu_1 \pm 1.5\sigma_1$. The full range fit does not have correct mean estimates, μ_1, due to the asymmetric tails of the distributions: this

will set incorrect limits for the central peak fit. The central peak fit was therefore applied twice: this fit has a correct mean estimate as it is not affected by the tails, so the second iteration of the central peak fit will have correct limits. The width of

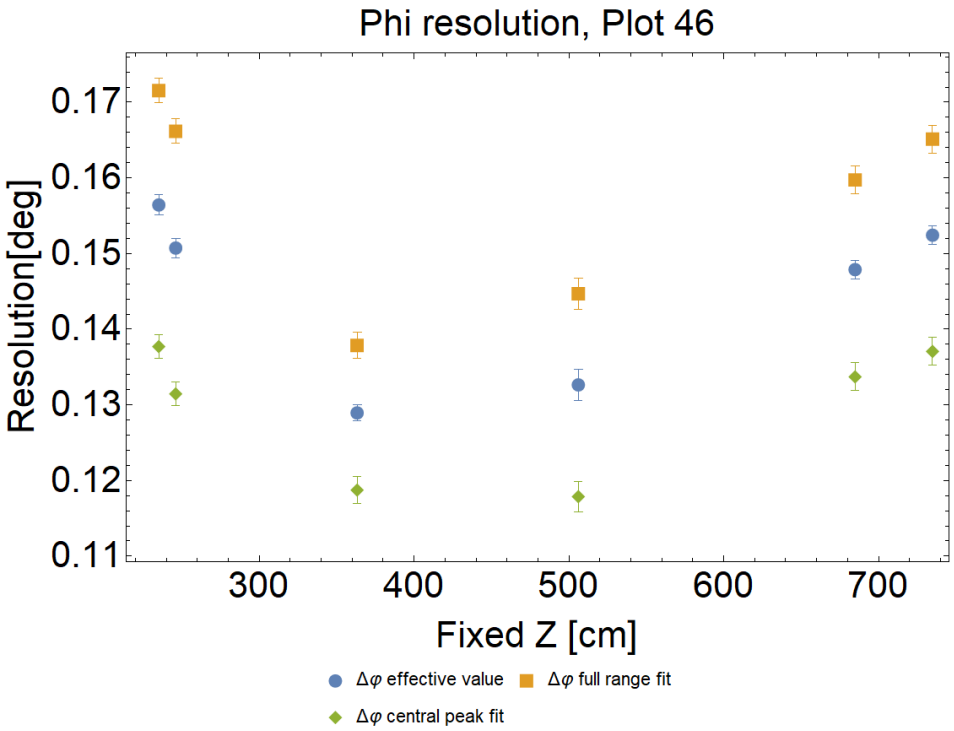

Figure 2.10: The phi resolution in degrees against the distance along the z-axis in cm of the endpoints in the Tilted Coordinate System (TSCS). The endpoints are given in Table 2.4, but the HTCC resolutions are omitted in this plot. In blue are the resolutions obtained from the entire data set, the resolutions estimated with central peak fits are orange. The green points represent the combined, effective resolutions.

the first (subscript 1) and final fit functions (3) were combined to obtain the effective moments as described in Section 3 in [46]:

$$m_1 = \frac{A_1}{A_3 A_1}\mu_1 + \frac{A_3}{A_3 A_1}\mu_3 \tag{2.6}$$

$$m_2 = \frac{A_1}{A_3 A_1}(\mu_1^2 + \sigma_1^2) + \frac{A_3}{A_3 A_1}(\mu_3^2 + \sigma_3^2) \tag{2.7}$$

The effective width of the histograms, and hence the effective resolution is then [46]:

$$\sigma_{eff} = m_2 - m_1^2 \tag{2.8}$$

Figures 2.9 and 2.10 both use the same event file that was used to obtain results at the HTCC in the previous section, 10 000 beam electrons at 6 GeV were swum. The full range and the corrected central peak fit are shown in Figure 2.9, which displays differences in position coordinates of the two tracks at the first DC superlayer. An example on how this fitting effects results is shown in Figure 2.10, the phi resolutions obtained from the full range fit, the corrected central peak fit and the combined fit at each endpoint are shown. The resolutions are shown against the z-axis distance (in cm) to each endpoint in the TSCS as this is the simplest way to display the spatial dependence of the resolutions. The points shown are at DC superlayer 1, 2, 3, and 5, the FTOF and the inner EC. The HTCC resolutions are omitted because of the use of a different swimmer method that swims in Lab coordinates. The results at the HTCC are displayed in the Appendix (see table B.1). This method of displaying resolutions against the endpoint z-coordinate in the TSCS while omitting the resolutions at the HTCC will be the standard method of presenting results in this paper. The resolutions are expected to increase linearly with the endpoint distance along the tilted z-axis. As seen in the Figure, this is not the case for the phi resolutions. The solenoid increases the phi angle close to the vertex. The two tracks have a slightly different x and y-momentum at the vertex so when the solenoid curves the tracks and increases the phi angles, the two tracks diverge. This results in high resolutions in the first DC region (first two points in Figure 2.10). The particles enter the torus field in the second region of the Drift Chambers (third point in Figure 2.10). When they enter the torus, the tracks bend in polar angle, while the azimuthal angle remains almost unchanged: this causes the observed dip in the phi resolution in the second DC region. After exiting the torus field the particles travel in straight lines, which causes a linear rise in the phi resolution for the final three points on the plot.

Chapter 3

Validation & Results

3.1 Validating the Method

3.1.1 Sector Analysis

The effective widths produced by fitting multiple Gaussian functions on histograms had to be tested for how well they represent the resolutions of the reconstruction software. 10 000 events of a 6 GeV e^- beam were created for this purpose in each of the six detection sectors of the CLAS12 detector. The events were spread throughout the azimuthal angle of the associated sector (e.g. sector 2: $30° < \phi < 90°$, sector 3: $90° < \phi < 150°$ etc.), and the particles were again sprayed at forward angles, $5° < \theta < 35°$. The detector components are identical in each sector, so the effective standard deviations at each endpoint should be approximately equal if they represent the resolutions of observables. The results of swimming particles in different detection sectors are seen in figures 3.1 and 3.2, where the differences in endpoint phi and theta angles in degrees are plotted against the distance along the z-axis to the endpoints in the TSCS. The plots of resolutions of the remaining observables can be found in Appendix B.3. In order to quantify the discrepancy in the resolutions at each endpoint, the reduced chi-squared quantity was computed for the six data sets. It was calculated at each endpoint with the following formula [44]:

$$\chi^2 = \sum_{i=1}^{N=6} (\frac{x_i - \mu}{\sigma_i})^2 \frac{1}{N-1} \tag{3.1}$$

The x_i and σ_i symbols denote the individual resolutions and their associated errors, μ denotes the mean of the six measurements at that endpoint, and N is the number of measurements being compared. The reduced chi-squared value of the phi and theta resolutions at each endpoint are shown in the tables below.

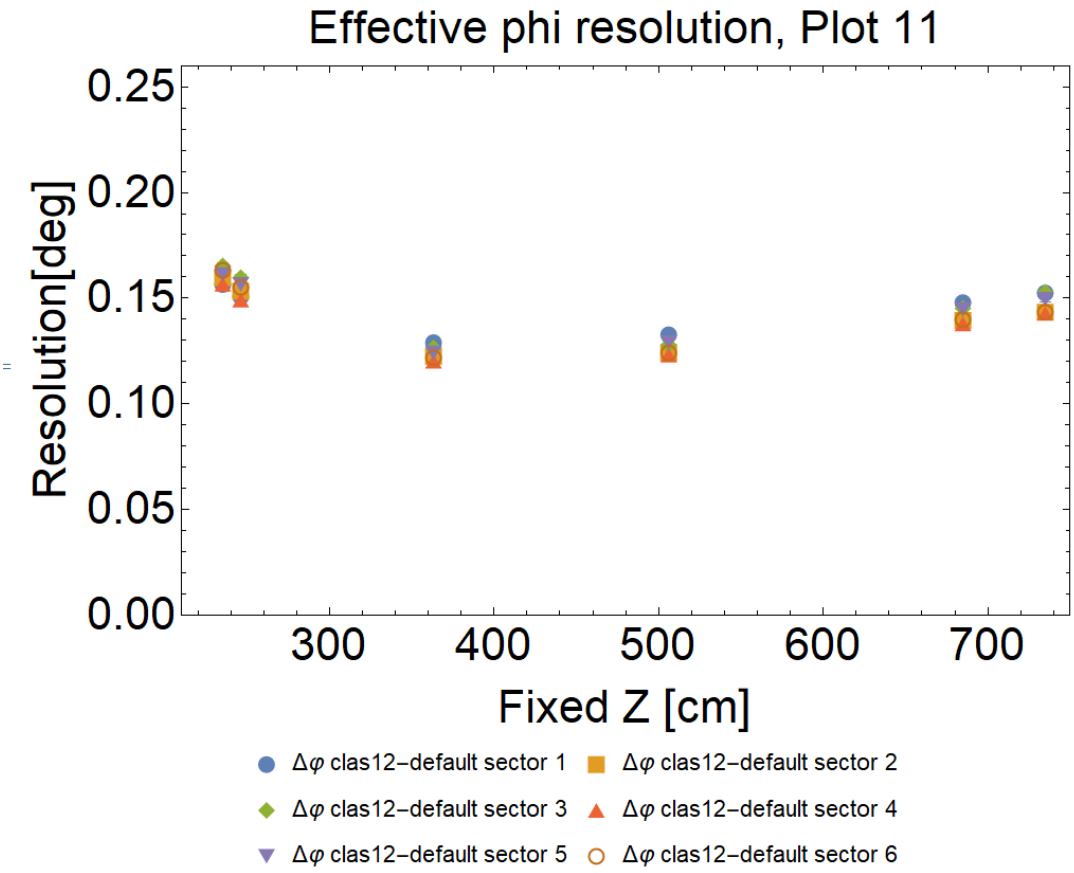

Figure 3.1: The phi angle resolution at the endpoints computed for the six sector event files. The resolutions are plotted against the z-axis distance to the endpoints in the tilted frame. The HTCC resolutions are omitted.

endpoint location	χ^2
DC superlayer 1	1.17111
DC superlayer 2	1.5101
DC superlayer 3	1.6384
DC superlayer 5	1.15356
FTOF panel 1a	1.84333
ECal inner 4th	2.4695

Chi-squared values of the phi resolution at the 6 endpoints for the six sector data sets.

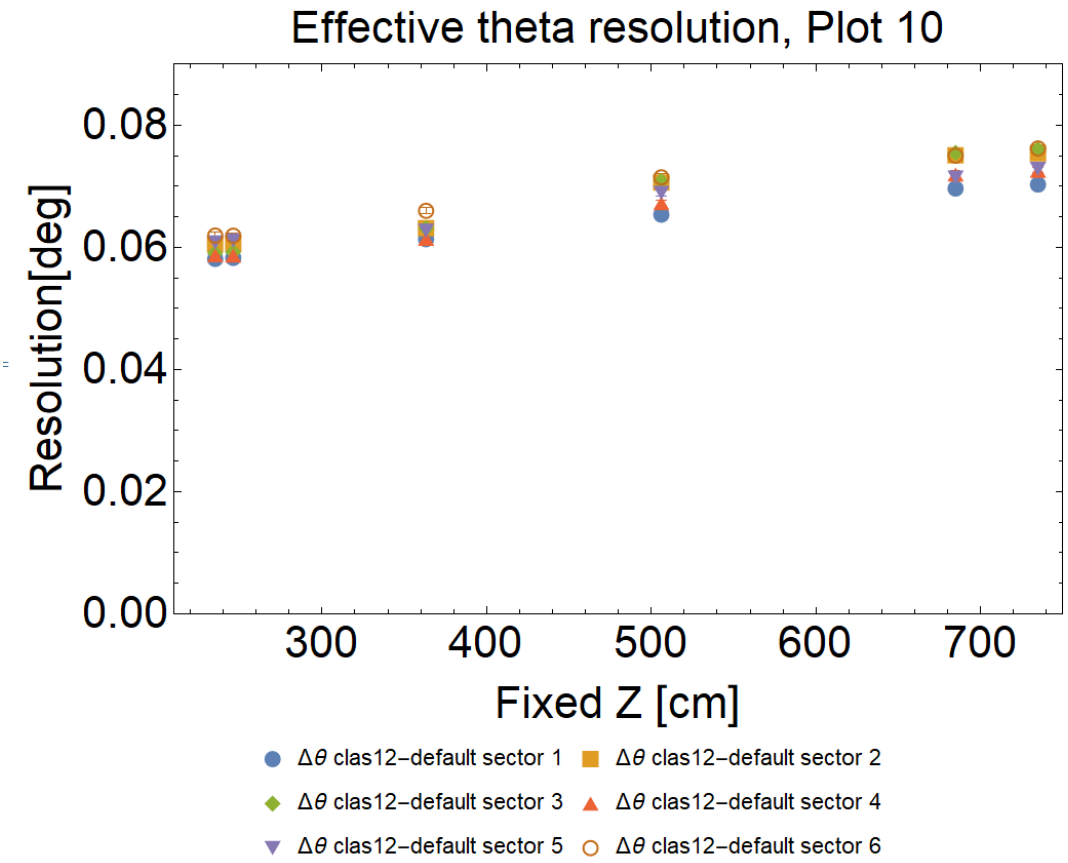

Figure 3.2: The resolution of the theta angle plotted against the z-axis distance to the endpoints in the tilted frame, the six sector data sets are marked as seen in the legend.

endpoint location	χ^2
DC superlayer 1	1.63529
DC superlayer 2	1.59259
DC superlayer 3	1.94385
DC superlayer 5	3.03924
FTOF panel 1a	2.89905
ECal inner 4th	2.73739

Chi-squared values of the theta resolution at the 6 endpoints for the six sector data sets.

The reduced chi-squared values obtained above reveal that there are small discrepancies between the resolutions in each sector. The spread in the vertex polar angle

of each event file causes the observed discrepancies because the resolutions change with the track polar angle. The torus field strength drops off towards the edges of the forward region. This decreases the amount of track curvature and hence increases the momentum resolution (see plots of the momentum resolution as a function of polar angle in [34]). The obtained reduced chi-squared values are therefore satisfactory, small discrepancies such as the ones seen above are caused by the angular spread in the data. The widths of histograms computed by combining two Gaussian functions are an accurate representation of the reconstruction resolutions, and the resolutions show no sector dependence. Real data has higher discrepancies between sectors due to imperfections in the magnetic field: the half-sector magnetic field files were used in the analysis so our data does not show the effect of these imperfections.

3.1.2 Comparing Resolutions to EC Residuals

In order to further validate our results, electromagnetic calorimeter residuals were computed for ten thousand 6 GeV electron events. The EC residuals are the differences between the hit position evaluated by the calorimeter and the coordinates of the reconstructed trajectory at the EC. The residuals should be similar to the reconstruction resolutions as they also represent how accurately the reconstruction software evaluated the trajectory at the EC. Each event has a data bank that contains the hit coordinates evaluated by the calorimeter and the coordinates of the trajectory at the EC. The residuals of the x, y and z-coordinate at the inner EC for the 10 000 events were computed and plotted in histograms. The exact layer where the residuals are obtained changes as the z-coordinate of clusters is determined from the layer with the maximum energy deposition [34]. These histograms are seen in Figure 3.3. The widths

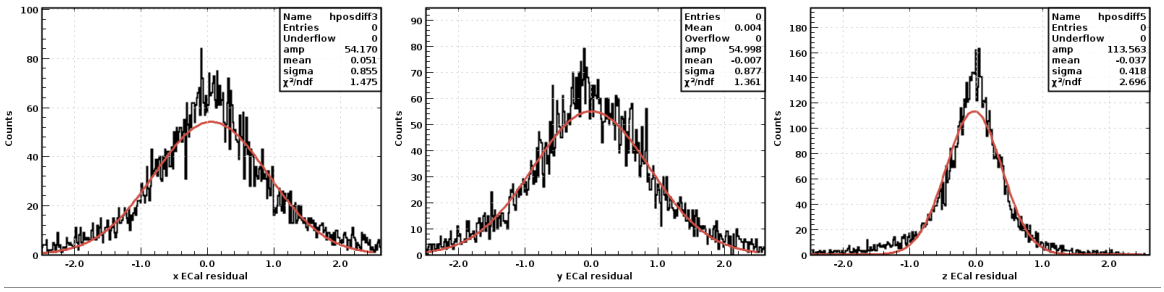

Figure 3.3: A plot of the EC x, y, and z-residuals for a 6 GeV e^- beam.

of these histograms are slightly larger than the spatial resolutions obtained at the EC in this study. The EC residuals are: $\sigma_x = 0.855$cm, $\sigma_y = 0.877$cm, $\sigma_z = 0.418$cm, while the resolutions of the reconstruction software at the EC for the same event file are: $\sigma_x = 0.786 \pm 0.007$cm, $\sigma_y = 0.548 \pm 0.005$cm, $\sigma_z = 0.393 \pm 0.003$cm. The resolu-

tions obtained by fitting histograms produce results that are very similar in size to the detector residuals, which further validated our method. The negative tails in the x and z-residuals look similar to the tails seen in histograms of differences in observables obtained in this study. This indicates that the momentum inaccuracies in forward tracking due to synchrotron radiation also affect the process of hit matching when the tracks are swum from the DCs to the other detectors. Therefore, the obtained reconstruction resolutions could also be used to check and validate the criteria for matching the DC track to hits in other detectors.

3.2 Varying the Beam Species and Energy

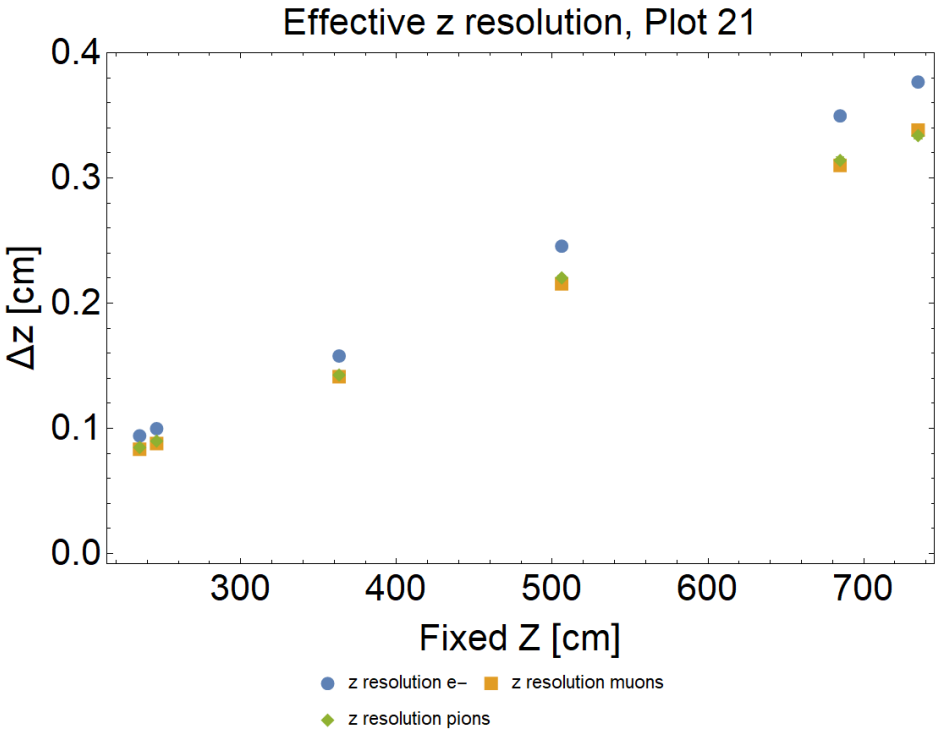

Figure 3.4: The z-resolution plotted against the z-axis distance to the endpoints in the tilted frame. The blue points represent electrons, the yellow points muons, while the green points represent pions.

In order to track how the resolutions vary for different particle species, 10 000 events with a 6 GeV π^- beam were created. The events were reconstructed, the two tracks were swum for each event and the resolutions were obtained. The resolutions

were plotted against the z-axis distance to the endpoints and compared to the aforementioned electron and muon resolutions. The results are shown in Figure 3.4 and in Appendix B.4. The pion and muon events have lower resolutions because they

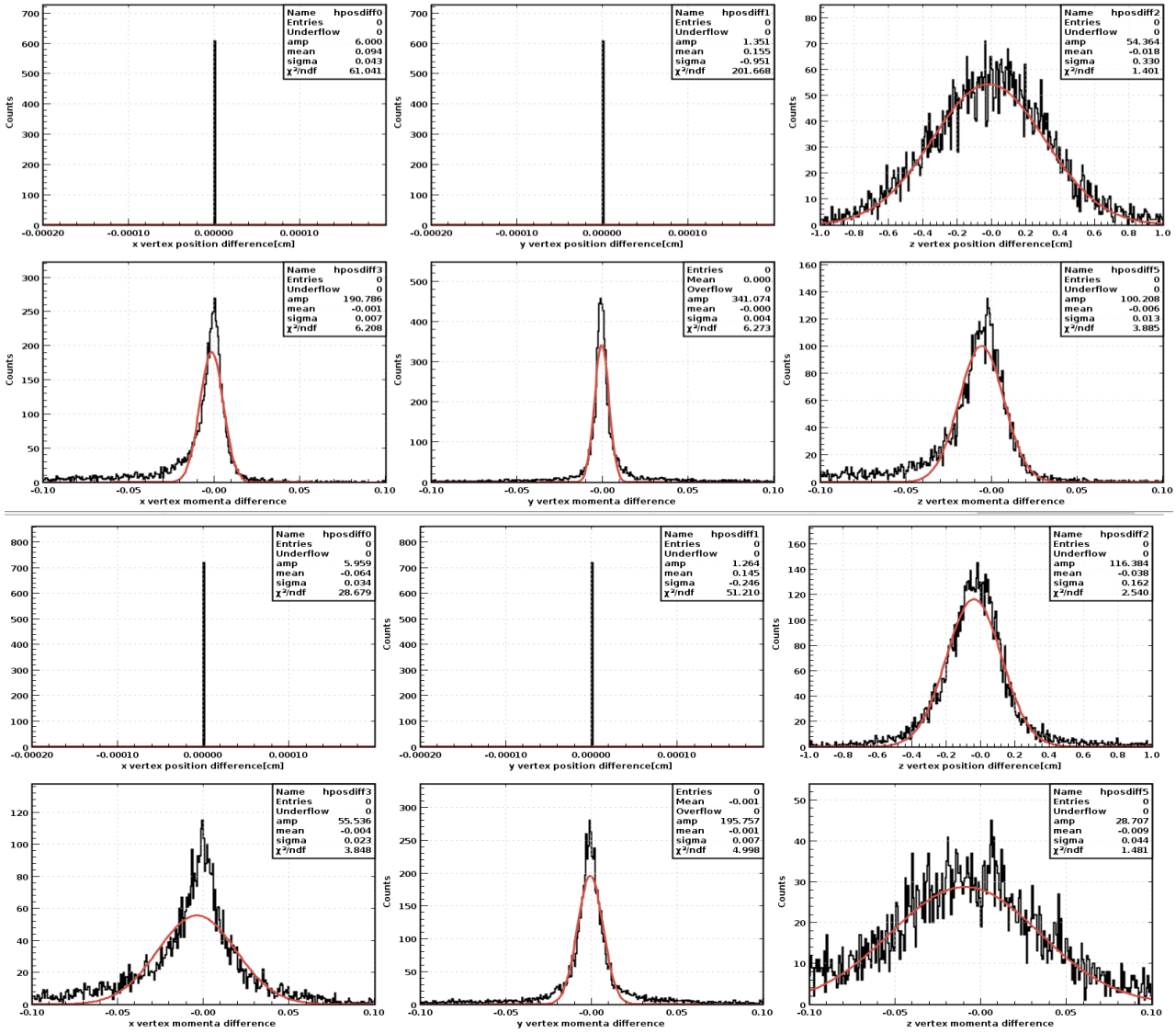

Figure 3.5: The histograms of vertex differences in the x, y, and z position and the momentum components for a 3 GeV beam are shown in the upper two rows, while the same histograms for a 9 GeV beam are shown in the two rows at the bottom.

are particles of higher mass that are therefore less affected by synchrotron radiation (equation 2.4). This comparison revealed that the radiation has a significant effect

on the resolution calculations, a $10 - 20\%$ increase is seen in the resolutions of all observables when the beam particles are electrons. The next point of interest in our study was the dependence of the resolutions on particle energy. 10 000 electron events were created in 1.5GeV increments for this purpose, with the lowest energy electrons having $E = 3$GeV. A minimum in the momentum resolution of the CLAS12 detector is reached at about 3 GeV/c, the resolution increases for more energetic particles than this [34]. This is due to the fact that particles with higher momentum are bent less by the torus and the track curvature resolution increases. The aforementioned synchrotron radiation will also affect the higher energy electrons more due to the dependence on the fourth power of particle energy (equation 2.4). Even though the momentum resolution increases for more energetic particles, they will produce lower, better resolutions. To understand why this happens, the spatial resolution of the

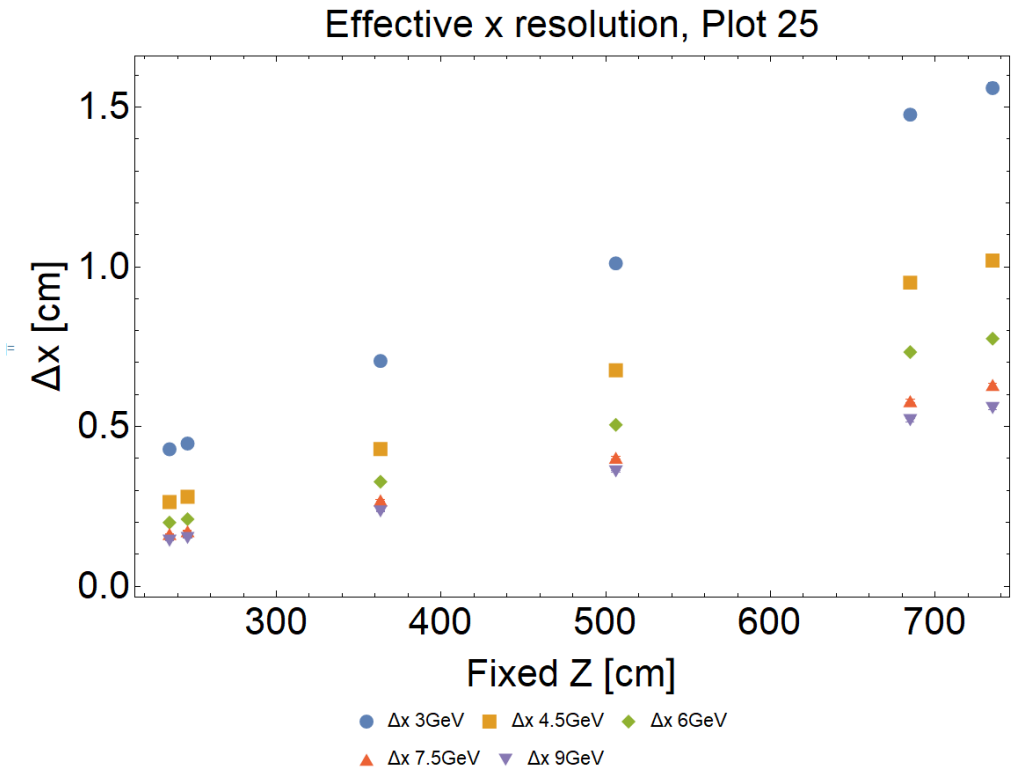

Figure 3.6: The x-resolution plotted against the z-axis distance to the endpoints in the tilted frame plotted for 3 GeV, 4.5 GeV, 6 GeV, 7.5 GeV and 9 GeV electron beams.

Drift Chamber cells and their dependence on particle energy must be considered. On average, the energy transfer per collision with electrons of the DC medium increases as the energy of the beam particle increases [33]. The probability of multiple scatter-

ing of the ionized electrons decreases as the energy of the ionized electrons increases [33]. Therefore, electrons of the DC medium ionized by higher energy beams are more energetic and scatter less when travelling towards the anode. The consequence of this is a smaller uncertainty in determining the Distance of Closest Approach (DOCA) of the particles to the wire cells, which therefore improves the spatial resolution of each cell. Figure 3.5 shows how these influences affect the vertex resolutions, the vertex differences in position and momentum for the 3 GeV and 9 GeV beams are shown. The momentum estimate is less accurate for a higher energy beam due to the track curvature resolution and synchrotron radiation: the bottom most row shows the 9 GeV momentum differences, 3 GeV momentum differences are in the second row. This is also confirmed by independent measurements, the momentum resolution increases with beam momentum [34]. The z-coordinate estimate of 9 GeV electrons is more accurate due to a cleaner signal in the DCs: the 9 GeV spatial differences are in the third row, 3 GeV spatial differences are in the first row. The results of swimming

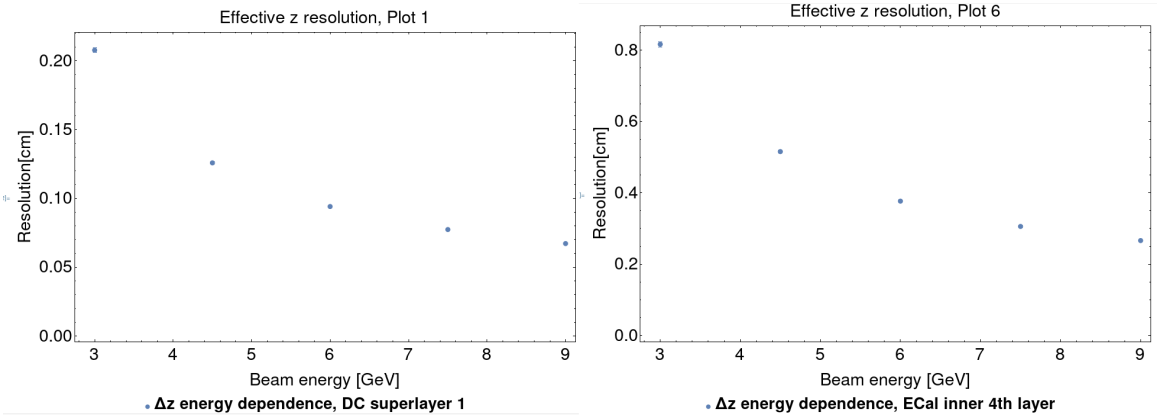

Figure 3.7: The z-resolution plotted against the particle energy on the x axis, the left plot shows how the resolution depends on beam energy in the first DC region, the right plot shows the same at the calorimeter.

particles with different momenta are seen in Figure 3.6 and in the figures in Appendix B.5: as expected, the resolutions decrease with increasing beam energy. In Figure 3.7, the z-coordinate resolution is plotted against the beam energy at two endpoints, the first DC superlayer and the calorimeter. At the first endpoint, the resolution of the 9 GeV beam is a factor of 3 smaller than the 3 GeV beam resolution, which increases to a factor of 4 at the calorimeter. The lower energy beams see a steeper increase in resolution as they travel further away from the target.

3.3 Resolutions for Different Detector and Magnet Configurations

The capabilities of the subsystems of CLAS12 change with the age of the components and with their placement within the detector array. Engineering surveys are therefore conducted after a large period of down time: the accelerator runs for a few weeks at a time once or twice a year, so these surveys are conducted before each experimental run. The detectors are shifted to improve their performance, and those

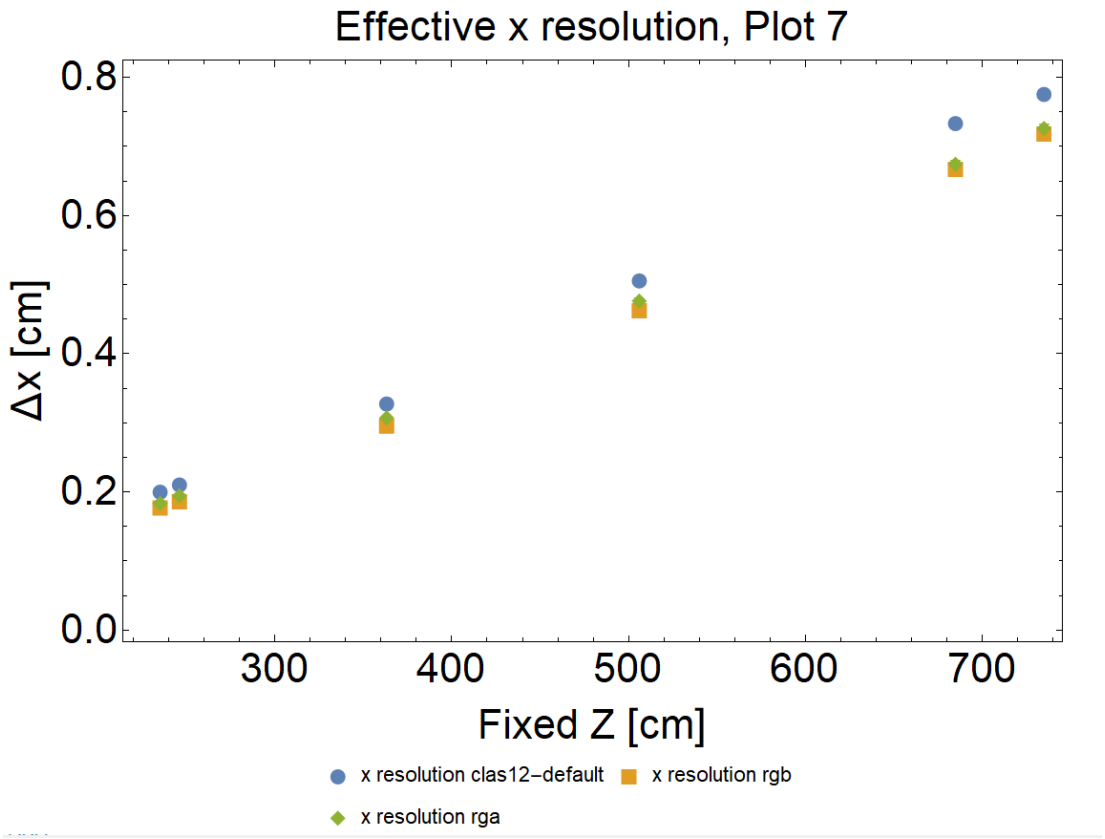

Figure 3.8: The x-resolution plotted against the z-axis distance to the endpoints in the tilted frame. The blue points represent events created with the ideal geometry, the yellow points show events with the Run Group B configuration, while the green points represent events created with the Run Group A configuration.

shifts in detector positions are stored as differences compared to the ideal values. Any changes in detector properties such as radiation lengths and light propagation times are measured by performing calibration runs. These differences compared to the ideal

configuration are inputted at the start of simulation and reconstruction with a text file. The specifics of each detector configuration can be found at the following page: `https://github.com/gemc/clas12Tags/tree/master/4.4.0/config`. All the analysis that was conducted above was done exclusively on events created with the ideal CLAS12 geometry. Therefore, 10 000 events were created with the Run Group A (RGA) configuration, and additional 10 000 were created with the Run Group B (RGB) configuration. These detector setups from 2019 recorded data in a time period that was very close to one another, and the two configurations do not differ in the positions of the detectors. Compared to the ideal geometry, the target and the Central Detector are shifted 3 cm upstream (beam direction is downstream) and the HTCC is shifted 2 cm upstream. Additionally, the Forward Tagger, a detector that detects particles scattering at small polar angles, and the Forward Micromegas Tracker, a detector that aids in vertex reconstruction, are both turned on [22] [47]. The only difference between the two configurations is the target: the RGA configu-

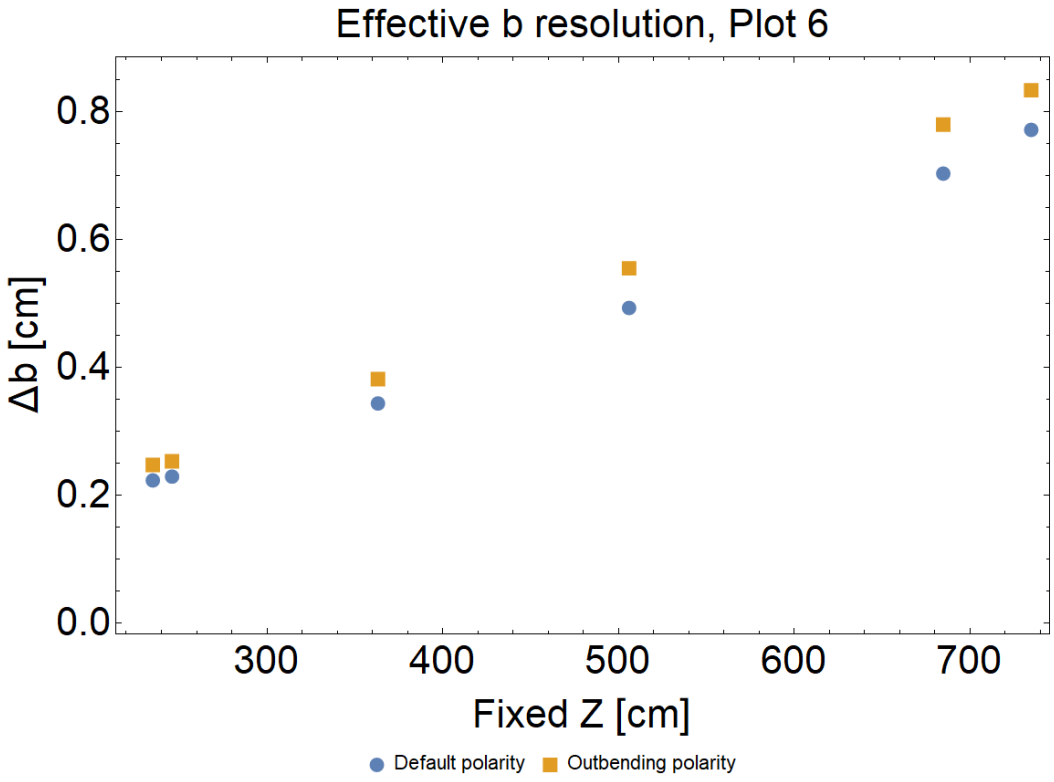

Figure 3.9: The impact parameter resolution plotted against the z-axis distance to the endpoints in the tilted frame. The blue points represent events created with the in-bending torus polarity, while the yellow points represent events created with the out-bending torus configuration.

ration file specifies liquid hydrogen as the target, while the RGB file has deuterium as the target. The GEMC internal event generator is used throughout this study to obtain the vertex positions and momenta of beam particles at the start of simulation, so the target variation has no effects on the resolutions. The electrons were created with 6 GeV of energy. Due to the similarities between the two run groups, the resolutions should look almost identical. Small discrepancies due to the angular spread at the vertex should again be seen as in the resolutions in different detection sectors. Figure 3.8 confirms this, the x-resolutions of the two run group event files are shown next to events created with the ideal geometry in the figure. The resolutions of other observables can be found in Appendix B.6. The run group resolutions are lower than the resolutions of events created with the ideal geometry, which is expected. The researchers used GEMC to improve the performance of the detector by finding the ideal hardware setup and placement for each run group [41]. The effects of future engineering surveys and new detector configuration files on the accuracy of reconstruction can thus be studied with the algorithm developed in this study. Results presented in the paragraphs below will all be created with the default geometry unless specified otherwise.

Another series of measurements that were conducted studied the resolutions when the torus field polarity was flipped. Some experiments are conducted with an out-bending torus magnet for negatively charged particles, which affects the resolutions. The beam electrons are bent towards the edges of the CLAS12 detector, where the magnetic field strength decreases and the track curvature resolution (and consequently the momentum resolution) increases. Therefore, events created with an out-bending torus configuration should have higher values of resolution. This is exactly what is observed when events with an out-bending torus are created in GEMC and are swum to the subsystems of CLAS12: the plot of the impact parameter resolution is seen in Figure 3.9. The plots of resolutions of the remaining observables can be found in Appendix B.7. Events mentioned in the paragraphs below will all be created with the default, in-bending configuration, unless specified otherwise.

3.4 Resolutions After the GEMC Software Update

Versions of GEMC released prior to the summer of 2020 simulated detector responses that resulted in more accurate results than the experimental data. The discrepancies between the simulated and real detector responses were identified, and the issues were resolved in the new version of the software, version 4.4.0. The GEMC code repository and the summary of changes made to each software version can be found here: `https://github.com/gemc/clas12Tags`. The smearing of the Distance Of Closest Approach (DOCA) of particles to the DC wire cells is the change that had the most impact on the reconstruction resolutions. When the arrival time of ionized

electrons at the DC wires is measured in an experiment, multiple scattering causes a broadening of the time signal and a decrease in the measured current pulse [33]. Due to the width of the Time-to-Digital Converter (TDC) response, there is an uncertainty in determining the drift time of ionized electrons. Consequently, the Distance Of Closest Approach (DOCA) of the particle to the wire is smeared. The DOCA circles

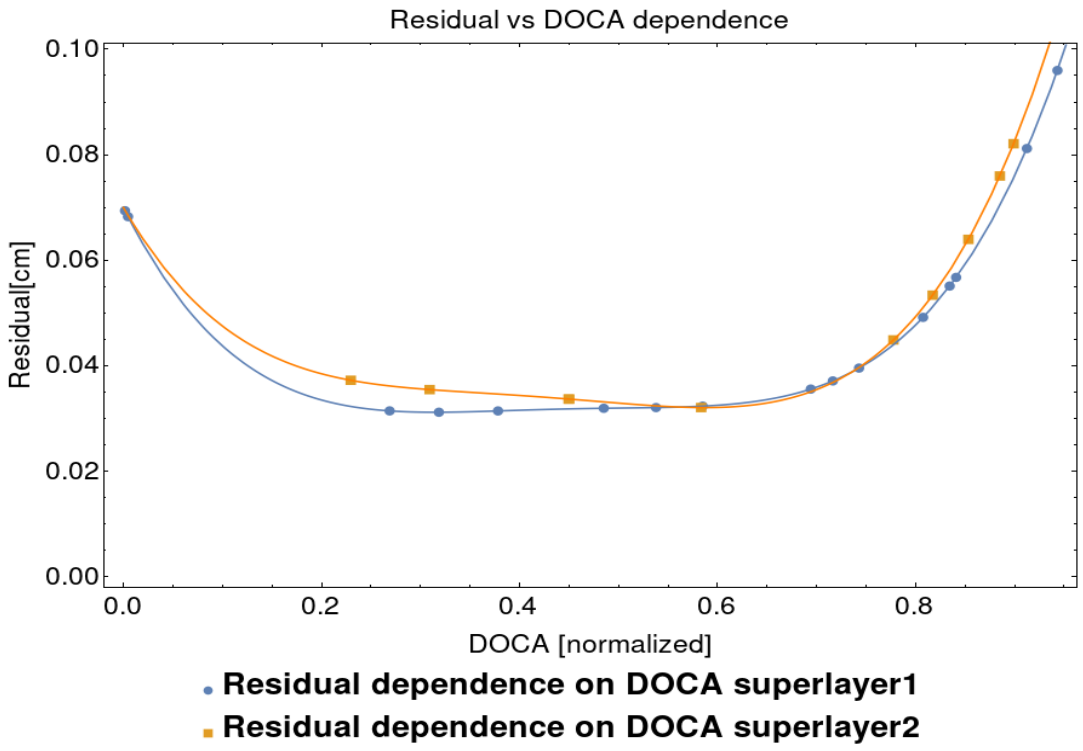

Figure 3.10: The residual of DC cells plotted as a function of the Distance Of Closest Approach (DOCA), the distance obtained from the arrival time measurements at the wires. The two functions plotted here show this dependence in the first (blue) and second (orange) superlayer of the Drift Chambers. The parameter of the polynomials are obtained from the CCDB.

and their uncertainties are the measurements that are fitted by the Kalman Filter in Time-Based Tracking, so the addition of this smear to the simulated detector outputs should significantly affect the reconstruction of simulated events. The smear in the DOCA is implemented by measuring the cell resolution from real data, an event file from the spring 2019 Run Group A experimental run was used. The closest distance between the reconstructed trajectory at a cell and the DOCA circle obtained at that cell from the measured arrival time is the resolution of the cell, which will be referred to as a residual from here on. The residuals are measured as a function of the DOCA

of particles since the resolution of cells changes with the closest distance that the beam particle passed by the anode wire. Figure 3.10 shows the residual dependence on the DOCA of the beam particle. An increase in the wire cell resolution is seen as the

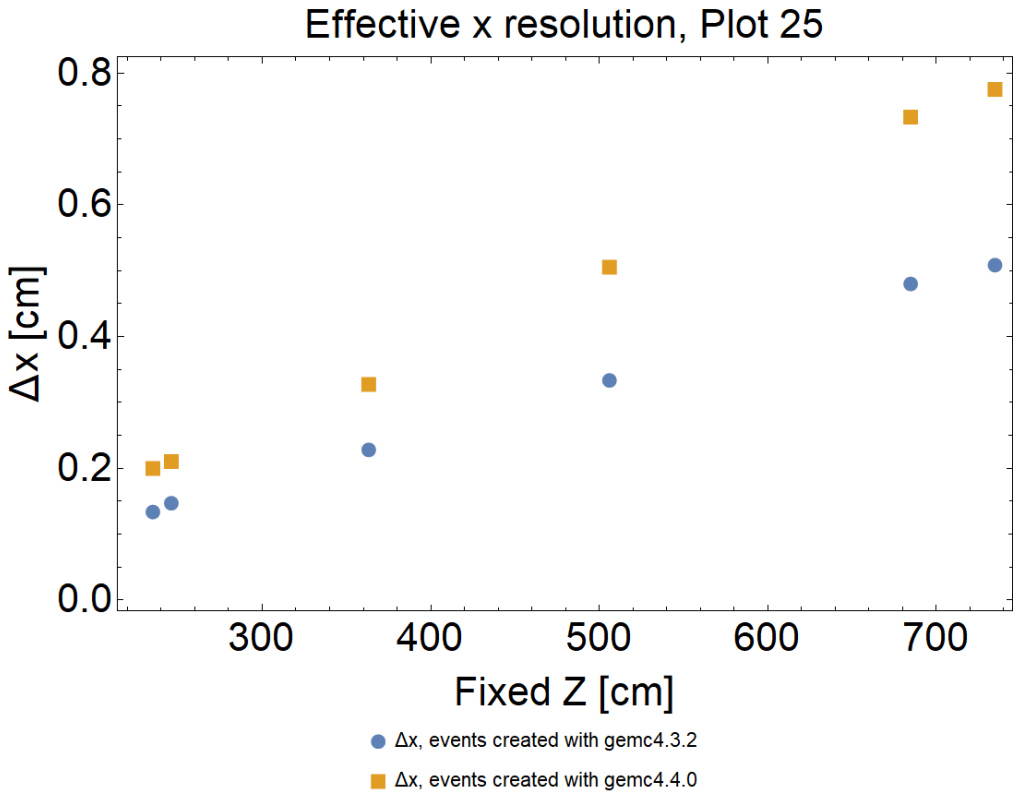

Figure 3.11: The x-resolution plotted against the endpoint distance along the z axis in the TSCS. The blue points show the results obtained using an event file created with the old version of the simulation software, while the yellow points show the resolution obtained from the event file created with the new version of the simulation software.

DOCA increases. If the ionized electrons have to travel further through the medium to get to the anode wire, the probability of multiple scattering is greater, and the uncertainty in the measurement of the exact time of arrival is larger. Additionally, geometric corrections need to be applied at the cell edges due to their hexagonal shape: the cells are approximated as spheres in reconstruction calculations, which is valid throughout the volume of the cell except at the edges [25]. On the other hand, when the DOCA is very small, the particle will pass through the centre of the cell. The electrons ionized closer to the centre of the cell will arrive at the anode wire much quicker than the electrons ionized at the edge of the cell, at the point where the beam particle entered/exited the cell. This causes a broadening of the time signal and an

increase in the residual for smaller values of DOCA. The polynomials that were fitted

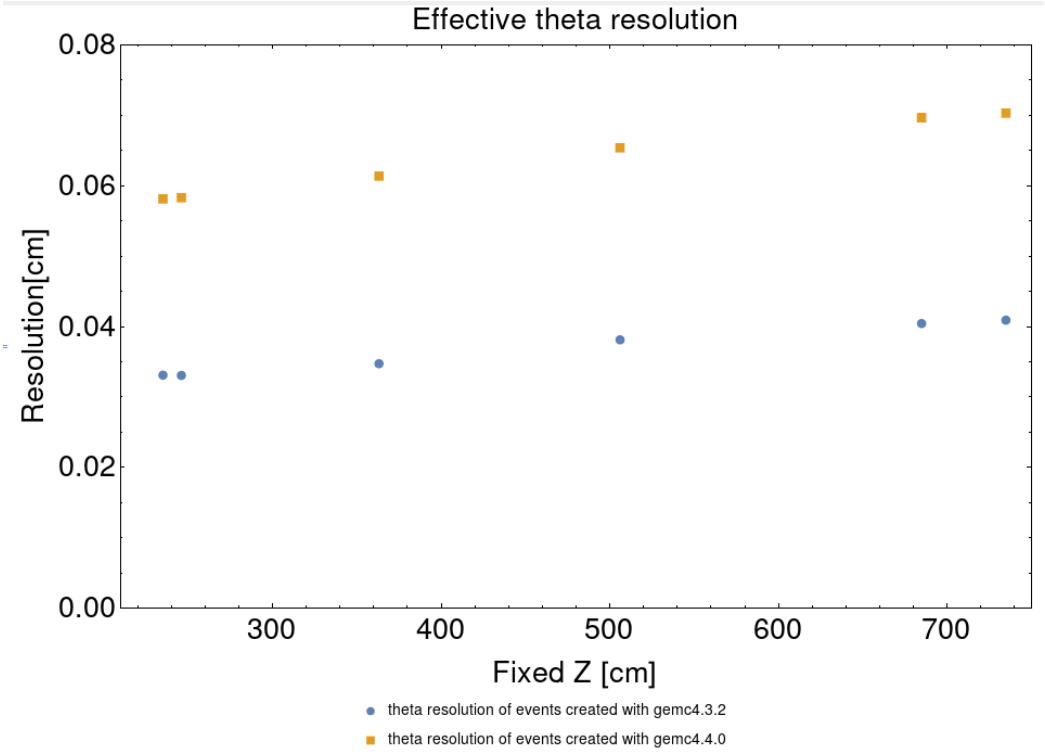

Figure 3.12: The theta resolution in degrees plotted against the endpoint distance along the z axis in the tilted coordinate system. The blue points show the results obtained using an event file created with the old version of the simulation software, while the yellow points show the resolution obtained from the event file created with the new version of the simulation software.

to the measured residuals differ for each DC superlayer, as seen in Figure 3.10. This is due to the fact that the strength of the magnetic field varies in each superlayer. The magnetic field strength affects the drift velocity of ionized electrons [33], which in turn affects the cell resolution dependence on the DOCA. The parameters of the polynomials are stored in Jefferson Lab's Calibration Constants Database (CCDB). The DOCA at each cell is what is calculated first in each Geant4 step in the DCs in simulation, and the obtained distance is smeared with the aforementioned polynomials [41]. The drift time is then obtained with the inverse of the time-to-distance function used in reconstruction [41]. The drift time is used to construct a Landau function that approximates the TDC response [41]. The Landau distribution has a large positive tail that mimics the tails seen in the TDC response functions that appear due to multiple scattering. The resulting signals are broader than the previous simulated

TDC responses produced by older versions of GEMC. CLARA calculates from these broader time signals the best estimate of the distance of closest approach to the wires, which results in more realistic data as the uncertainty in the DOCA is now greater. The exact effect of the software changes on the resolutions can be seen in Figure 3.11. Much like the x-resolution, the other resolutions saw a 50% increase for event files created with the new version of GEMC. Figure 3.12 is an example of the change in angular resolutions, and the remaining plots can be found in Appendix B.2. The previous plots that were shown in this paper all feature data created with the new GEMC software, all the analysis was redone after the new version of the software was released. The increase in the resolution stays around 50% for all events, irrespective of the beam energy, particle species, etc.
Another feature that was added in the new COATJAVA release along with the new version of GEMC was the background merger utility. This utility allows the merging

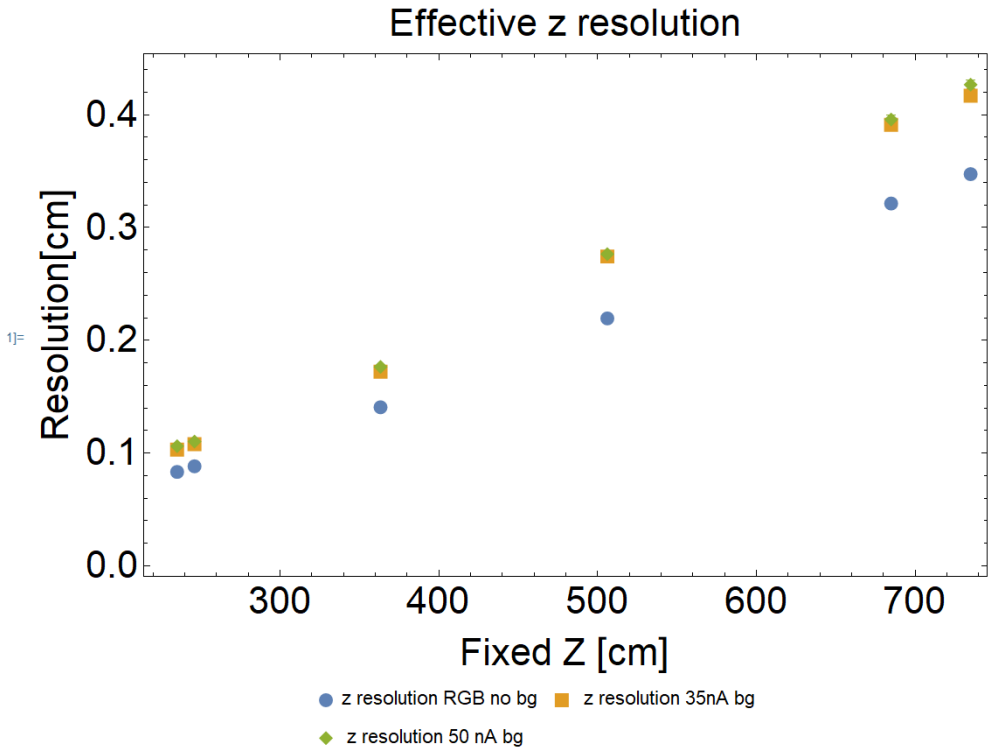

Figure 3.13: The z resolution in cm plotted against the endpoint distance along the z axis in the tilted coordinate system. The blue data set are simulated RGB events with no background, while the yellow and green are events with 35nA and 50nA backgrounds merged prior to reconstruction.

of background events with a simulated event file. The beam operates at a luminosity

of up to 10^{35} events/s/cm^2, which results in Moller scattering of beam electrons on the electrons of the target material [19]. The detectors capture these background particles together with the relevant scattering products in a real experiment. Fast triggers are necessary to capture the relevant interactions and to reject hits of Moller electrons, cosmic rays and other background between two events [48]. In order to create files for the background merger service, data was collected at each detector with random triggers at different values of the beam current during different experimental runs. The use of a random trigger results in the capturing of background events that are usually rejected in-between relevant beam electron scattering events. A file containing 10 000 background events from an RGB experimental run at 35 nA and 50 nA beam current were merged with an event file. The event file contained 10 000 beam electrons simulated with the same detector configuration at 6 GeV energy and at the standard values of the vertex angles and z-coordinate. The merged file was then processed by the reconstruction software. The particles were swum and the z-resolutions are seen in Figure 3.13. The resolutions of the remaining observables are found in Appendix B.8. Due to the greater occupancy of the DCs when background events are merged, the performance of the pattern recognition and noise removing algorithms worsens, which increases the resolutions [19]. The amount of background electrons created by Moller scattering increases with the beam current as more electrons are impinging on the target material. This results in an increase in the resolution for higher beam currents. A more detailed discussion on the effects of background on the detector resolutions can be found in Section 10 in [19]. The increase in the resolutions seen in Figure 3.13 matches the increase seen in [19]: the z-coordinate increase is 27% for swum particles at the first DC superlayer for a 50 nA beam, while the increase in the vertex z-coordinate in [19] is 31% for a 60 nA beam.

Chapter 4

Discussion & Conclusions

The resolution of the CLAS12 reconstruction software was obtained at the subsystems of the Forward Detector. The resolutions were obtained by swimming particles from their generated and reconstructed vertices of interaction. The state vectors of the two tracks were collected at the following locations: the High Threshold Cherenkov Counter, the three Drift Chamber regions, the Forward Time-Of-Flight system, and the electromagnetic calorimeter. The resolution of six observables was obtained for each set of events: the resolutions of the spatial coordinates and the angles theta and phi were obtained in the Lab coordinate system, and the impact parameter resolution was computed in the Tilted Sector Coordinate System. The distributions of differences in observables at the endpoints were fitted with multiple Gaussian functions to capture both the central peak and the wide tail of the distributions. The cause of the tails in endpoint distributions was identified: the effect of synchrotron radiation was unaccounted for during reconstruction, which resulted in underestimations of particle momentum at the vertex. The method of swimming particles from their vertices and using multiple functions to fit the distributions of differences was validated by swimming in different detection sectors of CLAS12. The results were similar at each endpoint, which validated our method. The reconstruction resolutions were then compared to the electromagnetic calorimeter residuals: the obtained residuals were very close in value to the resolutions at the calorimeter, which further validated our method. The resolutions obtained for different particle species and different beam energies agree with theoretical predictions. The resolutions improve for particles with higher mass due to a lesser influence of radiative effects and they improve with increasing beam energy, even though the momentum resolution worsens. When events are created with different detector configurations and a reversed torus polarity, the resolutions follow expected trends. There is little variation in the run groups A and B and the results improve compared to the default geometry. The resolutions increase for an out-bending field polarity as the magnetic field strength drops off at the edges of

the forward region and the track curvature resolution increases. Events created with the new version of GEMC, 4.4.0, see an increase in the resolution due to the more realistic digitization routines employed in the new version of the simulation software. Finally, the resolution increases when background events are merged to a simulated event file, and the size of this increase matches measurements in [19].
The angular resolutions obtained in this study were compared to the resolutions of the CLAS12 detector seen in Table 2 in the CLAS12 paper [19]. 10 000 6GeV electron beam events scattered at the standard angles and values of the vertex z-coordinate were used for the comparison ($-30° < \phi < 30°$, $5° < \theta < 35°$, $-2.5 < z < 2.5$). The phi resolution at the first DC superlayer equals $\sigma_\phi = 0.156° = 2.72 \pm 0.02$mrad and the theta resolution equals $\sigma_\theta = 0.058° = 1.01 \pm 0.008$mrad, both are within the constraints given by [19]. If the momentum loss due to synchrotron radiation is calculated during reconstruction, the resolutions would significantly improve and would be closer to the values obtained for pions and muons at the same energy (Figure 3.4). Synchrotron radiation is simulated in Geant4 as described in [49]. The algorithm that simulates the effect of the radiation can be found at the following link: `http://hurel.hanyang.ac.kr/Geant4/Doxygen/10.02.p02/html/d3/d2f/_g4_synchrotron_radiation_8cc_source.html`. The Lorentz factor, the mass of the particle and the cross product of the momentum and the magnetic field strength are inputted into the *GetRandomEnergySR* method: this method calculates the emitted energy of synchrotron radiation for that interval. The irradiated energy is obtained from the photon spectrum of the radiation [49]:

$$\frac{d^2N}{dxds} = \frac{\sqrt{3}\alpha}{2\pi}\frac{eB_\perp}{mc}\int_x^\infty K_{5/3}(\xi)d\xi \tag{4.1}$$

α denotes the fine structure constant, x is the photon energy expressed in units of the critical photon energy (the energy above which half the power is radiated), s is the path length and $K_{5/3}$ is a modified Bessel function of the third kind. The integral of this Bessel function is approximated by finding the inverse of the cumulative distribution of the function: this function is then approximated with Chebyshev polynomials and multiplied by the critical photon energy to obtain the total irradiated energy [49]. The direction of the radiation is then evaluated (photons are emitted in a cone in the direction of motion), and the particle momentum is finally updated [49]. To implement this method in the reconstruction process, the momentum loss due to the radiation would need to be computed at every step during the Kalman Filter fitting process. The greatest challenge in implementing this method is time consumption: tracking already takes up over 90% of the time it takes to reconstruct events. The Software Working Group at Hall B is currently focusing their efforts to reduce the reconstruction time [50], so the implementation of these calculations in the fitting process is unlikely. An alternative method to correct the momentum estimate could

be implemented if a study is conducted on the dependence of the radiation on the vertex angles and energy. To clarify, events could be created at different values of the vertex angles and energy, for example in five degree angular bins and 0.5 GeV energy bins. The differences in the simulated and reconstructed vertex momentum components could then be computed as a function of the vertex track angles and energy. The vertex angles and energy could then be inputted into this function for a simple numerical correction to the vertex momentum components. A more accurate vertex momentum estimate would improve the accuracy of experimental results. For example, if the accuracy of the vertex electron momentum in the Bonus12 experiment improves [14], the estimation of the neutron momentum improves, and therefore the structure function of the neutron is determined more accurately.

The method outlined in this study can be used in the future to test the effect of

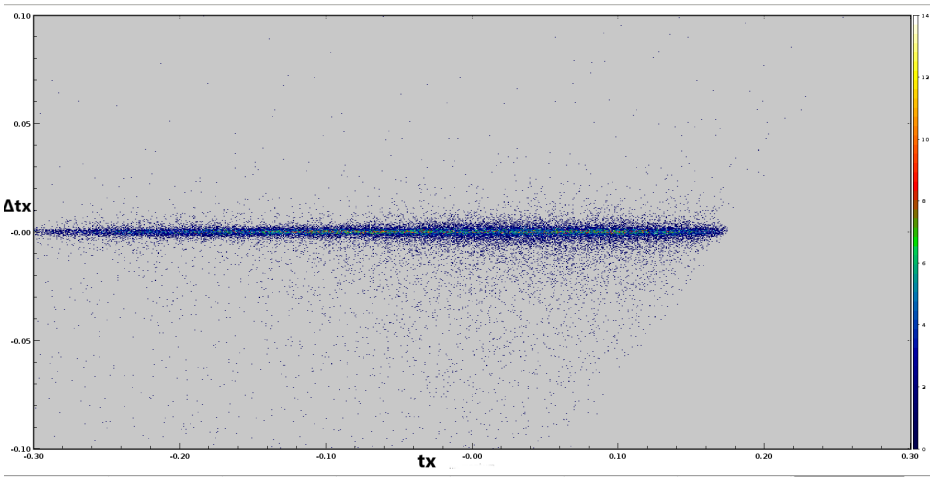

Figure 4.1: Figure 4.1: A plot of the $t_x = \frac{p_x}{p_z}$ resolution against the t_x of the track that was swum from the reconstructed vertex to the first wire layer in the first superlayer of the Drift Chambers.

adding new elements to the reconstruction chain. The results can also be used as benchmark values when engineering surveys are conducted and individual subsystems are shifted for optimised performance. Finally, the resolutions can be used to initialize the state vector covariance matrix that computes the weights of individual measurements in the Kalman Filter fitting process in the DCs. The matrix elements are obtained by comparing measurements in an iterative manner (equation 2.2) and by adding measurement noise due to multiple scattering [35]. This requires an assignment of uncertainties to the first measurement at the first wire layer of the DCs, where the Kalman Filter doesn't have previous measurements to compare. Currently, fixed values are used for uncertainties in all five track parameters at the first DC layer [51]. If true resolutions are used as the values that initialize the covariance matrix,

this could improve the speed and accuracy of the fitting process [37]. The algorithm developed in this study can be used to compute the resolutions of the five variables comprising the state vector $(x, y, tx, ty, Q = \frac{q}{p})$ as a function of each of the state vector parameters at the first DC layer. The state vector obtained at the first measurement site in reconstruction would then be inputted into this function to obtain the uncertainty in the first measurement. An example of one two-dimensional histogram is shown in Figure 4.1, where the t_x-resolution is plotted against t_x, the value of the x-direction cosine of the swum track at the first wire layer of the Drift Chambers. To obtain the dependence of the resolutions on the track parameters, 25 such histograms need to be produced and fitted: the resolution of each parameter must be obtained as a function of each track parameter. As seen in the Figure, a much larger amount of events than the amount used here (50k) would need to be swum to the first DC layer to obtain a function with acceptable statistical errors.
The four scripts that swim particles to four detectors, the script that fits the resulting histograms, and the Mathematica notebook containing all the results gathered throughout the course of this study can all be found at the following link:
`https://drive.google.com/drive/folders/1sg02PmmbRd3F1wVaezUyEdCTnjpFT6Xa?usp=sharing`.

References

[1]E. D. Bloom, D. H. Coward, H. DeStaebler, J. Drees, G. Miller, L. W. Mo, R. E. Taylor, M. Breidenbach, J. I. Friedman, G. C. Hartmann, and H. W. Kendall, "High-Energy Inelastic $e-p$ Scattering at 6° and 10°", Phys. Rev. Lett. **23**, 930–934 (1969) 10.1103/PhysRevLett.23.930.

[2]National Science Advisory Committee, *A Long Range Plan For Nuclear Science*, https://science.osti.gov/-/media/np/nsac/pdf/docs/1979_Long_Range_Plan.pdf?la=en&hash=C5FC769ACD98681FA97D893A1B2F0355793684A3, [Online; accessed 22-June-2020], 1979.

[3]J. Lab, *Jefferson Lab to Mark the End of CEBAF 6 GeV Operations on May 18* (2012 (accessed October 16th, 2020)), https://www.jlab.org/news/releases/jefferson-lab-mark-end-cebaf-6-gev-operations-may-18.

[4]C. W. Leemann, D. R. Douglas, and G. A. Krafft, "THE CONTINUOUS ELECTRON BEAM ACCELERATOR FACILITY: CEBAF at the Jefferson Laboratory", Annual Review of Nuclear and Particle Science **51**, 413–450 (2001) 10.1146/annurev.nucl.51.101701.132327.

[5]J. Seely et al., "New Measurements of the EMC Effect in Very Light Nuclei", Phys. Rev. Lett. **103**, 202301 (2009) 10.1103/PhysRevLett.103.202301.

[6]I. G. Aznauryan et al. (CLAS Collaboration), "Electroexcitation of Nucleon Resonances from CLAS Data on Single Pion Electroproduction", Phys. Rev. C **80**, 055203 (2009) 10.1103/PhysRevC.80.055203.

[7]S. Stepanyan, K. Hicks, D. S. Carman, E. Pasyuk, R. A. Schumacher, E. S. Smith, D. J. Tedeschi, L. Todor, G. Adams, P. Ambrozewicz, and et al., "Observation of an Exotic $S = +1$ Baryon in Exclusive Photoproduction from the Deuteron", Physical Review Letters **91** (2003) 10.1103/physrevlett.91.252001.

[8]Y. Prok, P. Bosted, N. Kvaltine, K. P. Adhikari, D. Adikaram, M. Aghasyan, M. J. Amaryan, M. D. Anderson, S. Anefalos Pereira, H. Avakian, and et al., "Precision Measurements of g_1 of the Proton and of the Deuteron with 6 GeV Electrons", Physical Review C **90** (2014) 10.1103/physrevc.90.025212.

[9]D. Adikaram, D. Rimal, L. B. Weinstein, B. Raue, P. Khetarpal, R. P. Bennett, J. Arrington, W. K. Brooks, K. P. Adhikari, A. V. Afanasev, and et al., "Towards a Resolution of the Proton Form Factor Problem: New Electron and Positron Scattering Data", Physical Review Letters **114** (2015) 10.1103/physrevlett.114.062003.

[10]J. Lachniet et al. (CLAS), "A Precise Measurement of the Neutron Magnetic Form Factor G_M^n in the Few-GeV^2 Region", Phys. Rev. Lett. **102**, 192001 (2009) 10.1103/PhysRevLett.102.192001.

[11]O. Gayou et al. (Jefferson Lab Hall A), "Measurement of G(Ep) / G(Mp) in $\overrightarrow{e}p \longrightarrow e\overrightarrow{p}$ to $Q^2 = 5.6GeV^2$", Phys. Rev. Lett. **88**, 092301 (2002) 10.1103/PhysRevLett.88.092301.

[12]C. Gal, "New Precision Measurement of the Neutral Weak Form Factor of ^{208}Pb", 2020 Fall Meeting of the APS Division of Nuclear Physics, 2020, https://hallaweb.jlab.org/parity/prex/201029_PREX2_CGal.pdf.

[13]C. J. Horowitz, S. J. Pollock, P. A. Souder, and R. Michaels, "Parity Violating Measurements of Neutron Densities", Phys. Rev. C **63**, 025501 (2001) 10.1103/PhysRevC.63.025501.

[14]M. Hattawy, M. Amaryan, S. Bültmann, G. Dodge, N. Dzbenski, C. Hyde, S. Kuhn, D. Payette, J. Poudel, L. Weinstein, R. Dupré, M. Guidal, D. Marchand, C. Muñoz, S. Niccolai, E. Voutier, K. Hafidi, Z. Yi, T. Chetry, L. El-Fassi, N. Baltzell, G. Gavalian, F. X. Girod, S. Stepanyan, I. Albayrak, E. Christy, A. Nadeeshani, N. Kalantarians, C. A. Gayoso, and D. Jenkins, *Neutron DVCS Measurements with BONuS12 in CLAS12*, 2019.

[15]S. Tkachenko, "Neutron Structure Functions Measured with Spectator Tagging", PhD thesis (Old Dominion University, 2009).

[16]A. Bogacz, *Introduction to Accelerators*, https://gspda.jlab.org/wiki/index.php/Main_Page#tab=Summer_Lecture_Series3, [Online; accessed 25-June-2020], 2020.

[17]Y. C. Chao, M. Drury, C. Hovater, A. Hutton, G. A. Krafft, M. Poelker, C. Reece, and M. Tiefenback, "CEBAF Accelerator Achievements", Journal of Physics: Conference Series **299**, 012015 (2011) 10.1088/1742-6596/299/1/012015.

[18]*CLASSE:SRF*, https://www.classe.cornell.edu/Research/SRF/SrfCavitiesAPrimerOne.html, Accessed: 2020-11-23.

[19]V. Burkert et al., "The CLAS12 Spectrometer at Jefferson Laboratory", Nucl. Instrum. Meth. A **959**, 163419 (2020) 10.1016/j.nima.2020.163419.

[20]R. Fair, N. Baltzell, R. Bachimanchi, G. Biallas, V. Burkert, P. Campero-Rojas, L. Elementi, L. Elouadrhiri, B. Eng, P. Ghoshal, J. Hogan, D. Insley, V. Kashikhin, D. Kashy, S. Krave, O. Kumar, M. Laney, R. Legg, V. Lagerquist, M. Lester, T. Lemon, A. Lung, C. Luongo, J. Matalevich, M. Mestayer, R. Miller, W. Moore, J. Newton, F. Nobrega, O. Pastor, S. Philip, R. Rajput-Ghoshal, V. Rao Ganni, C. Rode, N. Sandoval, S. Spiegel, D. Tilles, K. Tremblay, G. Velev, C. Wilson, M. Wiseman, and G. Young, "The CLAS12 Superconducting Magnets", Nuclear Instruments and Methods in Physics Research Section A: Accelerators, Spectrometers, Detectors and Associated Equipment **962**, 163578 (2020) https://doi.org/10.1016/j.nima.2020.163578.

[21]M. Antonioli et al., "The CLAS12 Silicon Vertex Tracker", Nuclear Instruments and Methods in Physics Research Section A: Accelerators, Spectrometers, Detectors and Associated Equipment **962**, 163701 (2020) https://doi.org/10.1016/j.nima.2020.163701.

[22]A. Acker et al., "The CLAS12 Micromegas Vertex Tracker", Nuclear Instruments and Methods in Physics Research Section A: Accelerators, Spectrometers, Detectors and Associated Equipment **957**, 163423 (2020) https://doi.org/10.1016/j.nima.2020.163423.

[23]D. Carman, G. Asryan, V. Baturin, L. Clark, R. De Vita, W. Kim, B. Miller, and C. Wiggins, "The CLAS12 Central Time-of-Flight System", Nuclear Instruments and Methods in Physics Research Section A: Accelerators, Spectrometers, Detectors and Associated Equipment **960**, 163626 (2020) https://doi.org/10.1016/j.nima.2020.163626.

[24]P. Chatagnon, J. Bettane, M. Hoballah, G. Hull, M. Imre, D. Marchand, B. Mathon, G. Murdoch, P. Naidoo, S. Niccolai, K. Price, D. Sokhan, and R. Wang, "The CLAS12 Central Neutron Detector", Nuclear Instruments and Methods in Physics Research Section A: Accelerators, Spectrometers, Detectors and Associated Equipment **959**, 163441 (2020) https://doi.org/10.1016/j.nima.2020.163441.

[25]M. D. Mestayer et al., "The CLAS12 Drift Chamber System", Nuclear Instruments and Methods in Physics Research Section A: Accelerators, Spectrometers, Detectors and Associated Equipment **959**, 163518 (2020) https://doi.org/10.1016/j.nima.2020.163518.

[26]Y. Sharabian, V. Burkert, A. Biselli, R. Badui, S. Christo, C. Cuevas, H. Dong, S. Danagoulian, A. Ellis, L. Elouadrhiri, B. Eng, K. Hafidi, I. Illari, G. Jacobs, J. Joo, K. Joo, D. Kashy, A. Kubarovsky, V. Kubarovsky, S. Maiylian, N. Markov, M. McClellan, M. McMullen, B. Miller, S. Miller-Smith, D. Nickolas, R. Niyazov, R. Paremuzyan, W. Phelps, V. Popov, J. Price, A. Puckett, B. Raydo, D. Riser, P. Stoler, A. Vlassov, and A. Voskanyan, "The CLAS12 High Threshold Cherenkov

Counter", Nuclear Instruments and Methods in Physics Research Section A: Accelerators, Spectrometers, Detectors and Associated Equipment **968**, 163824 (2020) https://doi.org/10.1016/j.nima.2020.163824.

[27]M. Ungaro, D. Anderson, G. Asryan, M. Antonioli, P. Bonneau, V. Burkert, S. Christo, M. Cook, B. Duran, B. Eng, A. Hoebel, D. Insley, J. Jacobs, S. Joosten, M. Leffel, T. Lemon, M. McMullen, Z. Meziani, R. Miller, P. Rojas, Y. Sharabian, and A. Yegneswaran, "The CLAS12 Low Threshold Cherenkov Detector", Nuclear Instruments and Methods in Physics Research Section A: Accelerators, Spectrometers, Detectors and Associated Equipment **957**, 163420 (2020) https://doi.org/10.1016/j.nima.2020.163420.

[28]M. Contalbrigo, V. Kubarovsky, M. Mirazita, P. Rossi, G. Angelini, H. Avakian, K. Bailey, I. Balossino, L. Barion, F. Benmokhtar, P. Bonneau, W. Briscoe, W. Brooks, E. Cisbani, C. Cuevas, P. Degtiarenko, C. Dickover, K. Hafidi, K. Joo, A. Kim, T. Lemon, V. Lucherini, R. Malaguti, R. Montgomery, A. Movsisyan, P. Musico, T. O'Connor, D. Orecchini, L. Pappalardo, C. Pecar, R. Perrino, B. Raydo, S. Tomassini, M. Turisini, and A. Yegneswaran, "The CLAS12 Ring Imaging Cherenkov Detector", Nuclear Instruments and Methods in Physics Research Section A: Accelerators, Spectrometers, Detectors and Associated Equipment **964**, 163791 (2020) https://doi.org/10.1016/j.nima.2020.163791.

[29]D. Carman et al., "The CLAS12 Forward Time-of-Flight system", Nuclear Instruments and Methods in Physics Research Section A: Accelerators, Spectrometers, Detectors and Associated Equipment **960**, 163629 (2020) https://doi.org/10.1016/j.nima.2020.163629.

[30]G. F. Knoll, *Radiation Detection and Measurement, 3rd ed.* 3rd edition (John Wiley and Sons, New York, 2000).

[31]E. Chudakov, *Electromagnetic Calorimeters*, https://userweb.jlab.org/~gen/talks/calor_lect_10.pdf, [Online; accessed 14-July-2020], 2020.

[32]G. Asryan et al., "The CLAS12 Forward Electromagnetic Calorimeter", Nuclear Instruments and Methods in Physics Research Section A: Accelerators, Spectrometers, Detectors and Associated Equipment **959**, 163425 (2020) https://doi.org/10.1016/j.nima.2020.163425.

[33]F. Sauli, "Principles of Operation of Multiwire Proportional and Drift Chambers", (1977) 10.5170/CERN-1977-009.

[34]V. Ziegler et al., "The CLAS12 Software Framework and Event Reconstruction", Nuclear Instruments and Methods in Physics Research Section A: Accelerators, Spectrometers, Detectors and Associated Equipment **959**, 163472 (2020) https://doi.org/10.1016/j.nima.2020.163472.

[35]G. Welch, G. Bishop, et al., *An introduction to the Kalman filter*, 1995.

[36]W. H. Press, S. A. Teukolsky, W. T. Vetterling, and B. P. Flannery, *Numerical Recipes in C*, 1988.

[37]V. Ziegler, "Application of Kalman Filters to Tracking in a Magnetic Field", Nuclear Physics Group Meeting, 2015, https://ww2.odu.edu/~skuhn/NucPhys/KalmanFilter.pdf.

[38]G. R. Lynch and O. I. Dahl, "Approximations to Multiple Coulomb Scattering", Nuclear Instruments and Methods in Physics Research Section B: Beam Interactions with Materials and Atoms **58**, 6–10 (1991) https://doi.org/10.1016/0168-583X(91)95671-Y.

[39]A. Spiridonov, "Optimized Integration of the Equations of Motion of a Particle in the HERA-B Magnet", (1998).

[40]V. Gyurjyan, D. Abbott, J. Carbonneau, G. Gilfoyle, D. Heddle, G. Heyes, S. Paul, C. Timmer, D. Weygand, and E. Wolin, "CLARA: A Contemporary Approach to Physics Data Processing", Journal of Physics: Conference Series **331**, 032013 (2011) 10.1088/1742-6596/331/3/032013.

[41]M. Ungaro et al., "The CLAS12 Geant4 Simulation", Nuclear Instruments and Methods in Physics Research Section A: Accelerators, Spectrometers, Detectors and Associated Equipment **959**, 163422 (2020) https://doi.org/10.1016/j.nima.2020.163422.

[42]S. Agostinelli et al. (GEANT4), "GEANT4–a simulation toolkit", Nucl. Instrum. Meth. A **506**, 250–303 (2003) 10.1016/S0168-9002(03)01368-8.

[43]J. Schwinger, "On the Classical Radiation of Accelerated Electrons", Phys. Rev. **75**, 1912–1925 (1949) 10.1103/PhysRev.75.1912.

[44]S. J. Miller, "The Method of Least Squares", Mathematics Department Brown University **8**, 1–7 (2006).

[45]F. James and M. Roos, "Minuit - a System for Function Minimization and Analysis of the Parameter Errors and Correlations", Computer Physics Communications **10**, 343–367 (1975) https://doi.org/10.1016/0010-4655(75)90039-9.

[46]L. Trailovic and L. Y. Pao, "Variance Estimation and Ranking of Gaussian Mixture Distributions in Target Tracking Applications", in Proceedings of the 41st IEEE Conference on Decision and Control, 2002. Vol. 2 (IEEE, 2002), pp. 2195–2201.

[47]A. Acker, D. Attié, S. Aune, J. Ball, P. Baron, M. Bashkanov, M. Battaglieri, R. Behary, F. Benmokhtar, A. Bersani, Q. Bertrand, D. Besin, T. Bey, P. Black, P. Bonneau, F. Bossù, R. Boudouin, M. Boyer, P. Campero Rojas, A. Casale, A. Celentano, R. Cereseto, A. Ciarma, F. Cipro, G. Charles, G. Christiaens, P. Contrepois, M. Cook, A. D'Angelo, R. De Vita, M. Defurne, E. Delagnes, E. Fanchini, S. Fegan, J. Fleming, A. Filippi, M. Garçon, F. Georges, K. Giovanetti, D. Glazier, R. Granelli, N. Grouas, K. Hicks, A. Hoebel, S. Hughes, C. Lahonde, L. Lanza, M. Leffel, T. Lerch, T. Lemon, K. Livingston, A. Manco, I. Mandjavidze, H. Mann, B. McKinnon, O. Meunier, R. Miller, G. Miní, Y. Mouden, P. Musico, M. Osipenko, G. Ottonello, F. Parodi, E. Pasyuk, P. Pollovio, F. Pratolongo, S. Procureur, R. Puppo, C. Rossi, M. Riallot, M. Ripani, A. Rizzo, F. Sabatié, C. Salgado, G. Smith, D. Sokhan, I. Stankovic, M. Taiuti, A. Trovato, M. Vandenbroucke, V. Vigo, E. Virique, D. Watts, C. Wiggins, N. Zachariou, and L. Zana, "The CLAS12 Forward Tagger", Nuclear Instruments and Methods in Physics Research Section A: Accelerators, Spectrometers, Detectors and Associated Equipment **959**, 163475 (2020) `https://doi.org/10.1016/j.nima.2020.163475`.

[48]B. Raydo, S. Boyarinov, A. Celentano, C. Cuevas, R. D. Vita, V. Kubarovsky, B. Moffit, S. Niccolai, R. Paremuzyan, and C. Smith, "The CLAS12 Trigger System", Nuclear Instruments and Methods in Physics Research Section A: Accelerators, Spectrometers, Detectors and Associated Equipment **960**, 163529 (2020) `https://doi.org/10.1016/j.nima.2020.163529`.

[49]H. Burkhardt, "Monte Carlo Generation of the Energy Spectrum of Synchrotron Radiation", (2007).

[50]G. Gavalian, P. Thomadakis, A. Angelopoulos, V. Ziegler, and N. Chrisochoides, "Using Artificial Intelligence for Particle Track Identification in CLAS12 Detector", ArXiv **abs/2008.12860** (2020).

[51]CLAS collaboration and others, "CLAS12 Technical Design Report", Jefferson Lab. Hall B, Newport News, VA, USA (2008).

Appendix A

Literature Review

Literature Review: Jefferson Lab's CLAS12 Detector & Its Reconstruction Software

URN 6464226
Department of Physics, University of Surrey,
Guildford GU2 7XH, United Kingdom

(Dated: July 27, 2020)

The following paper is a review of Jefferson Lab and the mass spectrometer located in Hall B, the CEBAF Large Acceptance Spectrometer, CLAS12, followed by a brief description of a research project that aims to obtain the reconstruction software resolution. The history of the facility and its main research goals are presented first. The basics of the accelerator are then described in short, after which comes a description of all the components of CLAS12. The reconstruction process in all the subsystems of CLAS12 is described in detail, as the results of this research project will be incorporated in the reconstruction routines. The Hall software packages are then briefly discussed, after which the methods of obtaining the reconstruction resolution are presented. The paper is concluded with a description of how the reconstruction resolutions will be integrated into the Hall reconstruction process to provide constraints on hit matching.

I. INTRODUCTION TO JEFFERSON LAB

The Thomas Jefferson National Accelerator Facility, referred to as JLab, is a linear accelerator facility that studies nucleon structure through electron scattering. It was built in the aftermath of the discovery of quarks at the Stanford Linear Accelerator. The United States National Science Advisory Committee (NSAC) recognized the importance of quark discovery and as a consequence they created their first ever document planning the future of nuclear physics research in 1979, The Long Range Plan for Nuclear Physics [1]. In this document, a facility that produces a continuous electron beam with at least 2 GeV of energy at a high duty factor was identified as the tool for studying these new particles in the nuclear regime [1]. The approval of construction was given to the Southeastern University Association (SURA) in the mid 1980s due to the superconducting radio frequency (SRF) based design and its ability of upgrading in the future. Once the first beam got delivered in 1994, a decade of successful research began. After 178 completed experiments on the topics of nucleon structure and form factors, electroweak interaction testing and more, the lab ceased operations in 2012 as the installation of the 12 GeV upgrade began. The research opportunities a higher energy beam would offer includes the study of confinement via the observations of exotic hybrid mesons, a new form of hadronic matter containing forbidden quantum numbers. This forbidden state is reached when the gluonic flux tube connecting the quark-antiquark pair gets excited, and the vibrational contribution of the excited flux tube produces the exotic quantum numbers of the system [2]. These exotic mesons should hypothetically be produced in 9 GeV pion photoproduction processes [2]. The higher energy also allows for measurements of elastic form factors at a larger momentum transfer. This would resolve the incompatibility of form factor measurements obtained through two different methods: the Rosenbluth separation of cross sections and recoil polarization measurements [3]. Moreover, proposed experiments would double the kinematic range of available neutron form factor data, allowing the separation of individual quark contributions to form factors to be extended to higher Q^2 [4]. Generalized parton distributions (GPDs) describe the probability of finding a parton (quark) with a specific value of an observable, such as longitudinal momentum. Moreover, the GPDs measure interferences of momentum states too, thus giving quark momentum correlations in a nucleon [5]. Additionally, the functions carry information of the transverse momenta, and by applying a Fourier transform one can acquire the position of the parton in the transverse plane along with it's longitudinal momentum [5]. JLab's detectors are an ideal tool to study GPDs, as they are acquired from deep exclusive measurements such as Deeply Virtual Compton Scattering [6].

A. Facility Overview

The CEBAF facility consists of a continuous wave recirculating linear accelerator delivering a 11 GeV electron beam to four research halls: A, B, C, and D. Two linear accelerators, North and South, accelerate the beam with superconducting radio frequency cavities. The beam gets bent around recirculation arcs that connect the two linacs. The electrons make five passes around the accelerator before the beam bunches get separated and guided into the four halls. Hall D electrons go through another pass through the North accelerator before they are directed to Hall D. The electrons are produced in the injector by illuminating polarized laser light of $\lambda = 780nm$ on a Gallium-Arsenide semiconductor, which emits bunches of electrons that are spin polarized up to $\sim 85\%$ by photoemission [7]. In the 6 Gev era, the accelerator worked on three-beam operation: three bunches were created at 499 MHz, each spaced apart by 120° of phase, forming 1497 MHz interleaved bunches [8]. A fourth laser was added for Hall D, operating at 249.5 MHz. In order to integrate the fourth laser to the interleaved system. the 499

MHz lasers were lowered to 249.5 MHz, leaving empty spots in the beam pattern for the new Hall D beam. The produced beam bunches get accelerated with a high-voltage DC electron gun to 130 keV and inserted into the pre-buncher where the beam pulse length is adjusted to be $250\mu s$ long, separated by $16.67ms(60Hz)$ [9].The beam then encounters a RF chopper cavity which deflects the beam bunches through slits at $0°, 120°$ and $240°$ with a magnetic field acting transversely to the beam line, regulating the beam current for the halls. A second chopper cavity then recombines the beam before it arrives at the buncher. Two accelerating modules, each containing 8 SRF cavities, then accelerate the beam to 123 MeV. The beam then passes through a swerving chicane shape in order to lose the low current halo surrounding the beam core, as the halo doesn't bend as much and gets absorbed by the piping [10]. Finally, the beam gets corrected for dispersion before being injected into the accelerator. The electron beam gets accelerated by two linear accelerators (linacs), North and South, each containing 25 cryomodules. Each cryomodule consists of 8 SRF cavities operating at 1497 MHz. Three cryogenic plants cool liquid helium and deliver it to necessary equipment, including the SRF niobium cavities. The two linear accelerators accelerate the beam with an oscillating electric field tuned at 1497 MHz to match the frequency of the incoming beam bunches. As seen in *Figure 3*, the cavity length is exactly half the wavelength of the beam wave ($\lambda = \frac{c}{1497MHz} \approx 20cm$) to match the oscillating electric field with the beam pulses. Mainly, the beam bunch reaches the end of the cavity in exactly half the beam pulse period as it' accelerated by the electric field ($T = \frac{1}{1497*10^6 MHz}$). As it enters the second cavity where the field is of opposite sign, the field switches off, allowing the electron to pass unperturbed to the next cavity, where the field is switched on and the electron is accelerated once again. The voltage that needs to be applied to the cavities can be obtained from the assumption that the electric field must have no component perpendicular to the direction of motion. The frequency and wavelength of the oscillating field are known as they match the beam bunches, so one can solve the wave equation for the component of the electric field along the beam axis [11]. From there, the applied voltage is obtained by integrating the field along the axis of travel [11]. The beam gains 1.1 GeV of energy per pass of one linac. As it gets accelerated, the beam gets displaced in the transverse direction, and the bunches get stretched along the beam axis. In order to correct for this, quadrupole focusing magnets are placed along the beam between the cryomodules to negate these effects. Quadrupoles work as a lens, the field strength increases linearly as the distance from the optical axis increases [13]. As a consequence, they have the ability to focus in one direction, whilst defocusing in the other direction. In order to achieve focusing in all directions, quadrupole magnets are arranged in a FODO lattice, where focusing and defocusing quadrupoles are alternated [13]. As the beam exits the linac, it encounters the spreader and the recirculation arcs. The spreader consists of deflecting dipole magnets with quadrupoles in step as vertical dispersion suppressors [9]. The spreader magnetic field bends each beam according to the momentum (eg. lowest momentum beam in the first pass gets bent into the uppermost arc). At the end of the arcs a recombiner mirror-symmetric to the spreader recombines the beam bunches. The uppermost arcs on each side have 16 dipole magnets of the "double pancake" design to guide the beam around the 250 m bend, whilst the other arcs have 32. As the beam gets bent by the dipole magnets, effects of synchrotron radiation and optical aberrations influence the beam quality. Synchrotron radiation is an effect that occurs when a charged particle experiences an acceleration perpendicular to its velocity. The expression for the power radiated by synchrotron radiation can be obtained using Lienard-Wiechert potentials. The energy crossing a surface enclosing a charged particle is given by integrating the Poynting vector: $E = \int_{-\infty}^{\infty} \boldsymbol{S} \cdot \boldsymbol{n} dt$, where n points from the particle's retarded position to the point where the fields are evaluated [14]. An expression for power per solid angle is obtained within the integral if one multiplies by $\frac{dt'}{dt'}$ and R^2:

$$\frac{dP(t')}{d\Omega} = (1 - \boldsymbol{\beta} \cdot \boldsymbol{n}) R^2 \boldsymbol{S} \cdot \boldsymbol{n} \tag{1}$$

The Poynting vector is obtained from the Lienard-Wieckert vector potential:

$$A^{\mu} = [\frac{e\beta^{\mu}}{R(1 - \boldsymbol{\beta} \cdot \boldsymbol{n})}] \tag{2}$$

, where R is the absolute distance between the current and retarded position. The radiation is transverse, so one can write: $\boldsymbol{n} \cdot \boldsymbol{E} = 0; \boldsymbol{n} \cdot \boldsymbol{B} = 0$. The Poynting vector is then: $\boldsymbol{S} = \frac{e^2}{c4\pi R^2}[\boldsymbol{n}|\boldsymbol{n} \times (\boldsymbol{n} \times \dot{\boldsymbol{\beta}})|^2]$. This expression is inserted into equation (5) and the power is integrated over the solid angle. This gives the following expression: $P = \frac{2e^2\gamma^6}{3c}[\dot{\beta}^2 - (\beta \times \dot{\beta})^2]$. When a particle is experiencing a radial acceleration, we have: $\dot{\beta} = \frac{c\beta^2}{R}$, R being the radius of the circle of motion. This leads to the power being:

$$P = \frac{2e^2 c \beta^4 \gamma^4}{3R^2} \tag{3}$$

[14]. In order to negate the effects of radiation, 32 quadrupole girders are placed on each arc to address issues caused by the bending: betatron oscillations around the equilibrium position, achromaticity control, and momentum compaction. Beam Position Monitors are placed at each of the quadrupoles to perform checks on the beam quality. After the beam gets recombined, it enters the South linac to get accelerated, and the whole process gets repeated for five laps. If one of the halls A-C requires a lower energy beam, a spreader working at a frequency of 500 MHz separates the beam bunches destined for the

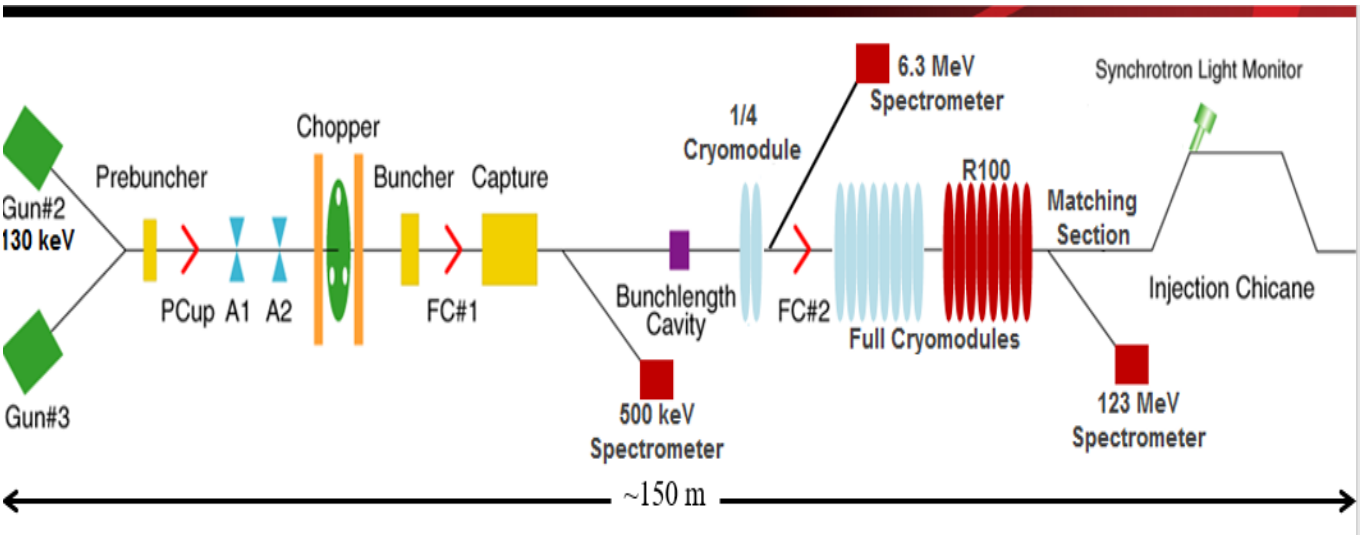

FIG. 1. A visual representation of the injector system and all of it's components. Picture adopted from [9].

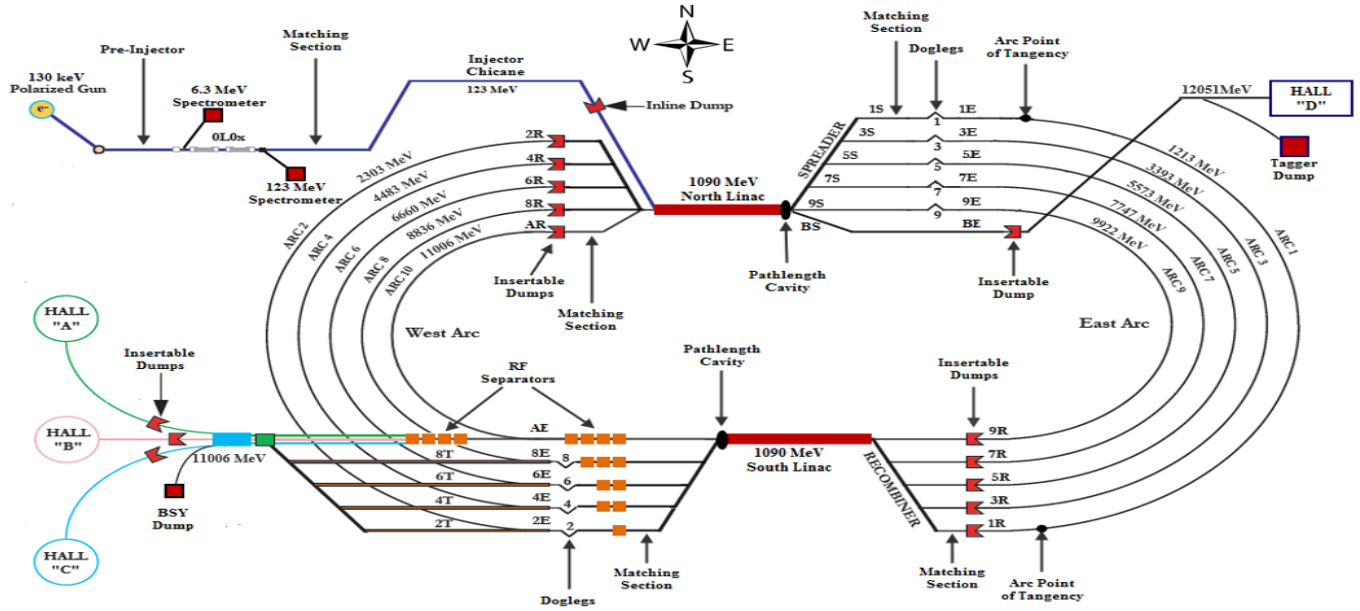

FIG. 2. A visual representation of the injector, the accelerator, and the research halls at Jefferson Lab. Picture adopted from [9]

hall requiring lower energy. If all halls require maximum energy, at the fifth pass a 750 MHz separator separates the beam destined for Hall D from the rest of the beams and directs it for a final pass through the North linac. The interleaved beam destined for halls A-C enters the extraction region where it encounters a second 500 MHz separator that splits the beam bunches according to their destination.

B. The CLAS12 Detector at Hall B

Hall B at Jefferson Lab uses the CLAS12 spectrometer for data acquisition. CLAS12 is a large acceptance spectrometer built around two superconducting magnets: a torus and solenoid. The solenoid is placed at the center and deflects particles with low recoil momentum that scatter at an $40^\circ < \theta < 135^\circ$ in polar angle, while the torus magnet deflects particles with high recoil momentum, in the range of $5^\circ < \theta < 40^\circ$. Two detector arrays are built around the two magnets, the Central Detector and The Forward Detector, the former measuring kinematic properties of the low momentum particles, while

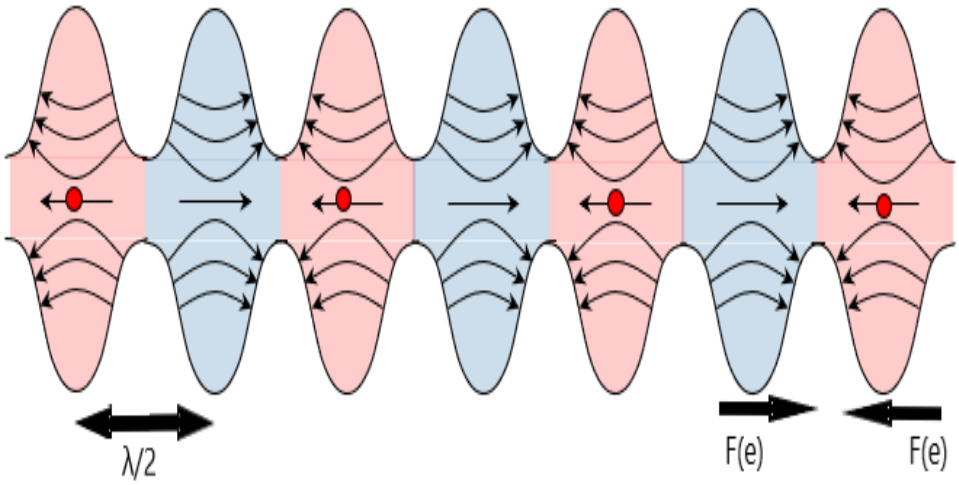

FIG. 3. An image of the RF cavities and their principle of operation. Red cavities represent areas where electrons get accelerated, whilst the red cavities decelerate electrons. Picture is adopted from [12] and edited.

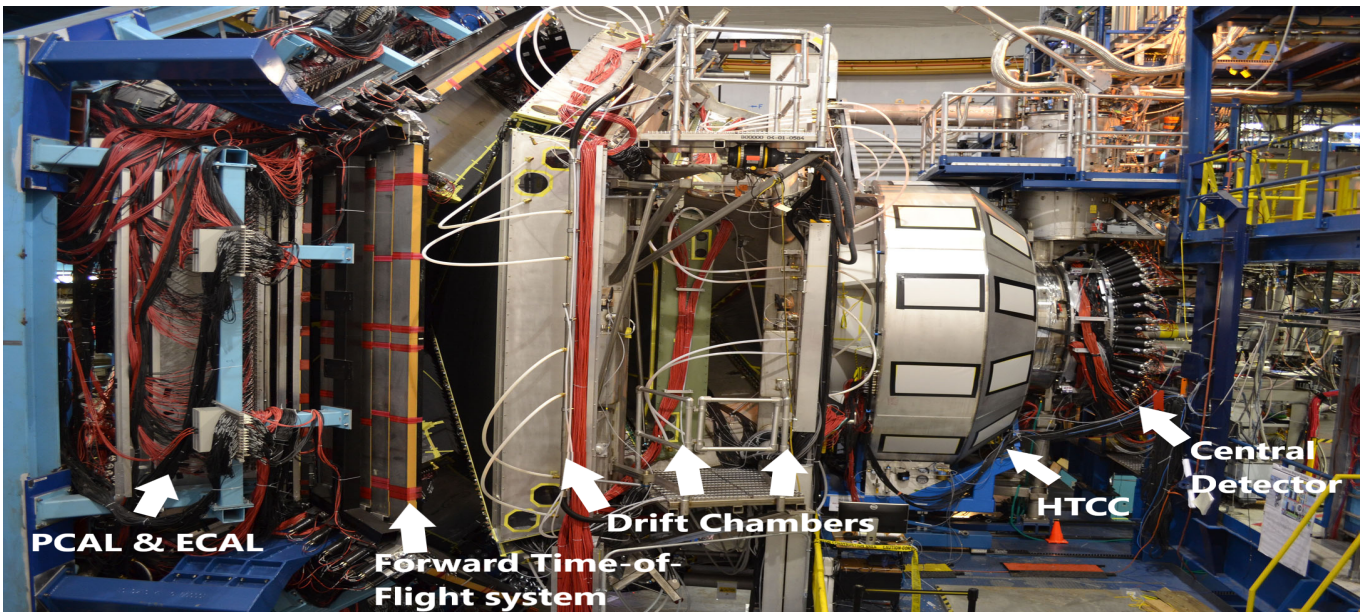

FIG. 4. The entire CLAS12 detector. The beam is incident from the right onto the target, located within the central detector and solenoid magnet. Picture adopted from [6] and edited.

the former observes particles in the forward region of the detector. The torus consists of six superconducting coils, with each coil being made from a two-coil "double pancake" in an aluminum case. The coils are arranged symmetrically to approximate a toroidal field around the beam axis. The coils divide the active detection area of the Forward Detector into six sectors. The torus operates at a nominal current of $3770A$ and a peak field of $3.58T$ [6]. The solenoid has multiple uses: firstly, it deflects the low momentum recoil particles. Secondly, it acts as a shield deflecting the electrons produced by Moller scattering. Finally, it provides a highly uniform field at it's center, therefore allowing researchers to use dynamically polarized targets, with the targets being $< 90\%$ polarized. The solenoid operates at a nominal current of $2416A$, providing a $5T$ field at it's center [6].

1. *Components of the Forward Detector*

As mentioned before, the detection area of the Forward Detector is divided into six sectors, with the detectors having symmetrical components in each. As a particle gets scattered off the target, the first detector it

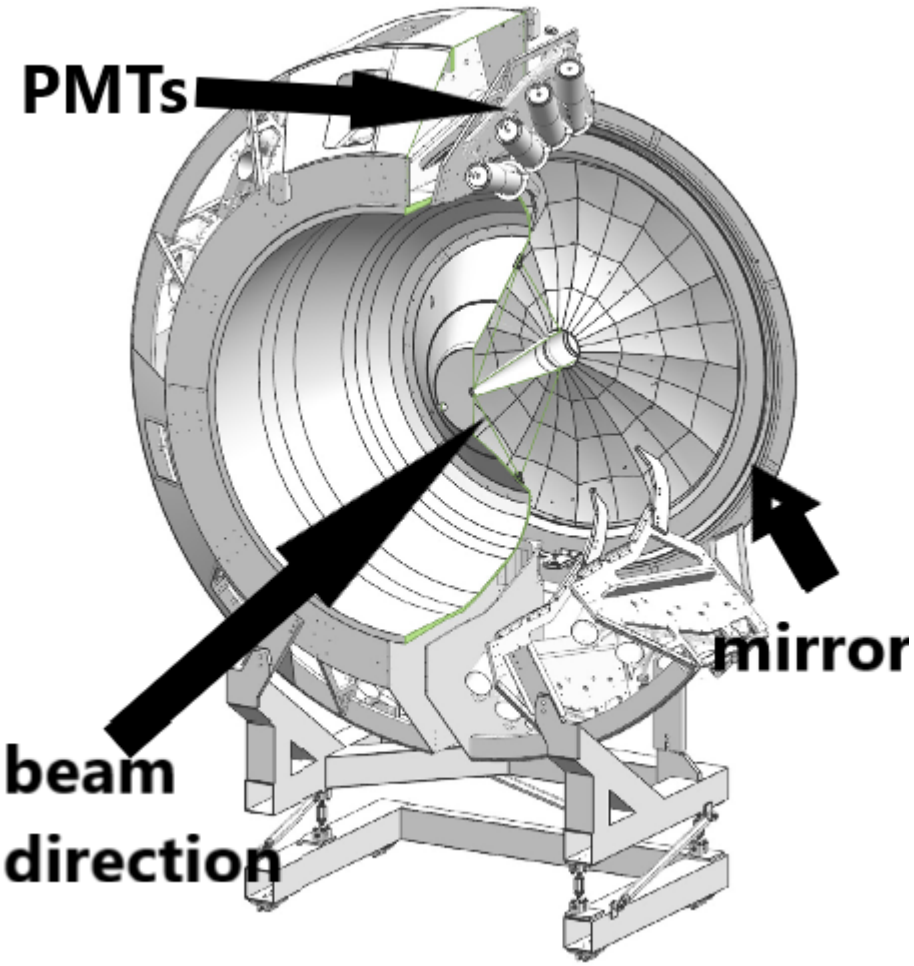

FIG. 5. The High Threshold Cherenkov (HTCC) detector. The incident beam direction is shown. The particle emits Cherenkov light at forward angles onto the mirrors, which deflect the light onto the PMTs, placed at the outer edges of the platform upholding the detector. Picture adopted from [6] and edited.

encounters in the forward region is the High Threshold Cherenkov Counter (HTCC). This detector provides the separation of electrons from pions and kaons. The detector has the ability to distinguish between them above 4.9 GeV/c [6]. It consists of a single unit, using dry CO_2 at $1atm$ as the active medium. A second, Low Threshold Cherenkov Counter (LTCC) is positioned further upstream, the particle encounters it as it exits the torus field and the time-of-flight scintillators. The LTCC has the abiility to discriminate between pions and kaons in the momentum range of $3.5 - 9GeV/c$. The different threshold was achieved by using a different active medium, the LTCC uses C_4F_10 as the radiator gas. The threshold energy of a Cherenkov counter is defined as: $E_{th} = m_0c^2(-1 + \sqrt{1 + \frac{1}{n^2-1}})$, where n is the index of refraction of the medium [15]. When an electron enters the active medium, it's moving at a velocity higher than the velocity of light in the medium ($\nu_{light} = \frac{c}{n}$), and it therefore emits Cherenkov radiation. The photons are emitted preferentially in the direction of motion of the particle, which results in the photons forming a cone of light around the traveling electron. The angle of the light cone is: $cos(\theta) = \frac{1}{\beta n}$ [15]. Therefore, by measuring the cone angle of Cherenkov photons gives β. If one measures the particle momentum, the mass of the particle can be calculated. The emitted Cherenkov light is reflected by a multi-focal mirror consisting of 48 elliptical mirror facets that focus the Cherenkov light onto 48 photomultiplier tubes (PMTs) that convert the emitted light into an electrical signal [6]. The mirror facets have one focus at the interaction point, and the other focus on the PMTs. This allows the light to efficiently be focused and directed onto the PMTs. Winston cones, parabolic light reflectors, are installed in front of the PMTs to increase the light collection efficiency. As the light gets reflected on the PMT, it strikes the photocathode, where electrons are produced via the photoelectric effect. They are then accelerated through a series of dynodes by an applied electric field. Since the dynodes have a high secondary emission coef-

ficient, additional electrons are produced at the dynodes and accelerated along with the shower [15]. The amplified pulse is then collected at the anode. The split signals of all flash ADCs are reconstructed to give the real signal strength. The process of reconstruction proceeds by converting the ADC signal into a number of photoelectrons with a calibration constant saved in Jefferson Lab's Calibration Constants Database (CCDB). The signal with the largest number of photoelectrons is then identified and used as a seed, a starting point, for building a cluster of all the hits. Timing and location of the signal, measured in angular coordinates, is also recorded and is used in creating clusters. Hits adjacent to the seed hit are added to the cluster if the response happened within a certain time window. The signal strength is determined as the sum of the individual signals within the cluster, while the signal time is obtained as a weighted average of the individual signal times, weighted by the number of photoelectrons in a hit [16]. The angular coordinates of the hit are obtained by computing an average angular coordinate of all the hits, and the angles are then projected on the ellipsoidal mirror surface to obtain the cluster coordinates. As they exit the HTCC, the particles traveling through CLAS12 enter the torus field and the drift chambers. There are 3 separate drift chambers for each detection sector. Each drift chamber has 2 superlayers, each consisting of 6 layers of wires, with the wire layers of the two superlayers being strung at a $\pm 6^{\circ}$ angle with respect to the sector midplane, allowing for better resolution of polar angles. The wire layers consist of 112 sense (S) wires, additional field (F) wires placed in-between, and guard (G) wires placed at the edges (GFFSFFSFF.....SFFG pattern) [17]. The active medium consists of a mixture of 90% Ar and 10% CO_2 [17]. A charged particle travelling through the active medium leaves behind it a trail of ionized electrons. These electrons drift towards the sense wires, colliding with gas molecules along the way, reaching the wires in time τ: $\frac{1}{\tau} = N\sigma c$, where σ is the cross section of the collision, N is the number density of gas molecules and c is the randomly oriented velocity of the scattered electron. Between the collisions, the electron is accelerated towards the wire by an electric field, gaining velocity in the field direction: $F = ma = m\frac{\nu}{\tau} = qE, \nu = \frac{qE\tau}{m}$, where E is the field strength and q is the electron charge. The two equations can be combined to give the drift velocity: $\nu = \frac{qE}{mN\sigma c}$. The drift chamber track reconstruction happens in two stages, the first stage being "hit-based" reconstruction. The reconstruction software forms hit objects, detector elements with signals. The pattern recognition algorithm then identifies clusters, many adjacent objects with a signal. Four out of 6 wire layers in each superlayer must have hits corresponding to the cluster. Noise rejection algorithms reject stray hits. Planes are then constructed from the clusters, and clusters from adjacent superlayers are matched by finding the plane intersections: this line of intersection is called a cross, it's coordinates are evaluated midway between the two superlayers. The path integral of the magnetic field through the drift chambers is computed with the torus field strength and a parabolic function obtained from the crosses between the three drift chamber regions. This integral is used along with the angle at the crosses of drift chambers one and three to compute the ratio of charge to momentum: $\frac{q}{p} = \frac{\theta_3 - \theta_1}{\nu \int Bdl}$, where the angles are in radians and ν is the speed of light, given in $GeV/cT^{-}1cm^{-}1$ [16]. The track fitting proceeds by using a Kalman Filter method with 5 parameters as input: x, y, tx, ty and Q, where $tx = \frac{p_x}{p_z}, ty = \frac{p_y}{p_z}, Q = \frac{q}{p}$ [16]. The equations of motion of the particle in the torus field are then expressed as derivatives with respect to z, as the parameters are computed at each layer with a hit, and each layer is at a fixed z distance in the local frame of analysis. The equations of motion are solved numerically by the swimmer software package using fourth-order Runge-Kutta integration to integrate from the initial measurement site to the next, giving the drift distance to each wire [16]. Once a full trajectory through the drift chambers is acquired, the track parameters are then converted to the lab frame, and the particle is "swum" to the interaction vertex, the distance of closest approach to the target, where the state vector is computed. The process of swimming refers to solving the equations of motion of a charged particle in a magnetic field. The swimming is repeated, this time from the interaction vertex, to compute the state vectors at the surface of each of the remaining subsystems. This information is used to match the tracks from the DCs to the clusters in the other subsystems. The fit is redone with time-based information to achieve greater accuracy once the information from other detectors is gathered. The arrival of the ionized electron on the wire is measured with Time-to-Digital Converters (TDCs) with a resolution of $\partial t < 1ns$. The drift time is calculated with the following formula: $t_{drift} = t_{TDC} - t_{start} - t_{delay} - t_{flight} - t_{prop} - \tau$, where t_{start} is the event start time given by the Forward Time-of-Flight system; t_{delay} is the intrinsic time delay of the wire; t_{flight} is the flight time from the interaction vertex to the wire cell; t_{prop} is the time it takes for the signal to propagate along the wire; finally, τ is the random walk time described above. The corrected time is then converted into a distance of closest approach. Mainly, the drift time is parametrized as a function of distance to the wire cell as a fourth order polynomial function. This polynomial is defined by three constraints: a maximum drift time, as all particles incident at the outer edges follow the field lines to the sense wire. Secondly, the velocity near the wire is the saturated drift velocity, V_0, found with the formula mentioned above. Finally, the polynomial has a point of inflection where the electric field is at a minimum, at $d = \frac{x}{d_{max}} = 0.64$. Using this polynomial, along with the local angle and magnetic field value at the point, the drift distance at each cell is computed and used with the corrected time in the time based reconstruction [16]. The time based reconstruction can achieve a spatial resolution of $\delta r \approx 250\mu m$, and

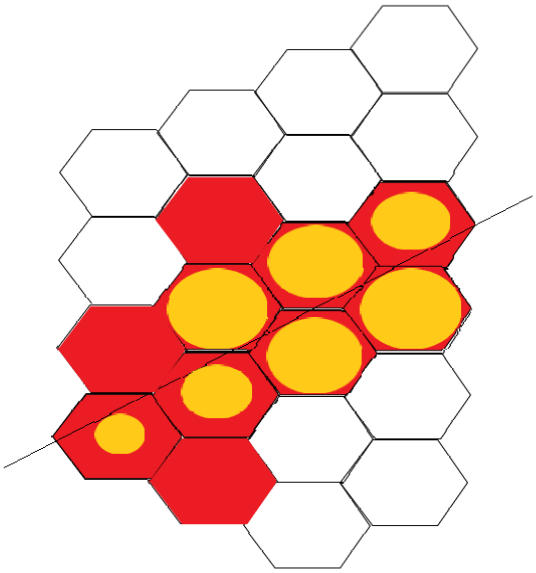

FIG. 6. A visual representation of a layer of sense wires in the drift chambers. The reconstructed particle track is represented by the line in the image. The red hexagons represent the wire cells with an electrical signal, and the yellow circles show the estimate of the distance of closest approach computed in time-based tracking.

a momentum resolution of $\frac{\delta p}{p} < 1\%$ [17]. The Forward Time-of-Flight system(FTOF) gives an accurate measure of the time of passage of charged particles through the CLAS12 detector and helps identify particle species. In order to provide reliable particle identification, a time resolution of $\sigma_t = 80ps$ is required for forward angles, while a resolution of $\sigma_t = 150ps$ is required at wide angles [18]. To accommodate these requirements, the FTOF system was constructed from three arrays of panels: 1a, 1b and panel 2. Each panel contains a number of rectangular scintillators (23, 62 and 5 for panels 1a, 1b and 2) with a PMT on each end. The scintillators are plastic and are connected to the PMTs with light guides. As a charged particle travels through the scintillator, it exchanges a virtual photon with an atom of the scintillation material, causing the atom to transition to a higher energy state. These atoms then de-excite by emitting photons which are then guided by the light guides onto the PMTs where the photoelectrons are multiplied. What's measured is the ADC charge and hit time, and the TDC time. The absorption of the virtual photon by an atom of the scintillation material can cause the excited atom to re-emit the photon in two ways: firstly, the atom can re-emit the photon immediately upon absorption, a process called fluorescence. Alternatively, the atom can be excited to a triplet state, causing a delayed emission in a process known as phosphorescence [19]. Since the CLAS12 scintillators are plastic, delayed emission is minimal and can be ignored [19]. The measure of photon absorption within a scintillator is given by the attenuation length, which is a distance over which the probability of a photon being absorbed is $\frac{1}{e}$ [18]. The number of photoelectrons produced at the PMT photocathcode is given by the formula: $N_{pe} = N^0_{pe} exp(\frac{L_0}{2\lambda_0} - \frac{L}{2\lambda})F$, where N is the number of photoelectrons at the PMT connected to a specific paddle, L and λ represent the paddle length and attenuation length, while L_0 and λ_0 are the length and attenuation length of the shortest paddle of panel 1-a, and N^0_{pe} is the average number of photoelectrons incident on the PMT for the shortest paddle. F is a scaling factor used when calculating N_{pe} for PMTs connected to paddles in panel 2 [20]. The specifications mentioned above can be converted to give a momentum threshold of species separation. The differences in flight time against momenta of different particle species with the same momenta are shown in *Figure 7*. The threshold for species separation is given as 4σ, σ being the timing resolution. The momentum at which the curve of differences in flight time crosses this threshold is the momentum threshold for species separation. The process of hit reconstruction in the FTOFs starts with matching the flash ADC and TDC information measured on each PMT. Mainly, flash ADCs measure the arriving charge in quick successive pulses. The time is obtained by fitting the leading edge of the pulse shape, corresponding to 3 to 4 measured samples, giving a resolution of $\approx 1ns$ for the FADC [16]. The TDC and ADC times have to be within a $10ns$ window for the data to be kept. The signal time at each end of the paddle can be obtained from the measured TDC times by subtracting the TDC channel-to-time conversion factor, time-walk corrections and constants that align the counter hit time with the beam oscillations [16]. If one subtracts from the PMT arrival time the light travel time, obtained by knowing the effective speed of light in the paddle from calibrations, the hit time is obtained. The

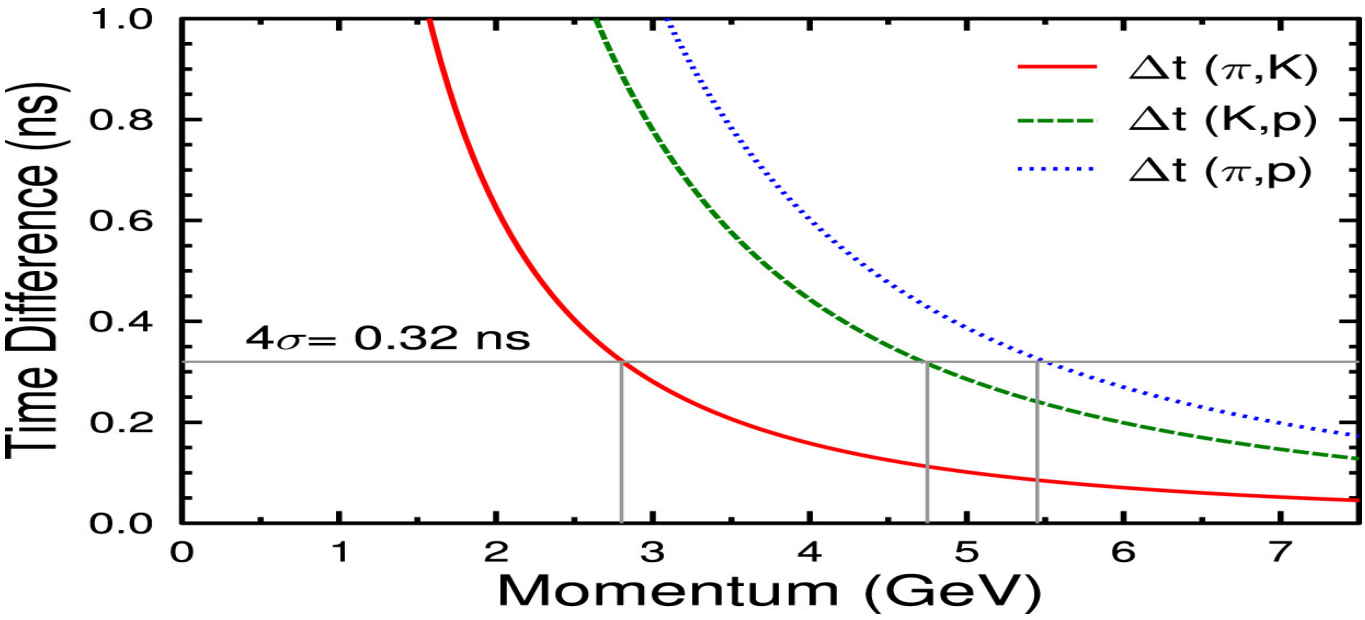

FIG. 7. The differences in flight time are shown for different particle species against the particle momentum. The horizontal 4σ line signifies the timing resolution below which the FTOF cannot measure the flight time differences reliably. The momentum at which the curves of flight time differences cross this timing threshold gives a measure of maximum momentum above which the FTOF cannot distinguish between species. Picture adopted from [18]

average hit time is obtained as the arithmetic average of the two hit times at each end. The hit coordinate can be obtained using the hit times: $y = \frac{\nu_{eff}}{2}(t_1 - t_2 - C_{12})$, where C_{12} is a calibration constant [18]. This coordinate is used to match the FTOF hits to a track. By computing the ADC signal integral and knowing the detector properties, the energy loss of a particle interacting with the scintillation volume can be obtained. The mean energy is obtained from the two energies measured at each end of the paddle as the geometric mean [16]. If both panel 1-a and panel 1-b have hits for a specific track, the timing information can be combined to give an improved measure of the resolution, an increase of 15-20% in accuracy is seen when both panels are used [16]. The electromagnetic calorimeters are the final subsystem that a particle traveling through CLAS12 encounters. This detector fully absorbs particles while recording the deposited energy and location of the energy loss. A pre-shower calorimeter (PCAL) was added in front of the electromagnetic calorimeter (ECAL) for the 12 GeV upgrade to ensure absorption. The calorimeters are of the sampling type, with interchanging layers of lead and scintillator strips. Both use a triangular hodoscope layout to account for the hexagonal geometry of the torus. The layers of scintillator strips are arranged to alternate between three readout planes, so called views: U, V, and W, with the strips in each of the planes being parallel to one of the sides of the triangle, as seen in *Figure 8*. Each of the 6 symmetrical modules of the PCAL contain 15 active layers, 5 of each readout plane, same as the inner calorimeter, while the outer calorimeter has 24 active layers, corresponding to 8 layers of each readout plane. The PCAL is more fragmented, as one active layer is comprised of 84 strips in the U layer, and 77 strips in V and W layers, while the ECAL has 36 strips per layer [22]. The light created by the scintillator strips must be measured in sum, so all the strips in one view are coupled. In the inner ECAL, the light emitted at the first strip in the first layer of the U view is measured together along with the light emitted at the first strip of the second, third, fourth and fifth layer of the U view. Therefore, the layers are grouped together into stacks. The stacks are grouped by the calorimeter components, PCAL and inner ECAL stacks have 5 strips, and outer ECAL stacks have 8 strips. The ECAL uses optic fibers that are bundled together, with one bundle guiding the light from all the strips in a stack to a PMT [21]. The PCAL has wavelength-shifting (WLS) fibers inserted inside holes running the length of the scintillator strip that down-convert the emitted photons and guide them to the PMTs [22] The main source of energy loss of an electron traversing through the medium is Bremsstrahlung radiation. On the other hand, a photon loses energy through pair production, characterized by the photon energy and the energy levels of the medium, Compton scattering, Rayleigh scattering and absorption, characterized by interaction cross sections. The medium can be characterized by a radiation length, the length over which a particle is left with $\frac{1}{e}$ of energy:

$$E = E_0 e^{\frac{-x}{X_0}} \tag{4}$$

,where E_0 denotes the initial particle energy. From there, we see that the rate of energy loss as a function of space, $\frac{dE}{dx}$, is proportional to $\frac{E}{X_0}$. In the limit of $x \ll X_0$, the en-

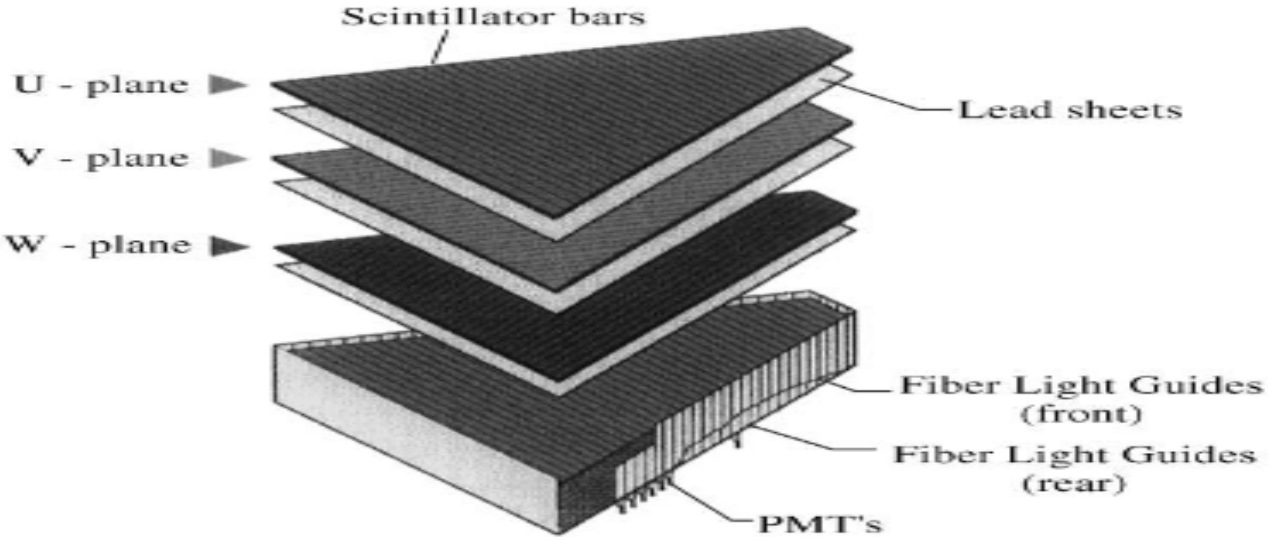

FIG. 8. The layers of the electromagnetic calorimeter. The three readout planes are shown, along with the absorbing layer of lead and the light guides that guide the shower to the PMTs at the back. Picture adopted from [21].

ergy loss is given by $\frac{E_)}{X_0}$ [23]. The cascade will stop at the critical energy, E_c. For a photon traveling through the medium, the mean free path between pair productions can be obtained from the cross section of the reaction: $\lambda = \frac{9}{7}X_0$ [19]. The intensity of the photon beam drops off exponentially with distance: $I = I_0 e^{\frac{-7x}{9X_0}}$. As all of these properties are related to the mass and atomic number of the medium, a heavy element such as lead is used in the absorption layers. Particles that produce a signal trigger the cluster finding algorithm. This algorithm finds collections of stacks with energy above the defined threshold. All the stacks of one view form a peak, and each stack is referred to as a hit. Each hit has its geometry stored, and the algorithm discriminates based upon the positions of hits to identify a cluster. The algorithm imposes a criterion of requiring a spatial intersection of three peaks, one for each view. Since the peak is comprised of many hits, stacks of strips in different layers, a line segment going through all the stacks in a peak can be constructed. The line is constructed as a energy-weighted average of the mid-lines of each member strip within a stack [22]. The process of localizing a cluster is shown in *Figure 9*. The path length from the now known cluster position to the PMT for each of the three peaks is then calculated in order to correct for scintillator light attenuation: $L = L_0 e^{\frac{-x}{l}}$, where x denotes the path traveled, l is the attenuation length of the scintillator, and L_0 is the initial intensity [19]. The energy is then obtained by knowing the effective velocity of light. Additionally, peak timing is also corrected for by using this velocity and the computed path length. The cluster energy is then computed as the sum of each of the three corrected peak energies. Also worth mentioning is the Forward Tagger, a separate detector system that extends electron detection capabilities to smaller polar angles, in the range of $2.5° < \theta < 4.5°$. The system consists of a micro strip gas tracker that measures the scattering angle, a scintillator hodoscope that provides photon and electron separation, and an electromagnetic calorimeter consisting of lead-tungsten crystals that measures the deposited shower energy [6].

2. The Central Detector

The Central Detector is built around the target and the solenoid magnet, seen in *Figure 10*. It consists of the Central Vertex Tracker (CVT), the Central Time-of-Flight System (CTOF), and two neutron detectors: the Central Neutron Detector (CND), and the Back Angle Neutron Detector (BAND), which extends the ability to detect neutrons to polar angles $155° < \theta < 175°$, with a neutron detection efficiency of 30% and a momentum resolution of 1.5%. Track reconstruction in the Central Detector begins with the Central Vertex Tracker. The CVT consists of 12 active detection layers, separated into two subsystems. The first 6 layers are the Silicon Vertex Tracker. The SVT uses silicon strip technology, which provides a tracking efficiency of $\geq 90\%$, a transverse momentum resolution of $\frac{\delta p_t}{p_t} = 5\%$, and angular resolutions of $\delta\theta \leq 10-20 mrad$ for $35° < \theta < 125°$, and $\delta\phi \leq 5 mrad$ [24]. The detector is built from 3 concentric, double layered rings, with each of the regions containing 10, 14, and 18 double sided modules of silicon strip sensors at 65, 93, and 120 mm [24]. The outer 6 layers of the CVT are the Barrel Micromegas Tracker (BMT). The detector contains 6 cylindrical active detection layers, with 3 layers

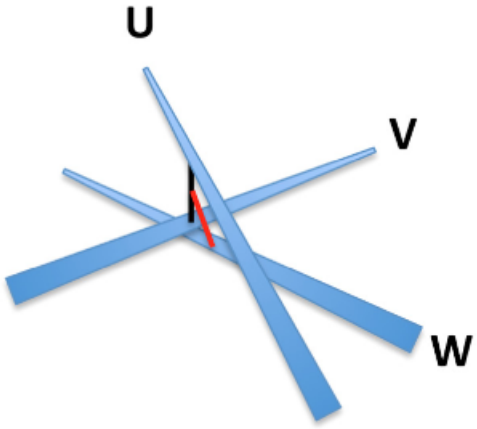

FIG. 9. The process of defining the spatial coordinates of a cluster in the calorimeters. The three lines represent the line segments constructed from the three peaks, U, V and W. The black line is constructed to connect segments U and V, and the red line is then drawn from the midpoint of the black line to the W strip. The cluster transverse coordinates are then defined as the coordinates of the midpoint of the red line. The longitudinal coordinate is taken at the layer of maximum energy deposition to avoid parallax errors for particles with trajectories that are not normal to the layers of the detectors [22]. Picture adopted from [22].

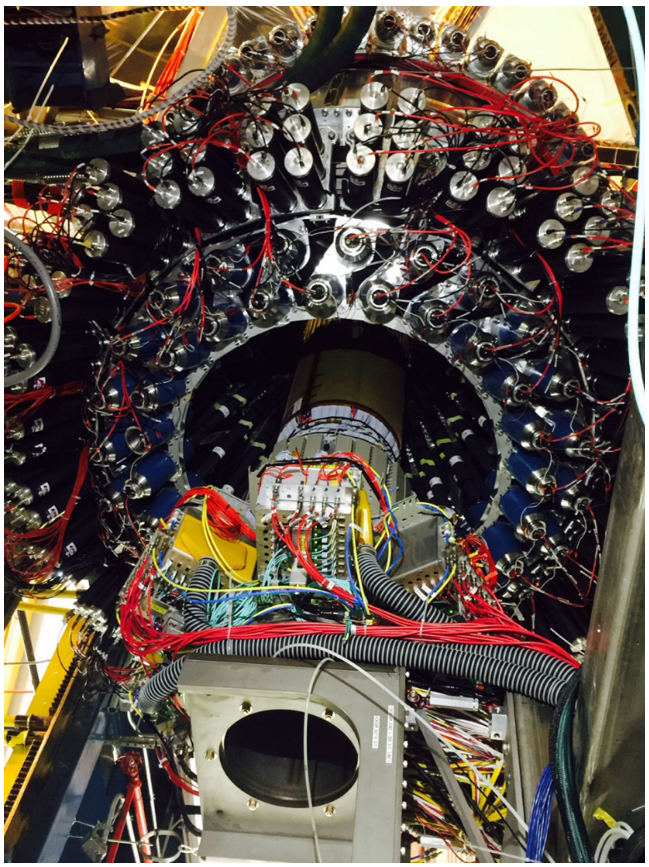

FIG. 10. The CLAS12 Central Detector. The central tracking system is retracted from its position for a better view. Around it are the two rings of PMTs and light guides of the Central-Time-of-Flight System, while the three outermost rings of PMTs are from the Central Neutron Detector. Picture adopted from [6].

having strips going along the beam axis (Z strips), and three with circular strips (C strips) that are perpendicular to the beam axis. Each layer consists of micro strips that read out signals, and electrode plates that provide a drift voltage of $5 - 6kV/cm$ [25]. At this voltage, the 5 T solenoid field causes the primary drift electrons to move at an angle of 40° with respect to the electric field direction [25]. As a result, a mixture of 90% Argon and 10% isobutane is used as the ionization gas due to its limited drift velocity. An additional detector, the Forward Micromegas Tracker (FMT), is placed downstream of the target center. This detector consists of 6 identical discs with an active area of 1024 strips. The drift field and magnetic field are parallel in the FMT so there is no effect of the Lorentz force. A higher drift velocity gas mixture of 80% Argon, 10% isobutane and 10% of carbon tetrafluoride is used as the ionization gas [25]. The track reconstruction begins similarly to forward tracking, clusters are sought for first. The solenoid causes particles to move in a helical fashion. This causes projections in the x-y plane to be circles and projections in the r-z plane to be straight lines [16]. The pattern recognition algorithm searches for circular hit patterns in the x-y plane of the SVT hits and BMT Z strips. The pattern recognition algorithm then connects two adjacent x-y clusters into a cell unit if the angular distance between them is below a certain threshold [16]. The pattern recognition in the r-z plane uses information from BMT C strips exclusively, and a straight line fit is applied to the clusters, with the SVT hits used as rejection criteria [16]. Once a track candidate is obtained, it gets passed to a Kalman Filter. The helical motion is described by 5 parameters, obtained from the applied fits in the x-y and r-z plane [16]. The state vector is then propagated to the outermost layer of the CVT and brought back to the CVT revolution axis as it is and the propagation occurs again, with a maximum of five iterations [16]. The Central Neutron Detector (CND) detects neutrons with $0.2 - 1GeV/c$ of momenta. It consists of 3 layers of 48 scintillator paddles coupled at their downstream end with light guides, and connected to PMTs with light guides at the upstream end. The light can go through the light guide at the upstream end and to the PMT, called a direct hit, or through the downstream light guide into a neighboring paddle, classified as an indirect hit. The reconstruction starts with the separation of the direct and indirect hits by comparing PMT times [16]. Next, the deposited energy of the hits needs to be reconstructed using a formula that includes the ADC-to-energy constant, the distance from the paddle to the PMTs and the coupled paddle pair properties [16]. Finally, by calculating the propagation times to the two PMTs the time of flight is obtained, which is used in species identification along with the hit position [16]. The Central Time-of-Flight (CTOF) detector is a hermetic barrel of 48 scintillation counters at 25 cm from the beam axis [**?**]. Each counter has light guides on each end that guide the light onto PMTs. The time resolution of the detector equals that of the FTOF, $\sigma_t = 80ps$. The reconstruction process of the raw hits is the same as for the FTOF, with the exception that the FTOF uses a leading-edge discriminator for the FADC signal, while the CTOF uses a constant fraction discriminator which takes into account the entire pulse [16]. The Event Builder is the last service that's employed in reconstruction. The Event Builder matches hits from different detectors by looking at geometric coincidences of the signals using criteria defined by the resolutions of the subsystems. It then calculates the event start time using timing information from the time-of-flight systems, the path length to the FTOF, and the speed of the particle. The calorimeter signal then identifies electrons and positrons by comparing to expected responses. This information is checked with the HTCC to see if the angle of the Cherenkov cone gives $\beta \approx 1$. Other charged particles are identified by computing the time residuals: the flight time of a particle with a particular mass is computed ($p/K/\pi$), and the smallest time difference compared to the measured time gives the particle species. For neutral particles, they are assumed to be neutrons or photons, and the clusters in the ECAL and CND are used to construct the path and compute the value of β: if its close to 1 the particle is a photon, and a neutron otherwise.

3. Hall Software & Ongoing Software Development

All the services that reconstruct raw detector hits as described above are contained within the hall's reconstruction framework, CLARA. CLARA is based on a service oriented architecture, where many loosely coupled, self-contained services perform the necessary tasks to reconstruct the raw event data. It consists of four layers, the first one being a publish-subscribe messaging system, providing a standardized protocol of communication between the many services written in different coding languages [26]. The next layer is the service layer, which houses all the services used to build physics data processing applications. The orchestration layer contains an application controller agent that controls the physics data analysis and ensures service functionality. Finally, a physics complex event processing layer contains agents that oversee and analyze the reconstructed event data in real time, with the ability to act on any changing conditions or abnormalities [26]. Other tools within COATJAVA include the geometry package, an interface that describes all the complex detector components with geometrical objects: for example, detector layers are planes, while hexagonal wire chambers are represented as hexagons [16]. The Calibration Constants Database (CCDB) is a package that contains all the calibration constants of the detectors and their geometry, and maps of the entire CLAS12 spectrometer that are used in reconstruction [16]. The aforementioned swimmer package "swims" particles in a magnetic field: it solves the equations of motion of the particle using an adaptive step fourth order Runge-Kutta integration with

fifth order corrections. The adaptive step algorithm increases the step size in an area of a weak field and decreases it in areas of peak field. The single step advancement is achieved with a configurable Butcher tableau advancer, a matrix containing the coefficients for evaluating the function between the two steps [16] [27]. The swimmer package utilizes the magnetic field package to obtain the field values at points in space. The magnetic field package creates binary field maps from engineering models of the torus and solenoid. It also has the ability to cache the nearest neighbour values of a point that's currently being loaded in the swimmer, creating a probe that increases the speed of swimming. Analysis and plotting is done with GROOT, a histogram plotting software with a programming interface modeled after CERN's ROOT software. The final COATJAVA package is the simulation package, Geant4 Monte Carlo software (GEMC). GEMC is a C++ framework that utilizes Geant4, CERN's toolkit for passage of particles through matter. The initial conditions of the scattered beam are defined in a text file by the user: the number of events, the range of angles at which the particles scattered from the target, the range of momenta of the scattered particles, and the detectors to use. The software uses a Monte Carlo routine to randomize the directions and momenta of the scattered particles. It then accesses simulation parameters that are stored in external databases to create Geant4 objects in real time. These parameters include: the geometry of all subsystems and mirrors, the materials and their properties, the electromagnetic fields, the calibration and digitization constants [28]. The particles are then transported through detector materials, producing radiation, primary hits and secondaries, and the software collects all the raw output produced by the detectors in a single file. The analysis presented below is done on simulated events created by GEMC. For the purpose of this research, 10 000 events were produced with GEMC in sector 1 of the active detection area: uniformly spread through $-30^\circ < \phi < 30^\circ$, with electrons having $6GeV/c$ of momenta, and scattering at forward angles, $5^\circ < \theta < 35^\circ$. The raw event data was then reconstructed with CLARA. Two data banks of interest were extracted for each event: one bank contains the state vector of the beam at the vertex, positions and components of momenta, stored by GEMC before it proceeded to simulate the trajectory through CLAS12. The other bank of interest contains the same information, the vertex state vector, but obtained from reconstruction. As mentioned before, once the track is reconstructed at the drift chambers, it gets swam to the interaction vertex where the state vector is computed and saved in our bank of interest. The two state vectors are then used as input for the swimmer package. The swimmer swims the particles with simulated vertex data and reconstructed vertex data to an endpoint, initially defined at a radial distance of $175cm$ from the origin, the target, as an approximation to stop particles once they reached the curved surface of the HTCC. The swimmer returns the state vector at the endpoint, and the difference in endpoint positions is plotted. The standard deviation of this graph gives a measure of the reconstruction spatial resolution, once a fit is applied to the graph and the standard deviation is acquired. The standard deviation of the plot of differences in $\sqrt{(x^2+y^2)}$ gives the impact parameter resolution, while the angles of direction are computed from components of momenta, with the differences in θ and ϕ giving a measure of the angular resolution. The analysis was extended to an FTOF layer, an inner ECAL layer, and each of the three regions of the drift chambers. Since all of these systems are tilted 25° with respect to the beam axis, the Tilted Sector Coordinate System (TSCS) is used for swimming, where the z axis is perpendicular to the planes of the detectors, and the detection layers are at a fixed z distance from the origin. The input data therefore needs to be transformed to the TSCS, and the output of the swimmer needs to be transformed back to the lab frame before the differences are computed, with the exception of the impact parameter as this quantity will be used in reconstruction in the local tilted frames as a measure of uncertainty when matching clusters. The magnetic field maps also undergo a rotation to the TSCS before they're used by the swimmer. An example of the results of the positional resolution and it's dependence on z distance is shown in *Figure 11*. The fitter that fits the graphs of differences in position, angles and impact parameter works as following: the initial estimates of the amplitude, σ and mean are given as input, along with the range over which to fit, the fitting function to use, and the fitting method. Gaussian functions and Neyman's chi-squared method were used to fit the data. The fitter struggled as the peaks showed asymmetric behavior. As the particles curve in the magnetic field, they emit synchrotron radiation, described in paragraph 2. This radiation causes the particle to lose transverse momentum, and as a consequence, the reconstruction software overestimates the vertex momentum as the effects of radiation loss are not taken into account. This momentum overestimation creates a positive tail in the graphs of differences in all quantities. When the angles, obtained from components of momenta, are plotted for different particle species, as in the bottom row of *Figure11*, the discrepancy in the results is greater than for the spatial resolutions, as the momenta of μ^- and π^- is not affected by the radiation as much. To clarify, as the muons and pions have a higher mass, and consequently a lower velocity for the same beam momenta, the radiation emitted will be lower, as a result of the β^4 and γ^4 dependence of the power emitted. To mitigate the effect for electrons, two fits were applied: one fits the entire data set, while the other fits the central peak exclusively. The amplitudes, means and sigmas of the two fits are then used to evaluate an effective value of σ from the combined first and second moments of the two Gaussians: $mom_1 = \frac{A_1}{A_1+A_2}\mu_1 + \frac{A_2}{A_1+A_2}\mu_2$, $mom_2 = \frac{A_1}{A_1+A_2}(\mu_1^2+\sigma_1^2) + \frac{A_2}{A_1+A_2}(\mu_2^2+\sigma_2^2)$. The effective standard deviation is given as: $\sigma_{effective} = mom_2 - mom_1^2$.

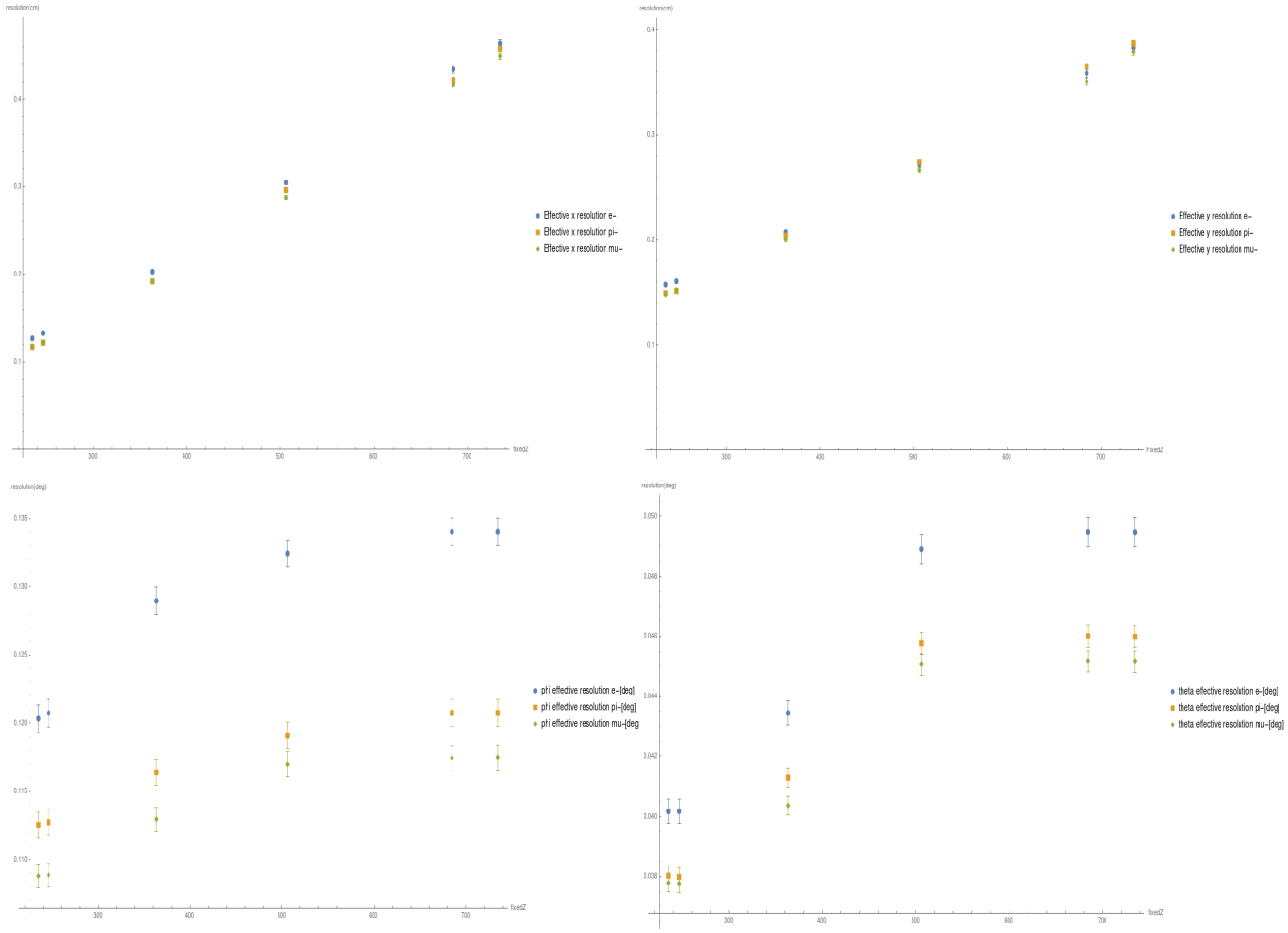

FIG. 11. The x, y, phi and theta resolution at regions 1, 2, and 3 of the drift chambers (2 points in the first region), the FTOF, and the fourth layer of the inner calorimeter against the fixed z distance in the Tilted Sector Coordinate System. The information is shown for 6 GeV electron, pion and muon beams (e^- shown in blue, μ^- in orange, π^- shown in green). The uncertainties in individual data points were obtained as: $\delta res = \frac{res}{\sqrt{2N-2}}$, where N signifies the number of events contained within the histogram.

4. *Summary*

This paper summarized the process of reconstruction in all the subsystems of CLAS12. These reconstruction routines were highlighted as the reconstruction resolutions obtained by this research project will be used in the described processes: the impact parameter resolution will give a direct constraint on finding clusters in localized frames of the subsystems. The angular and spatial resolutions will replace current approximations obtained from individual detector resolutions as constraints on matching of clusters from other subsystems to reconstructed tracks in the drift chambers. These quantities will be obtained for different particle species, and for electrons with varying kinematics.

5. *Acknowledgments*

This measurement was supervised by JLab staff scientist Dr Veronique Ziegler and Dr Gerard P. Gilfoyle, a professor at University of Richmond, who both provided valuable input in completing the analysis for this paper. This material is based upon work supported by the U.S. Department of Energy (DOE),Office of Science, Office of Nuclear Physics under contract DE-AC05-060R23177.

[1] National Science Advisory Committee, A Long Range Plan For Nuclear Science, https://science.osti.gov/-/media/np/nsac/pdf/docs/1979_Long_Range_Plan.pdf?la=en&hash=C5FC769ACD98681FA97D893A1B2F0355793684A3 (1979), [Online; accessed 22-June-2020].

[2] J. Lab, Pre-Conceptual Design Report (pCDR) for The Science and Experimental Equipment for The 12 GeV Upgrade of CEBAF (2005).

[3] C. Perdrisat, V. Punjabi, and M. Vanderhaeghen, Nucleon Electromagnetic Form Factors, Progress in Particle and Nuclear Physics **59**, 694 (2007).

[4] G. Gilfoyle, W. Brooks, and K. Hafidi (CLAS), Measurement of the Neutron Magnetic Form Factor at High Q**2 Using the Ratio Method on Deuterium, in *4th Workshop on Exclusive Reactions at High Momentum Transfer* (2011) pp. 266–274.

[5] M. Garçon, An introduction to the Generalized Parton Distributions, The European Physical Journal A **18**, 389–394 (2003).

[6] V. Burkert *et al.*, The CLAS12 Spectrometer at Jefferson Laboratory, Nucl. Instrum. Meth. A **959**, 163419 (2020).

[7] Y. C. Chao, M. Drury, C. Hovater, A. Hutton, G. A. Krafft, M. Poelker, C. Reece, and M. Tiefenback, CEBAF Accelerator Achievements, Journal of Physics: Conference Series **299**, 012015 (2011).

[8] R. Kazimi, J. M. Grames, J. C. Hansknecht, A. S. Hofler, G. E. Lahti, T. E. Plawski, M. Poelker, R. S. Suleiman, and Y. Wang, Four Beam Generation for Simultaneous Four-Hall Operation at CEBAF 10.18429/JACoW-IPAC2016-THPOY060 (2016).

[9] Y. Roblin, CEBAF Overview, `https://gspda.jlab.org/wiki/index.php/Main_Page#tab=Summer_Lecture_Series3` (2020), [Online; accessed 25-June-2020].

[10] H. Liu, S. Benson, J. Bisognano, P. Liger, G. Neil, D. Neuffer, C. Sinclair, and B. Yunn, Numerical Investigation of a Laser Gun Injector at CEBAF, Nuclear Instruments and Methods in Physics Research Section A: Accelerators, Spectrometers, Detectors and Associated Equipment **339**, 415 (1994).

[11] H. Padamsee, The Science and Technology of Superconducting Cavities for Accelerators, Superconductor Science and Technology **14**, R28 (2001).

[12] A. Bogacz, Introduction to Accelerators, `https://gspda.jlab.org/wiki/index.php/Main_Page#tab=Summer_Lecture_Series3` (2020), [Online; accessed 25-June-2020].

[13] B. J. Holzer, Lattice Design in High-energy Particle Accelerators (2016), arXiv:1601.04913 [physics.acc-ph].

[14] M. Jarrell, A Course in Graduate Electrodynamics (2001).

[15] G. F. Knoll, *Radiation Detection and Measurement, 3rd ed.*, 3rd ed. (John Wiley and Sons, New York, 2000).

[16] V. Ziegler *et al.*, The CLAS12 Software Framework and Event Reconstruction, Nuclear Instruments and Methods in Physics Research Section A: Accelerators, Spectrometers, Detectors and Associated Equipment **959**, 163472 (2020).

[17] M. D. Mestayer *et al.*, The CLAS12 Drift Chamber System, Nuclear Instruments and Methods in Physics Research Section A: Accelerators, Spectrometers, Detectors and Associated Equipment **959**, 163518 (2020).

[18] D. Carman *et al.*, The CLAS12 Forward Time-of-Flight system, Nuclear Instruments and Methods in Physics Research Section A: Accelerators, Spectrometers, Detectors and Associated Equipment **960**, 163629 (2020).

[19] W. R. Leo, *Techniques for Nuclear and Particle Physics Experiments: a How-to Approach* (Springer Science & Business Media, 2012).

[20] E. Smith *et al.*, The Time-of-Flight System for CLAS, Nuclear Instruments and Methods in Physics Research Section A: Accelerators, Spectrometers, Detectors and Associated Equipment **432**, 265 (1999).

[21] M. Amarian *et al.*, The CLAS Forward Electromagnetic Calorimeter, Nuclear Instruments and Methods in Physics Research Section A: Accelerators, Spectrometers, Detectors and Associated Equipment **460**, 239 (2001).

[22] G. Asryan *et al.*, The CLAS12 Forward Electromagnetic Calorimeter, Nuclear Instruments and Methods in Physics Research Section A: Accelerators, Spectrometers, Detectors and Associated Equipment **959**, 163425 (2020).

[23] E. Chudakov, Electromagnetic Calorimeters, `https://userweb.jlab.org/~gen/talks/calor_lect_10.pdf` (2020), [Online; accessed 14-July-2020].

[24] M. Antonioli *et al.*, The CLAS12 Silicon Vertex Tracker, Nuclear Instruments and Methods in Physics Research Section A: Accelerators, Spectrometers, Detectors and Associated Equipment **962**, 163701 (2020).

[25] A. Acker *et al.*, The CLAS12 Micromegas Vertex Tracker, Nuclear Instruments and Methods in Physics Research Section A: Accelerators, Spectrometers, Detectors and Associated Equipment **957**, 163423 (2020).

[26] V. Gyurjyan, D. Abbott, J. Carbonneau, G. Gilfoyle, D. Heddle, G. Heyes, S. Paul, C. Timmer, D. Weygand, and E. Wolin, CLARA: A Contemporary Approach to Physics Data Processing, Journal of Physics: Conference Series **331**, 032013 (2011).

[27] E. Süli and D. Mayers, *An Introduction to Numerical Analysis* (Cambridge University Press, 2003).

[28] M. Ungaro *et al.*, The CLAS12 Geant4 Simulation, Nuclear Instruments and Methods in Physics Research Section A: Accelerators, Spectrometers, Detectors and Associated Equipment **959**, 163422 (2020).

[29] F. Gross, Making the Case for Jefferson Lab, in *J. Phys. Conf. Ser.*, Vol. 299 (Thomas Jefferson National Accelerator Facility, Newport News, VA (United States), 2011).

[30] R. C. York and D. R. Douglas, Optics of the CEBAF CW Superconducting Accelerator. (1987).

Appendix B

Additional Results Produced During the Course of This Study

B.1 The HTCC Resolutions for Each Event File

Event File	Δx	Δy	Δz	$\Delta\phi$	$\Delta\theta$	Δb
6 GeV e^-	0.14224	0.26871	0.07216	0.22496	0.05920	0.15909
6 GeV μ^-	0.12067	0.21764	0.06148	0.16634	0.05163	0.13992
6 GeV π^-	0.12526	0.21754	0.06331	0.16682	0.05357	0.14468
3 GeV e^-	0.28961	0.33924	0.14639	0.26645	0.12423	0.32176
4.5 GeV e^-	0.18046	0.28126	0.08919	0.22661	0.07654	0.20067
7.5 GeV e^-	0.11233	0.23361	0.05276	0.20878	0.04620	0.12354
9 GeV e^-	0.09898	0.23964	0.04590	0.20245	0.03956	0.10431
6 GeV e^-, RGA	0.12321	0.22838	0.06196	0.21298	0.04767	0.14088
6 GeV e^-, RGB	0.12073	0.22626	0.05995	0.21518	0.04702	0.13936
6 GeV e^-, $t = +1$	0.13673	0.28365	0.06753	0.25740	0.05934	0.16224

The resolutions at the HTCC for various event files: RGA, RGB denote the Run Group A and Run Group B detector configurations. The $t = +1$ is the value of the torus field: $t = +1$ is the out-bending torus configuration, the opposite from the default polarity.)

B.2 Plots of Events Created With Different Versions of GEMC

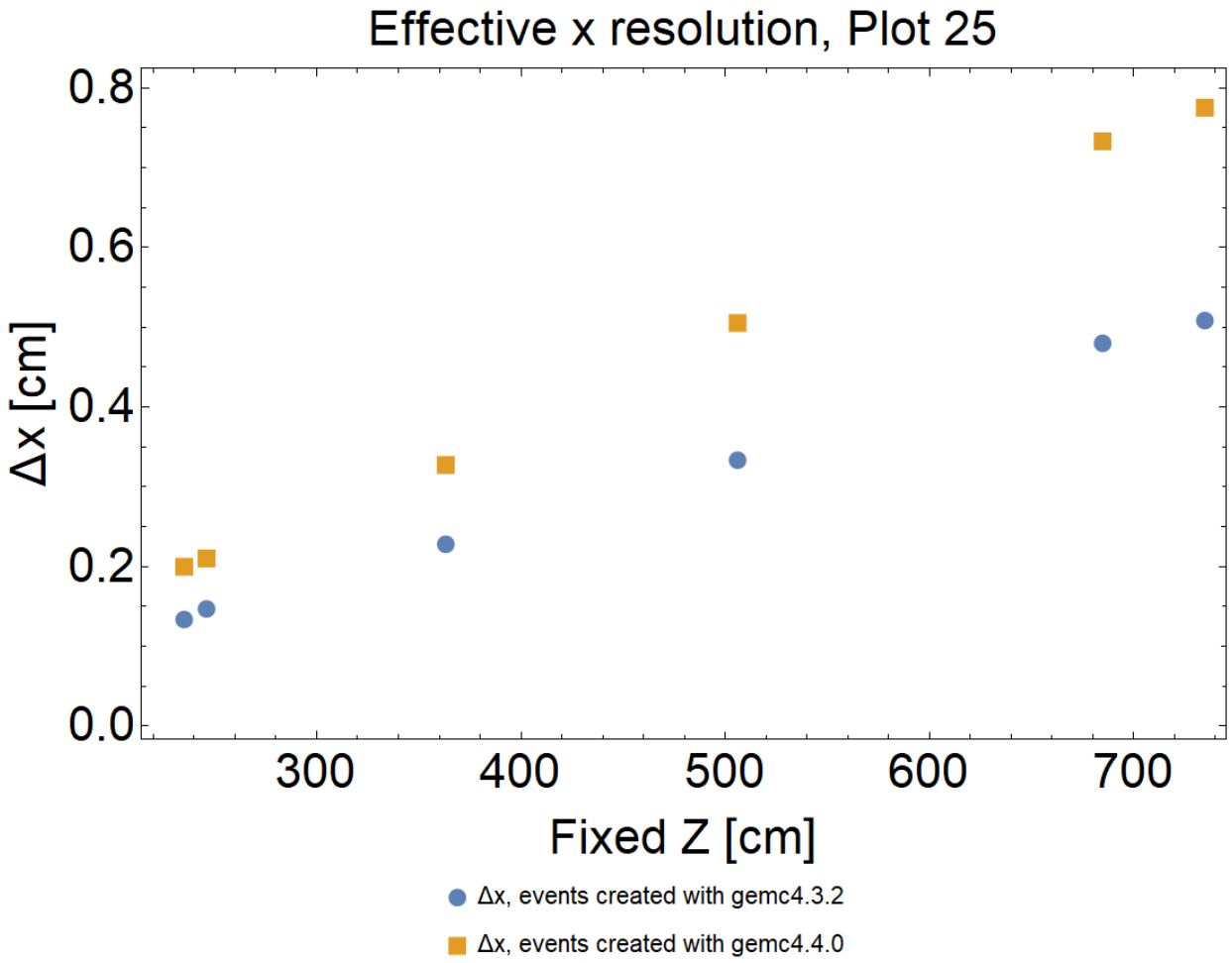

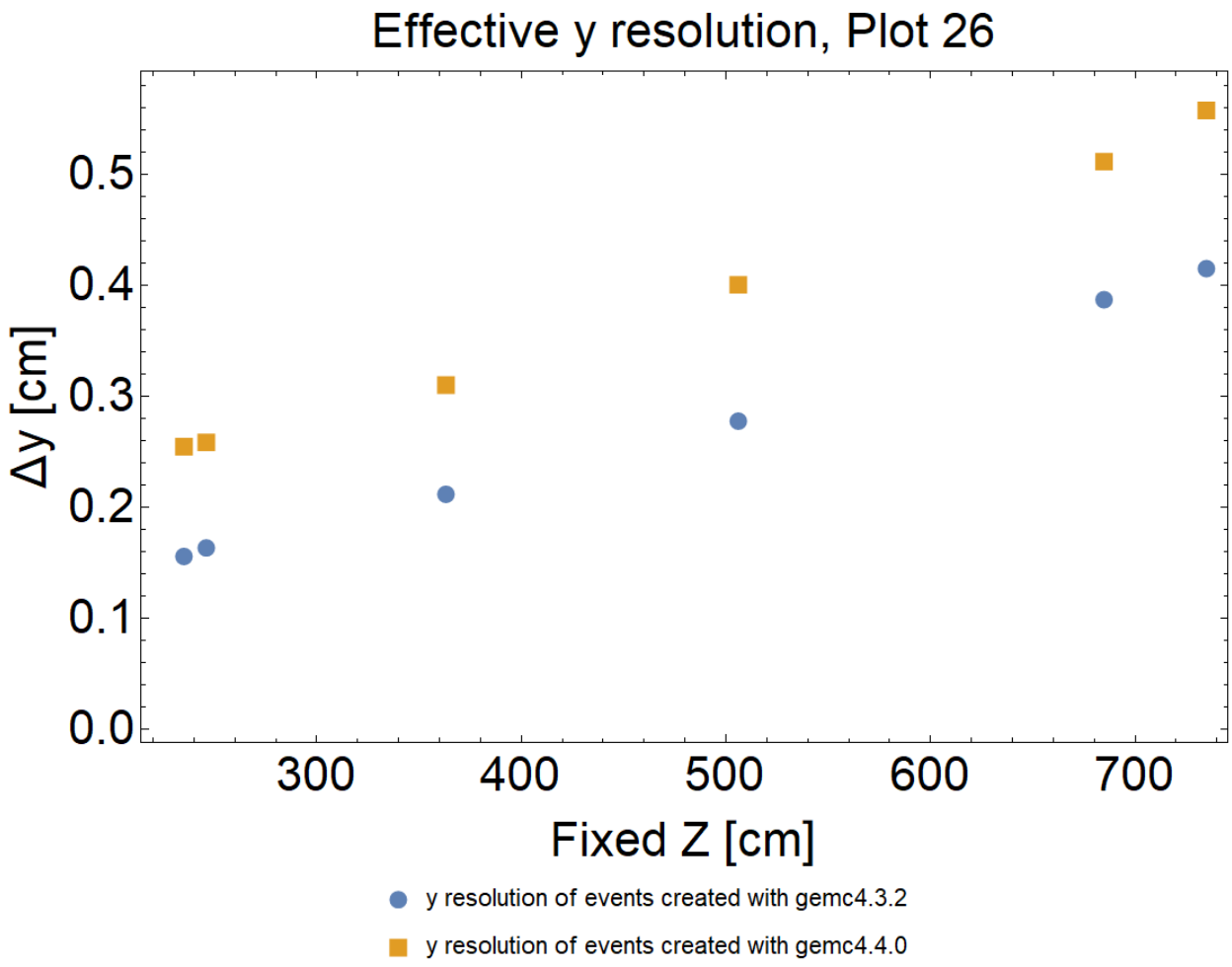
Effective y resolution, Plot 26
Δy [cm]
0.0
0.1
0.2
0.3
0.4
0.5
300
400
500
600
700
Fixed Z [cm]
y resolution of events created with gemc4.3.2
y resolution of events created with gemc4.4.0

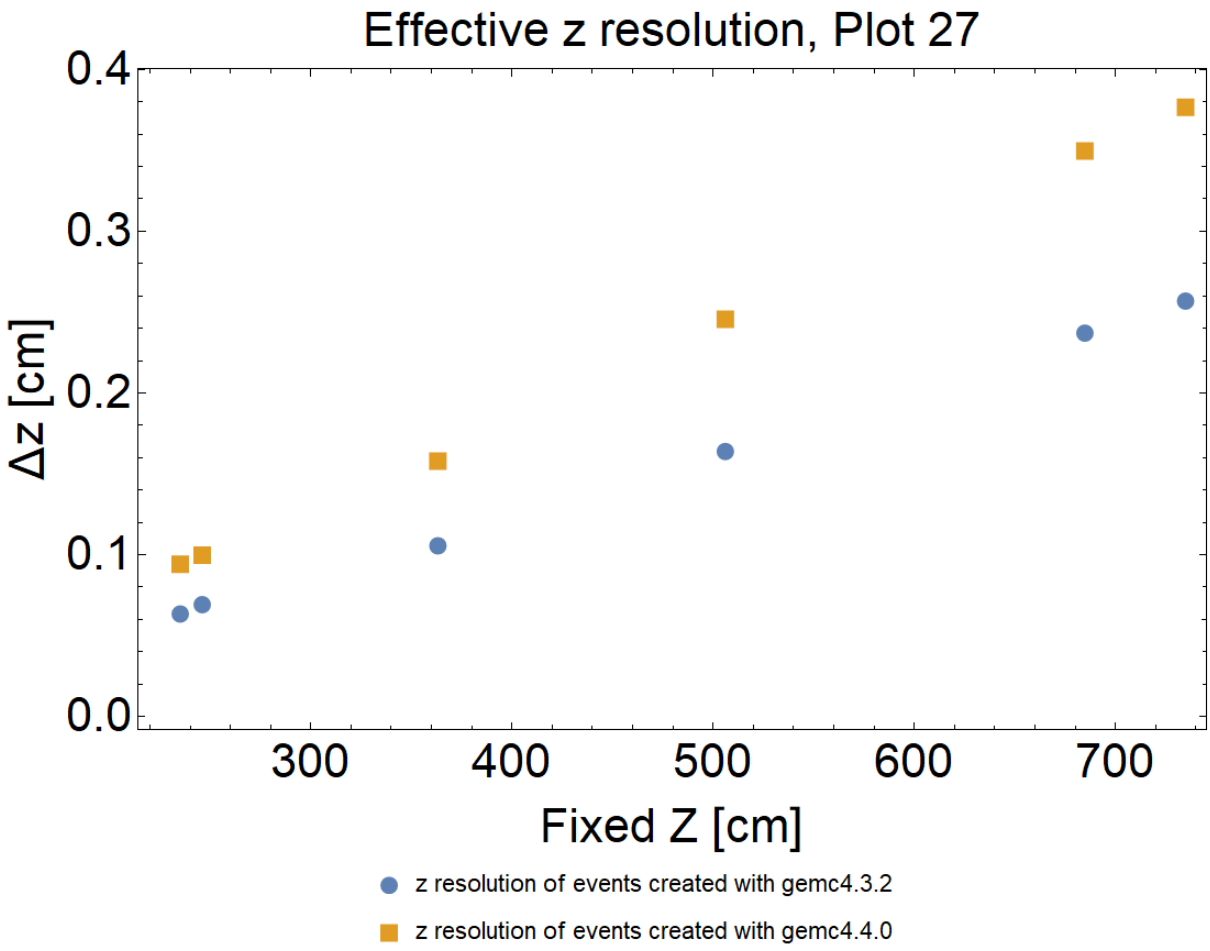
Effective z resolution, Plot 27
0.4
0.3
0.2
0.1
0.0
Δz [cm]
300
400
500
600
700
Fixed Z [cm]
z resolution of events created with gemc4.3.2
z resolution of events created with gemc4.4.0

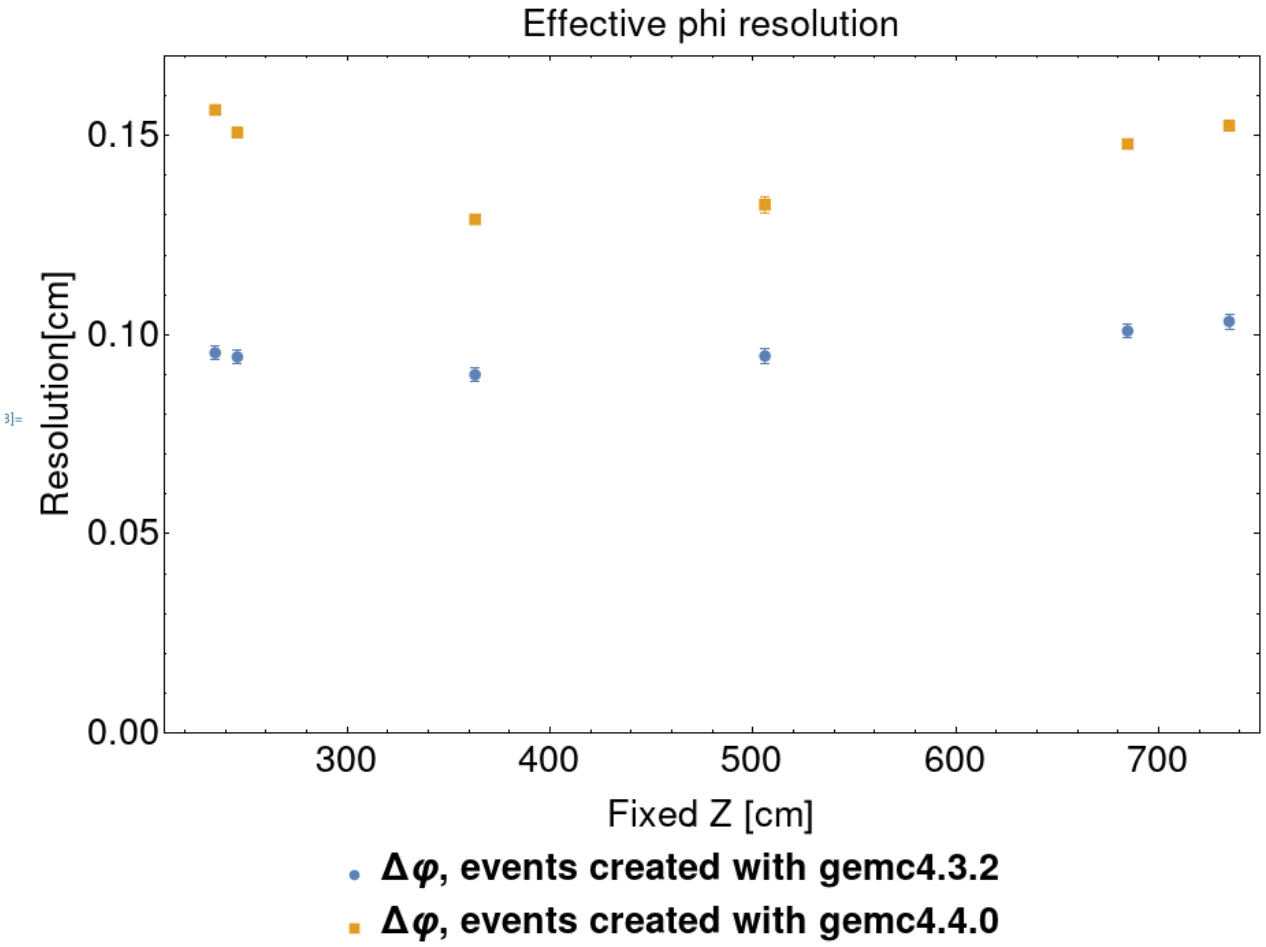
Effective phi resolution
Resolution[cm]
0.15
0.10
0.05
0.00
300
400
500
600
700
Fixed Z [cm]
Δφ, events created with gemc4.3.2
Δφ, events created with gemc4.4.0

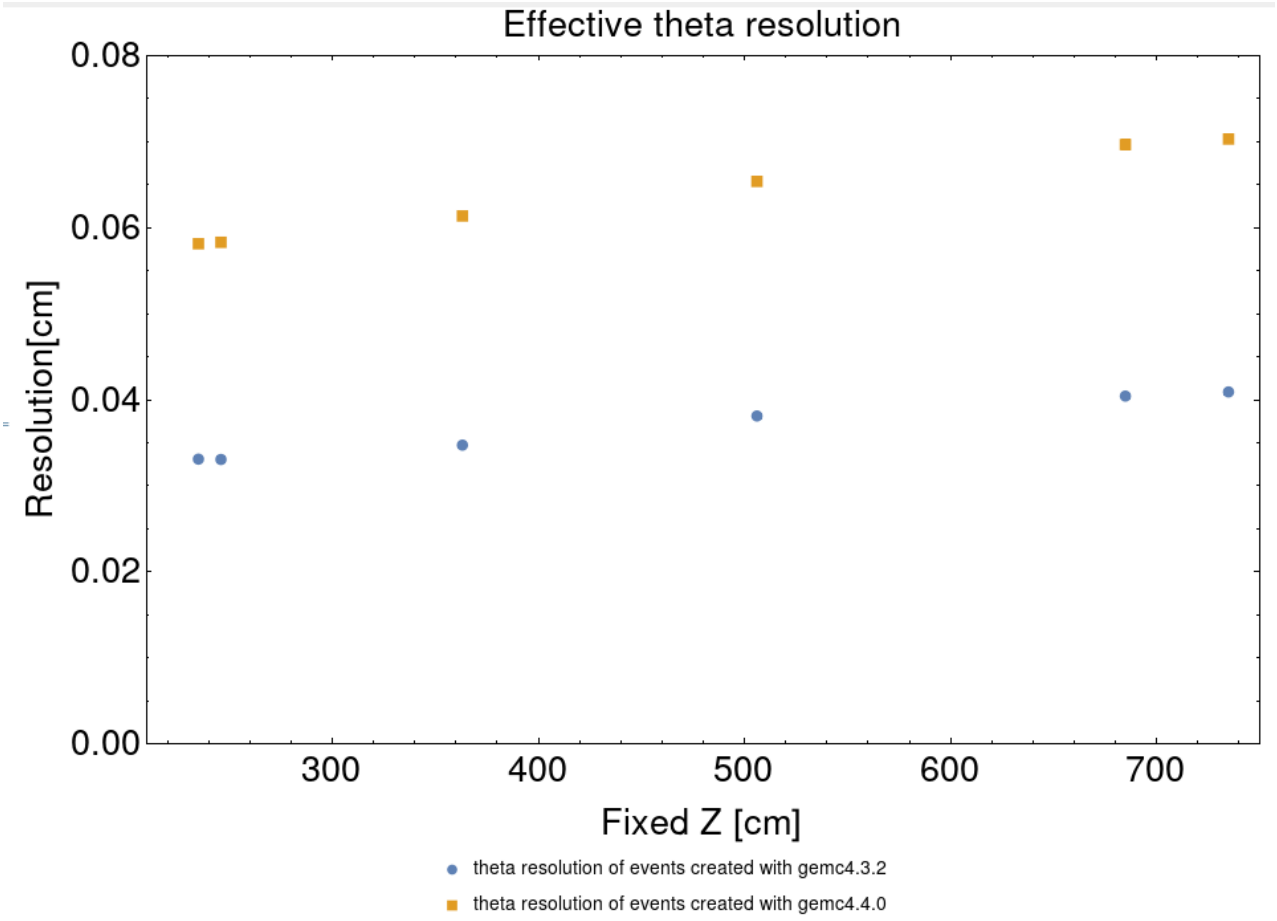
Effective theta resolution
0.08
0.06
0.04
0.02
0.00
Resolution[cm]
300
400
500
600
700
Fixed Z [cm]
theta resolution of events created with gemc4.3.2
theta resolution of events created with gemc4.4.0

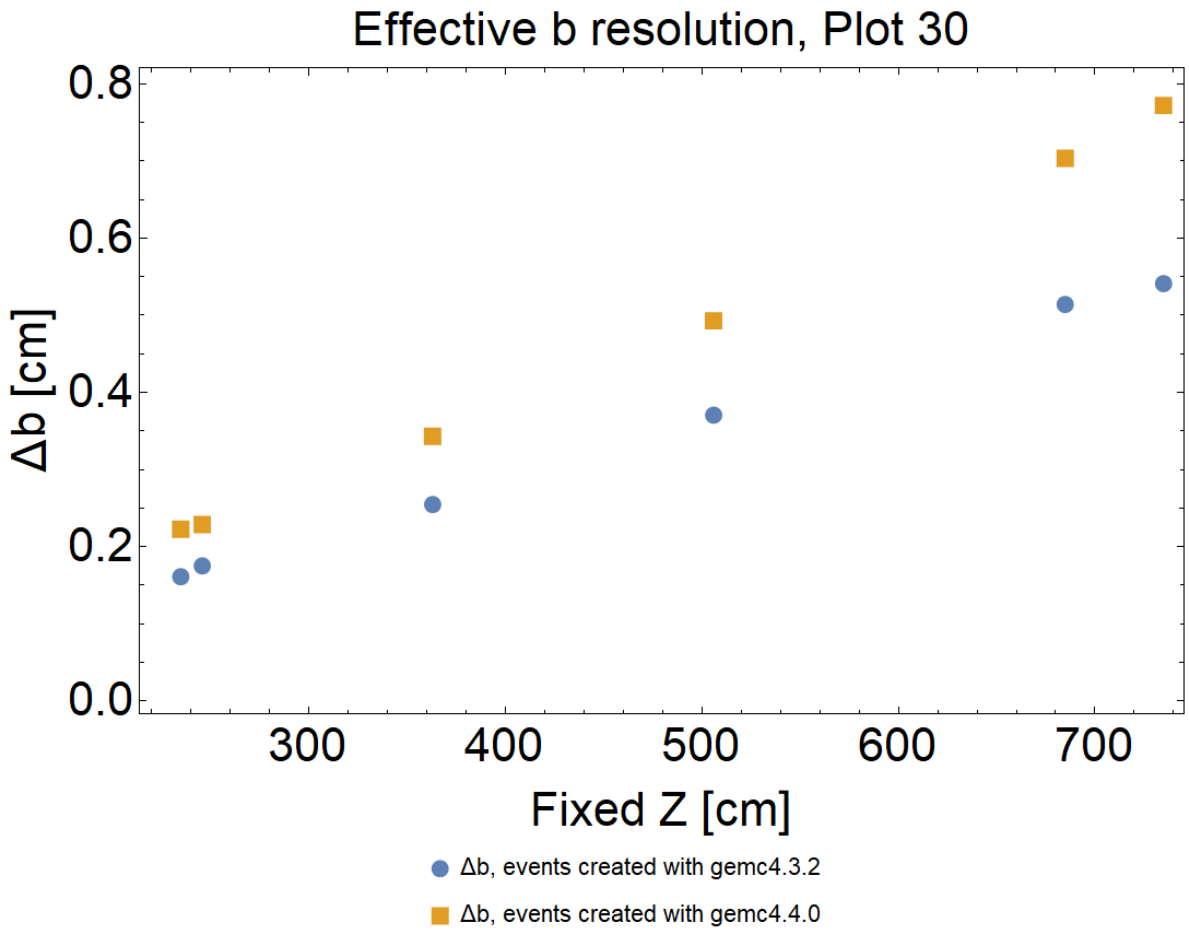
Effective b resolution, Plot 30
0.8
0.6
0.4
0.2
0.0
Δb [cm]
300
400
500
600
700
Fixed Z [cm]
Δb, events created with gemc4.3.2
Δb, events created with gemc4.4.0

B.3 Plots of Events in Different Detection Sectors

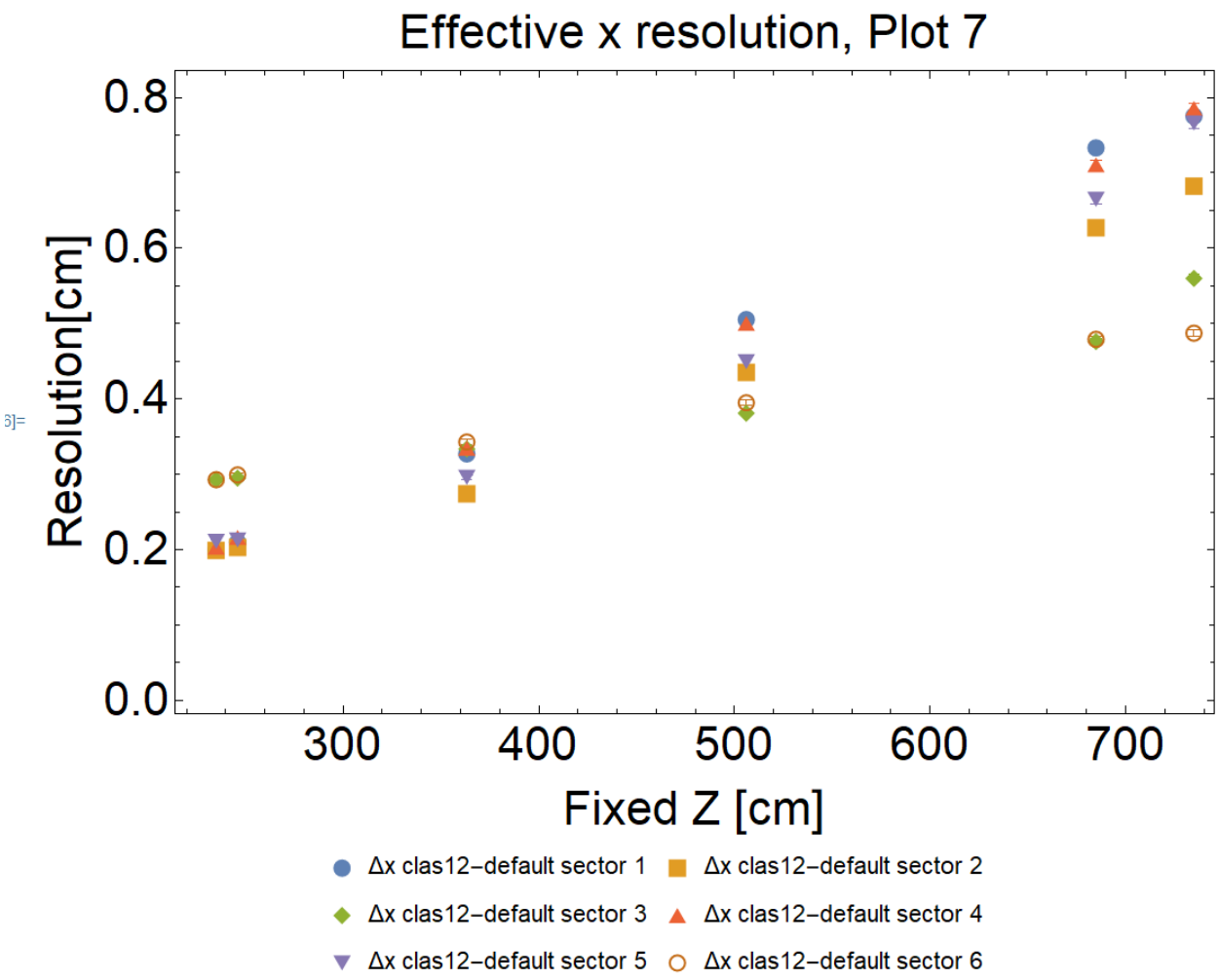

NOTE: The x and y axis resolutions in sectors 3 and 6 differ due to the definition of the axes: the x resolutions in these two sectors coincide with the y resolutions in the other sectors, and the y resolutions coincide with the x resolutions of the other sectors.

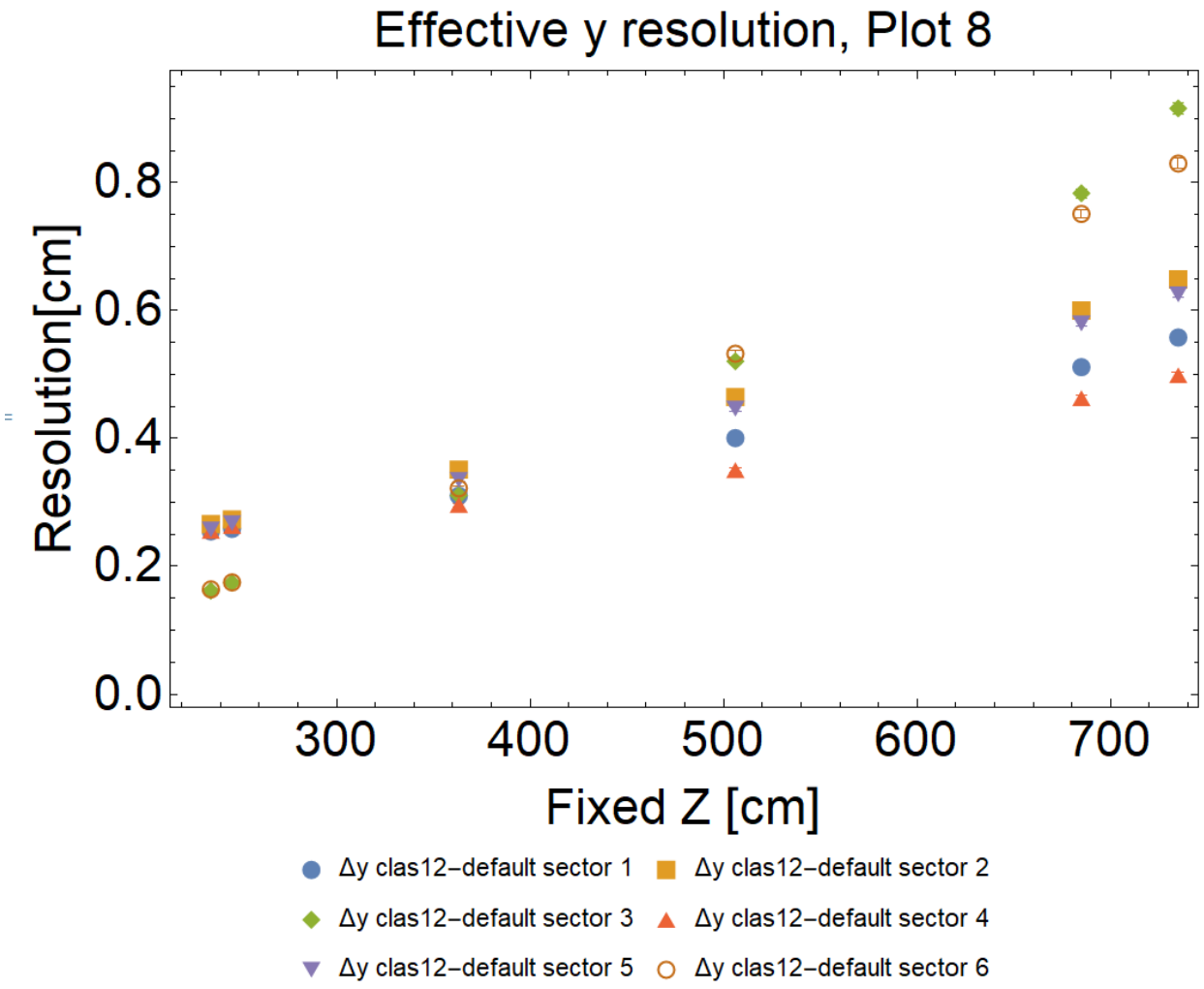
Effective y resolution, Plot 8
Resolution[cm]
0.0
0.2
0.4
0.6
0.8
300
400
500
600
700
Fixed Z [cm]
Δy clas12−default sector 1
Δy clas12−default sector 2
Δy clas12−default sector 3
Δy clas12−default sector 4
Δy clas12−default sector 5
Δy clas12−default sector 6

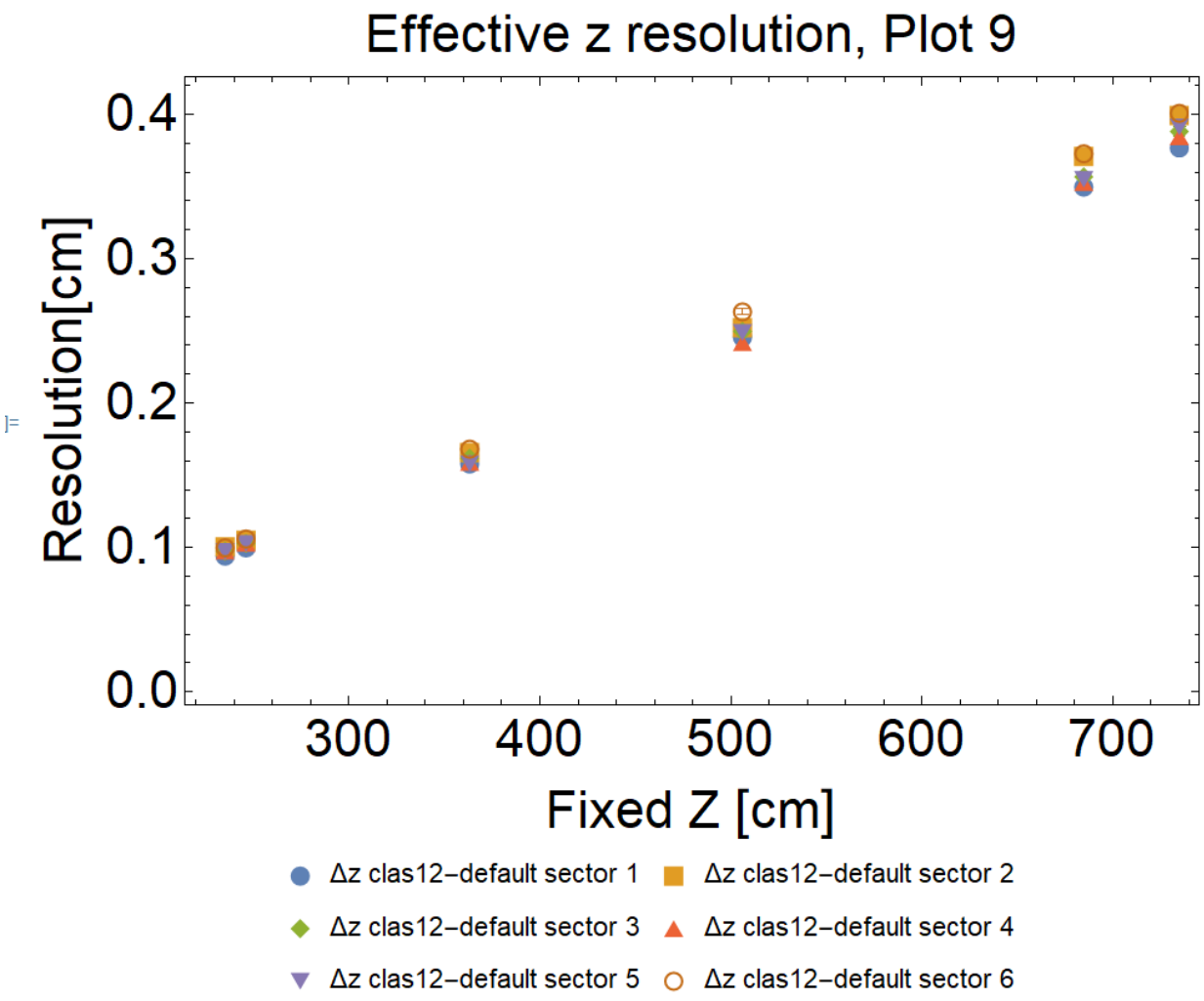
Effective z resolution, Plot 9
Resolution[cm]
0.0
0.1
0.2
0.3
0.4
300
400
500
600
700
Fixed Z [cm]
Δz clas12−default sector 1
Δz clas12−default sector 2
Δz clas12−default sector 3
Δz clas12−default sector 4
Δz clas12−default sector 5
Δz clas12−default sector 6

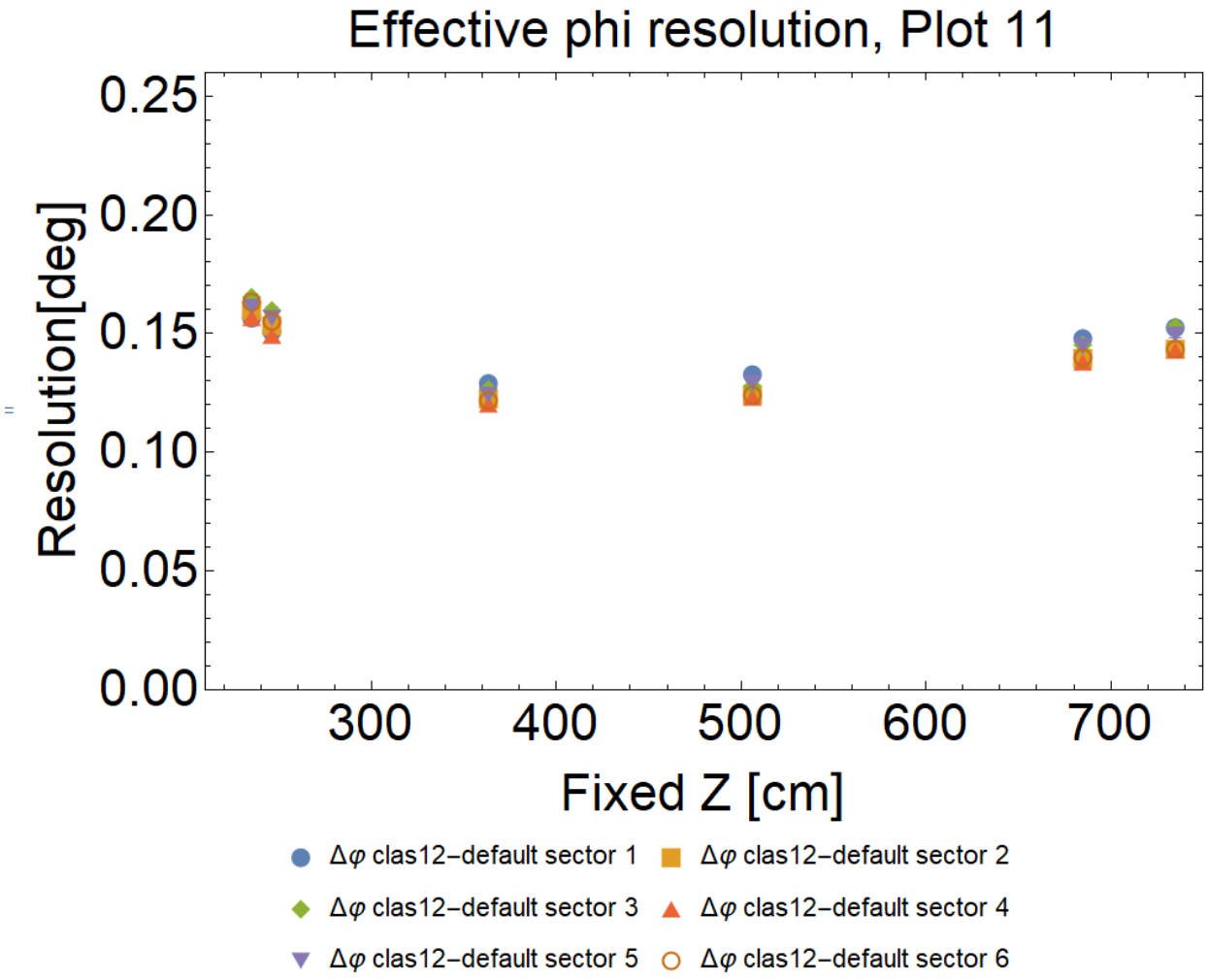
Effective phi resolution, Plot 11
Resolution[deg]
0.25
0.20
0.15
0.10
0.05
0.00
300
400
500
600
700
Fixed Z [cm]
Δφ clas12−default sector 1
Δφ clas12−default sector 2
Δφ clas12−default sector 3
Δφ clas12−default sector 4
Δφ clas12−default sector 5
Δφ clas12−default sector 6

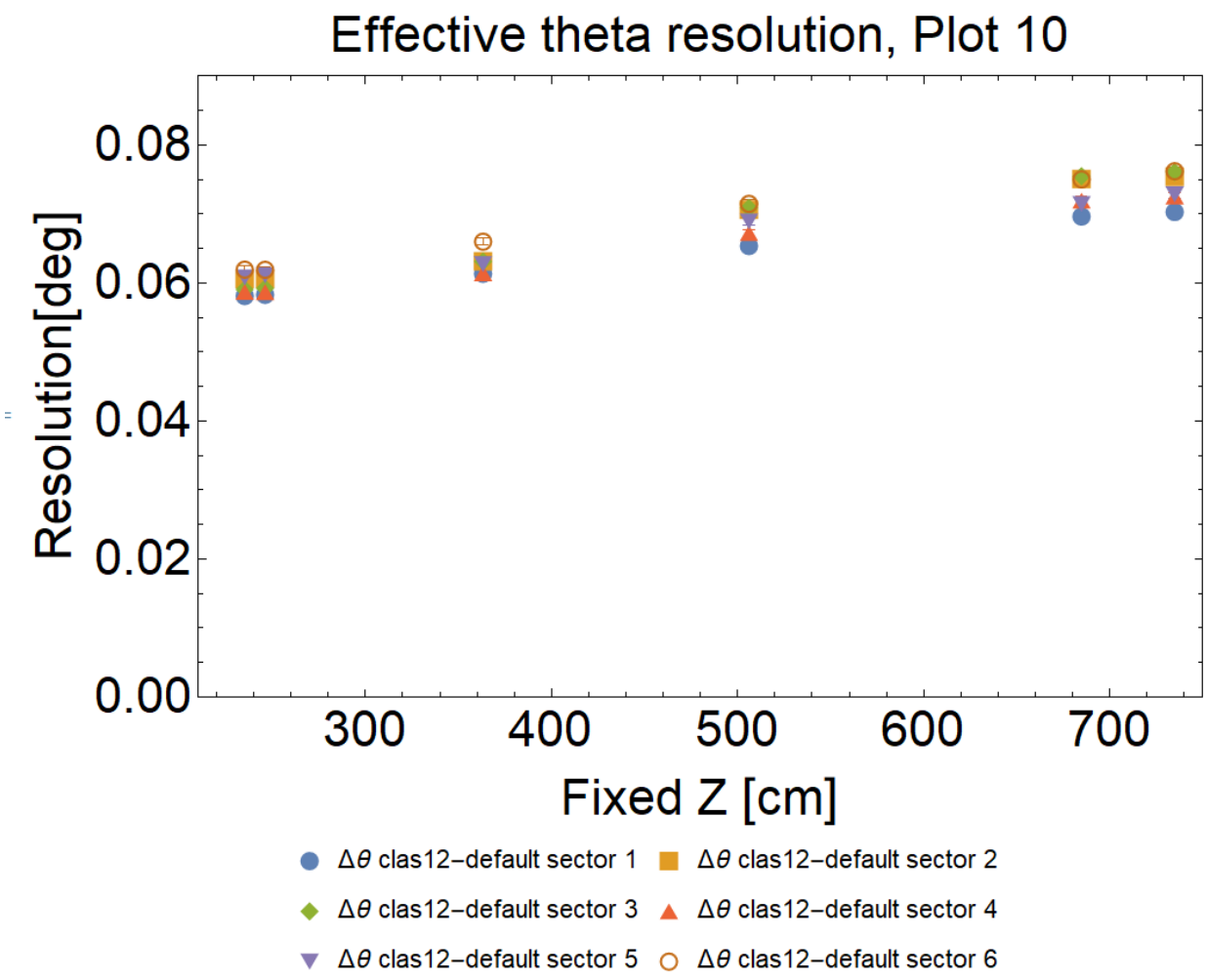
Effective theta resolution, Plot 10
Resolution[deg]
0.00
0.02
0.04
0.06
0.08
300
400
500
600
700
Fixed Z [cm]
Δθ clas12−default sector 1
Δθ clas12−default sector 2
Δθ clas12−default sector 3
Δθ clas12−default sector 4
Δθ clas12−default sector 5
Δθ clas12−default sector 6

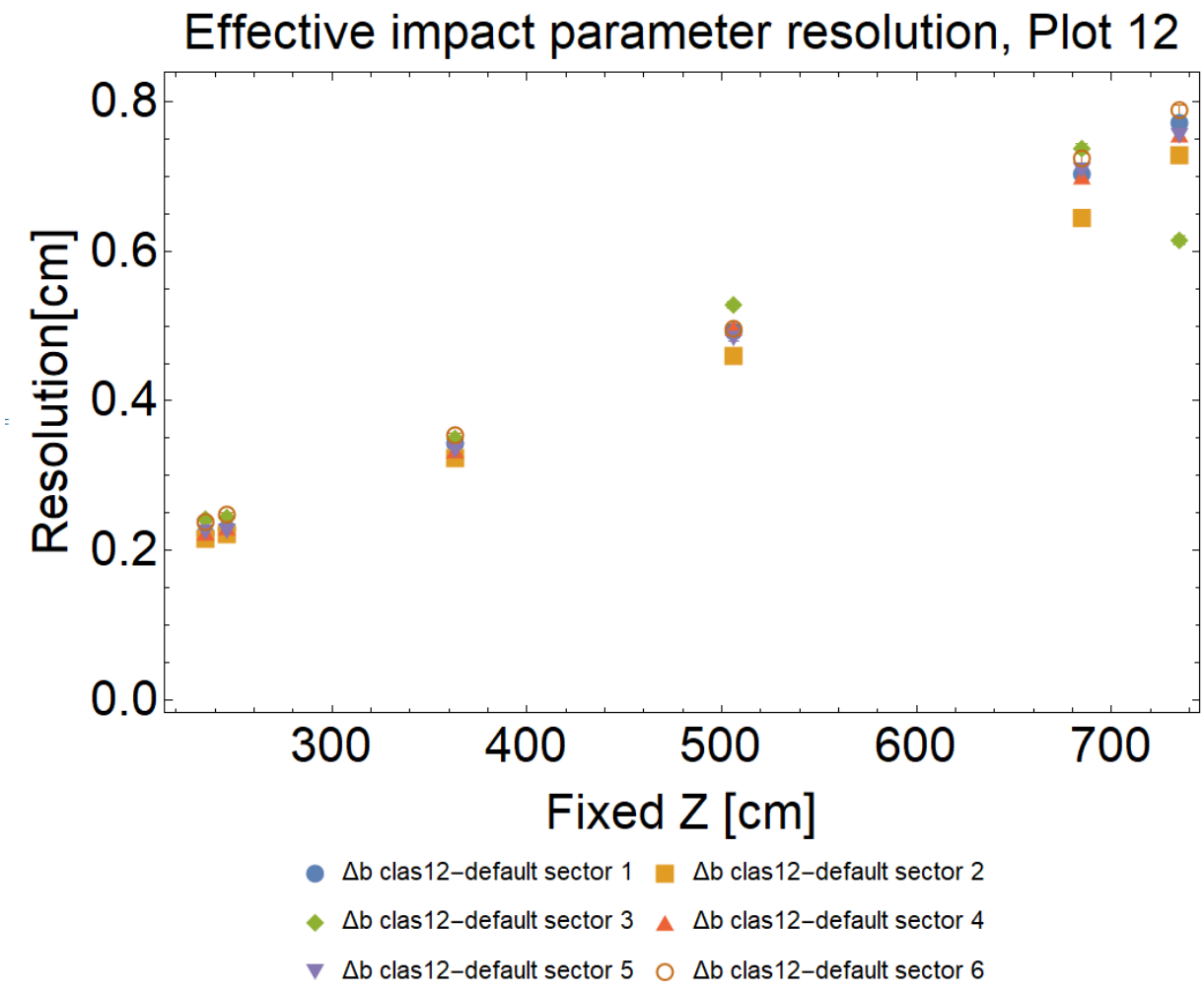
Effective impact parameter resolution, Plot 12
Resolution[cm]
0.0
0.2
0.4
0.6
0.8
300
400
500
600
700
Fixed Z [cm]
Δb clas12−default sector 1
Δb clas12−default sector 2
Δb clas12−default sector 3
Δb clas12−default sector 4
Δb clas12−default sector 5
Δb clas12−default sector 6

B.4 Plots of Events of Different Particle Species

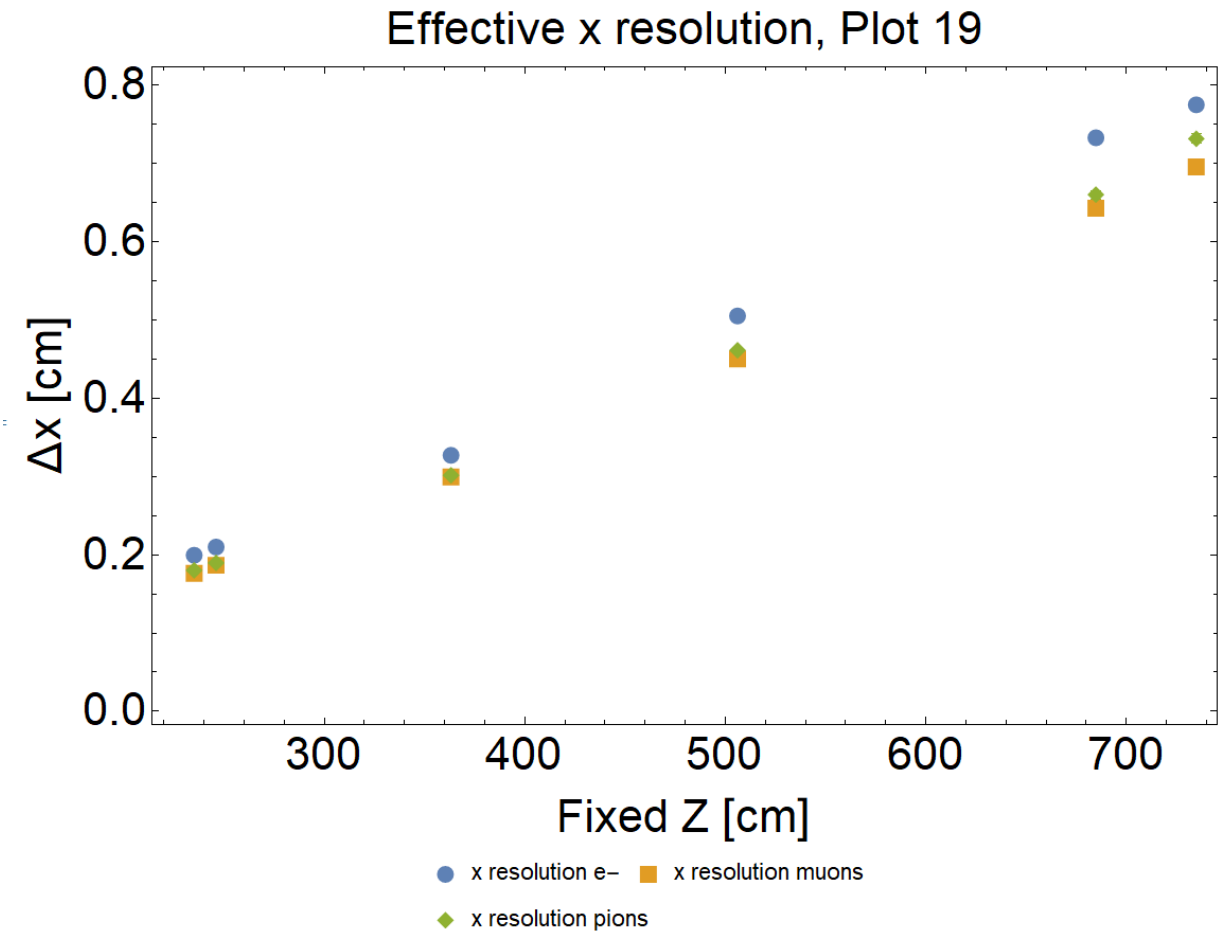

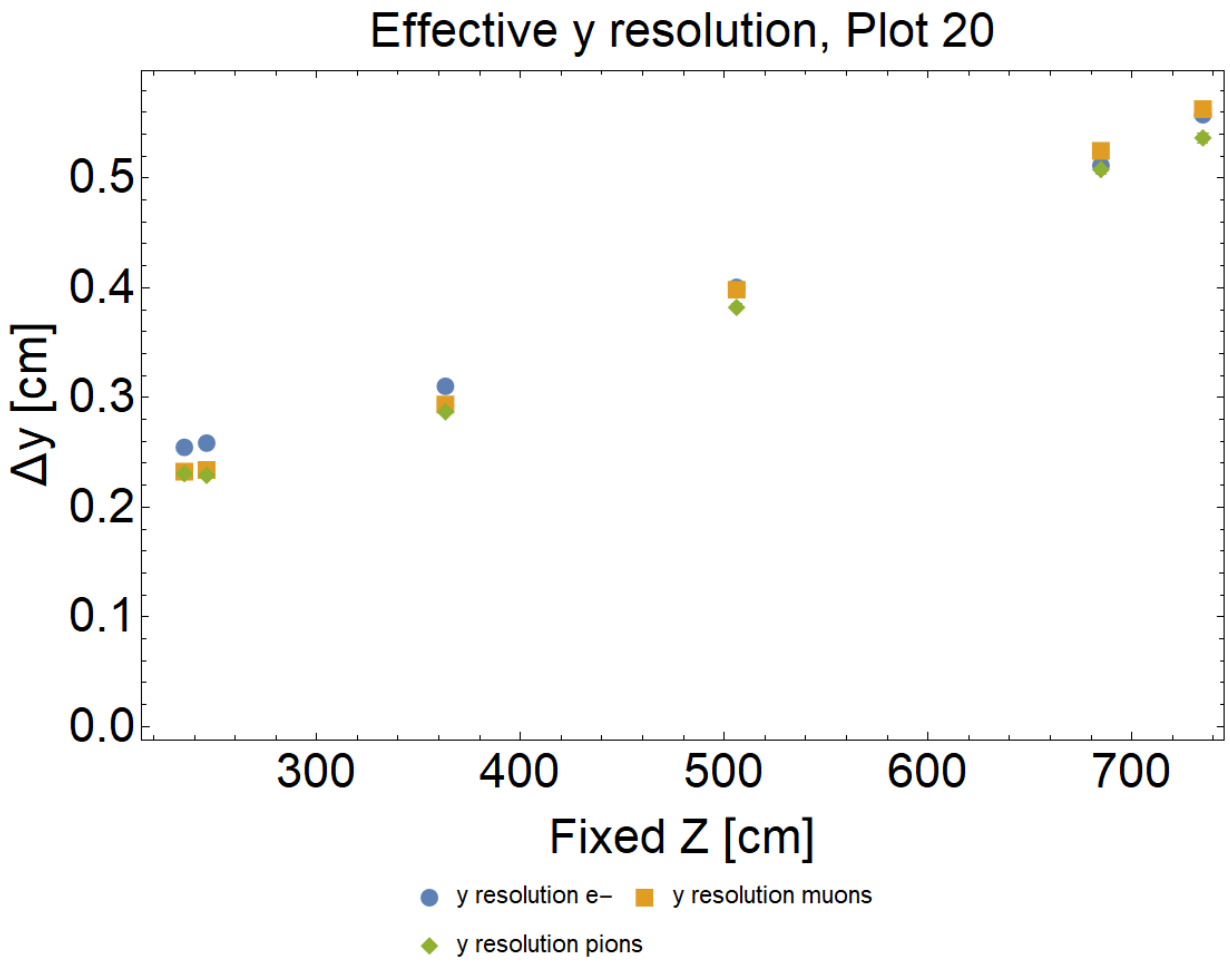
Effective y resolution, Plot 20
Δy [cm]
0.0
0.1
0.2
0.3
0.4
0.5
300
400
500
600
700
Fixed Z [cm]
y resolution e−
y resolution muons
y resolution pions

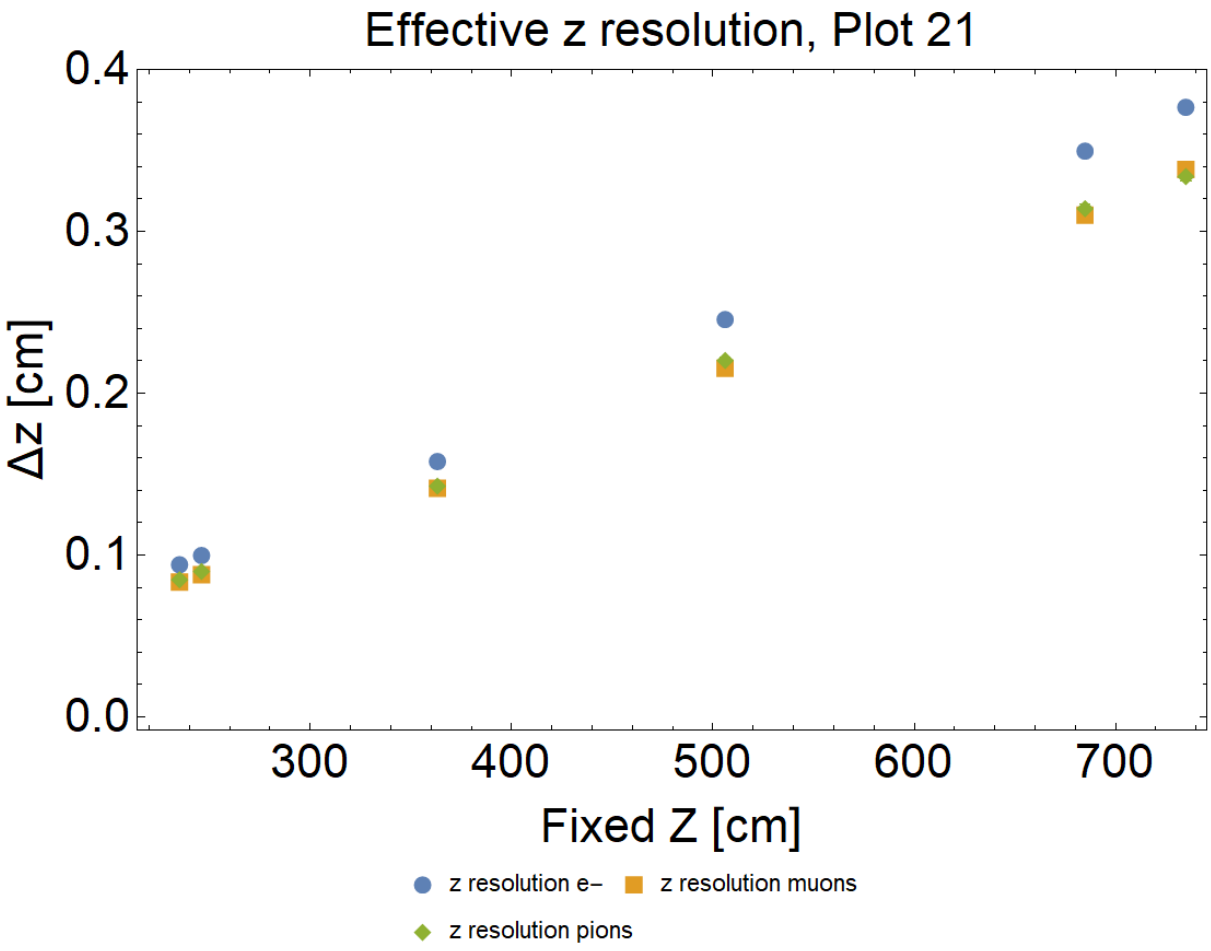
Effective z resolution, Plot 21
0.4
0.3
0.2
0.1
0.0
Δz [cm]
300
400
500
600
700
Fixed Z [cm]
z resolution e−
z resolution muons
z resolution pions

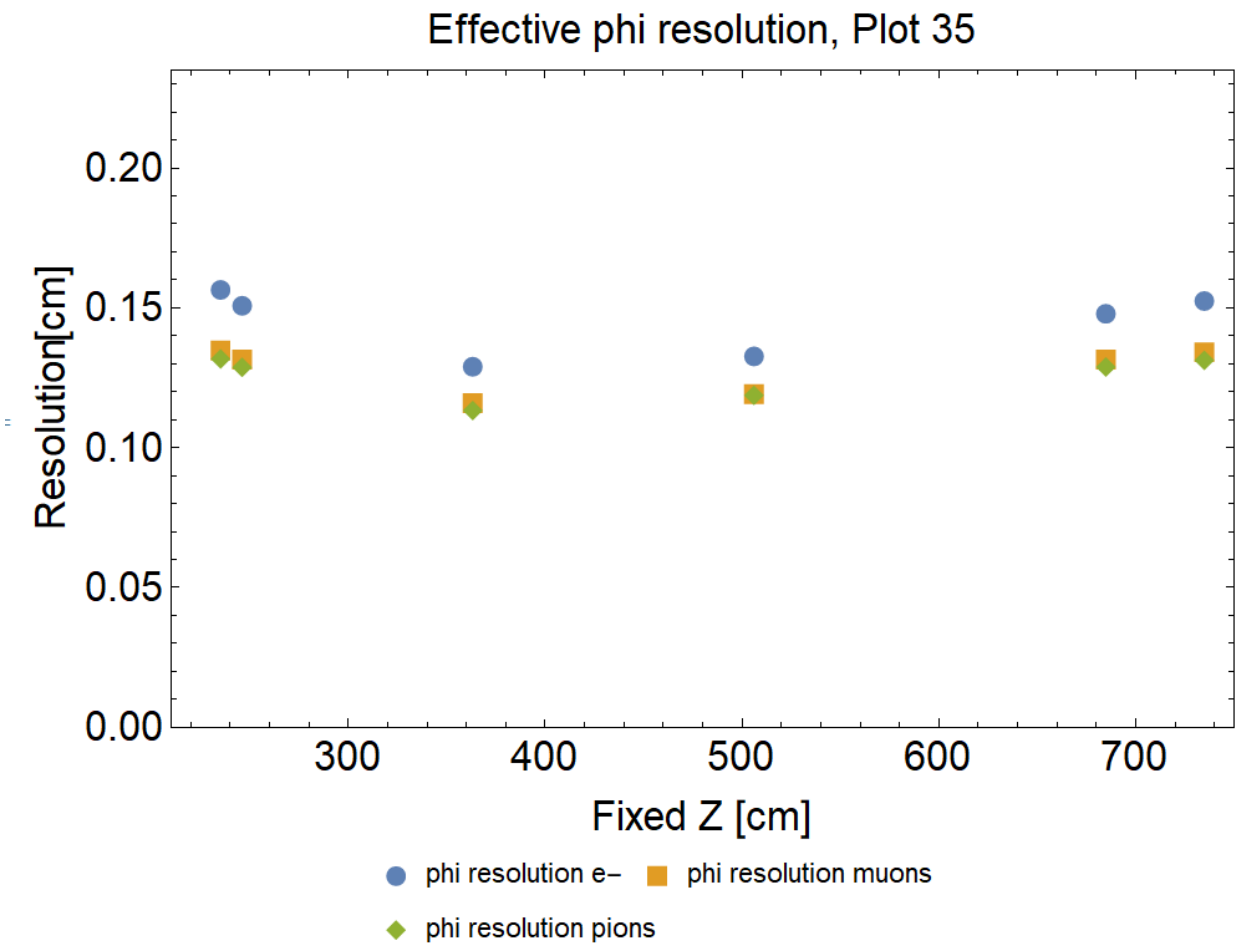
Effective phi resolution, Plot 35
Resolution[cm]
0.20
0.15
0.10
0.05
0.00
300
400
500
600
700
Fixed Z [cm]
phi resolution e−
phi resolution muons
phi resolution pions

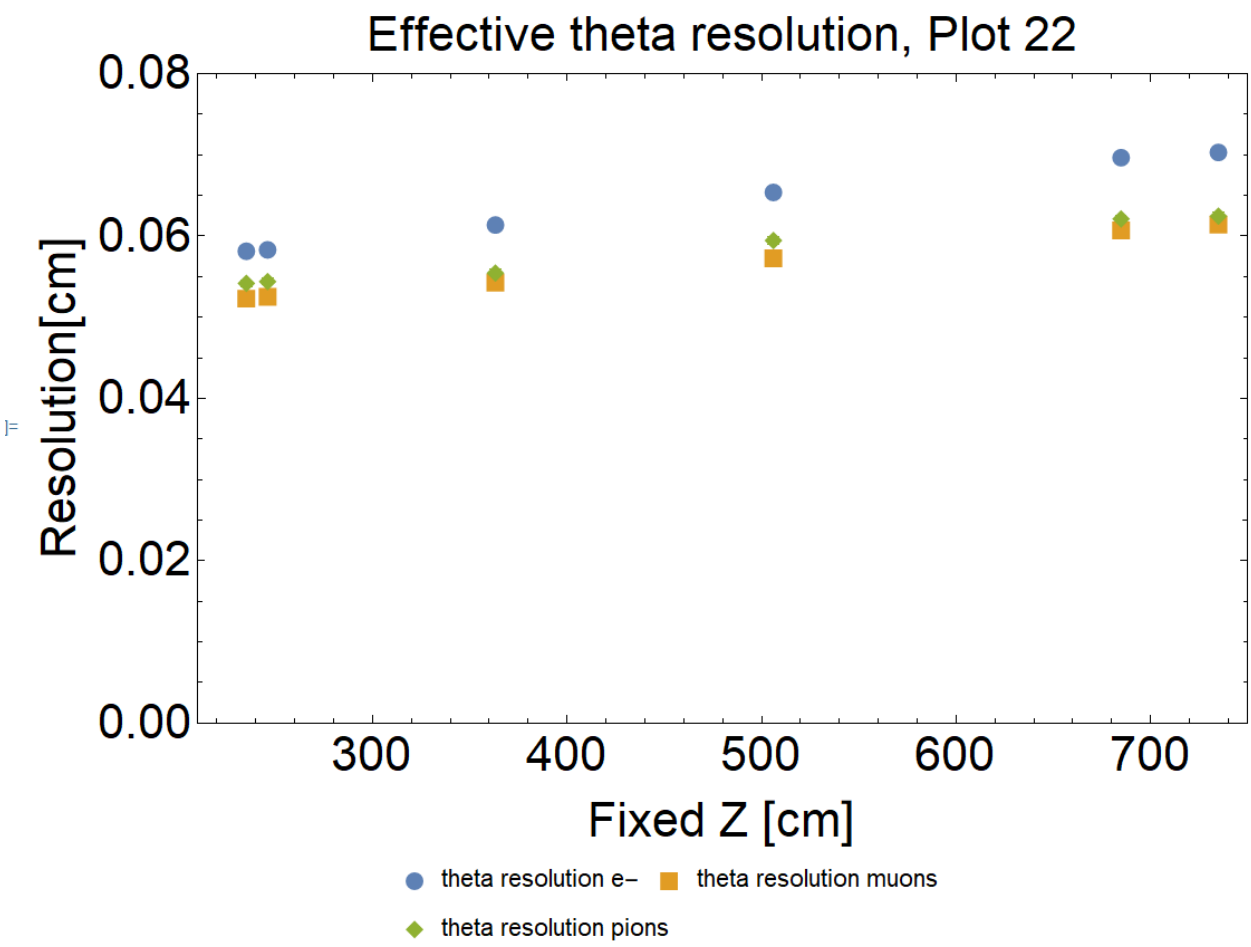
Effective theta resolution, Plot 22
Resolution[cm]
0.08
0.06
0.04
0.02
0.00
300
400
500
600
700
Fixed Z [cm]
theta resolution e−
theta resolution muons
theta resolution pions

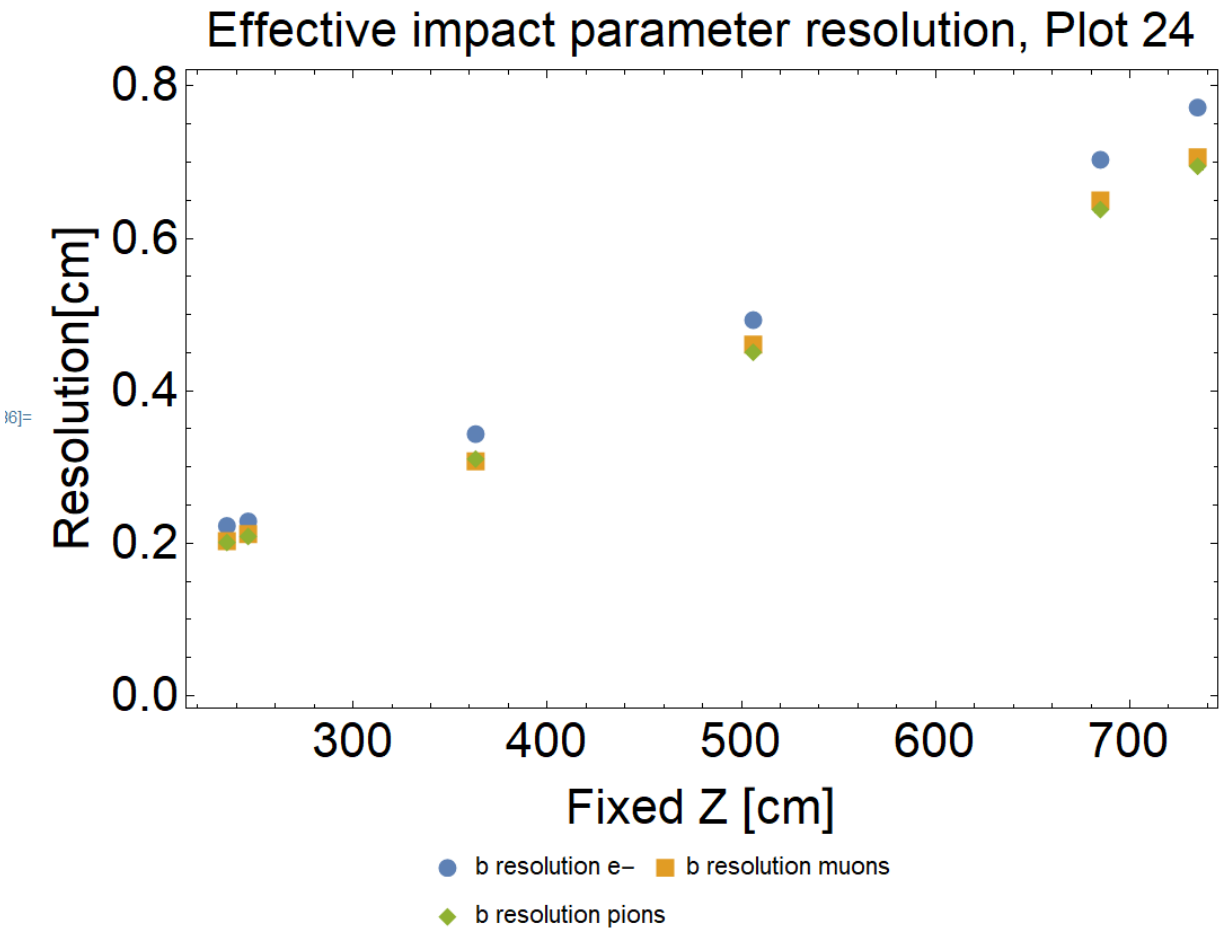
Effective impact parameter resolution, Plot 24
Resolution[cm]
0.0
0.2
0.4
0.6
0.8
300
400
500
600
700
Fixed Z [cm]
b resolution e−
b resolution muons
b resolution pions

B.5 Plots of Events of Different Particle Energies

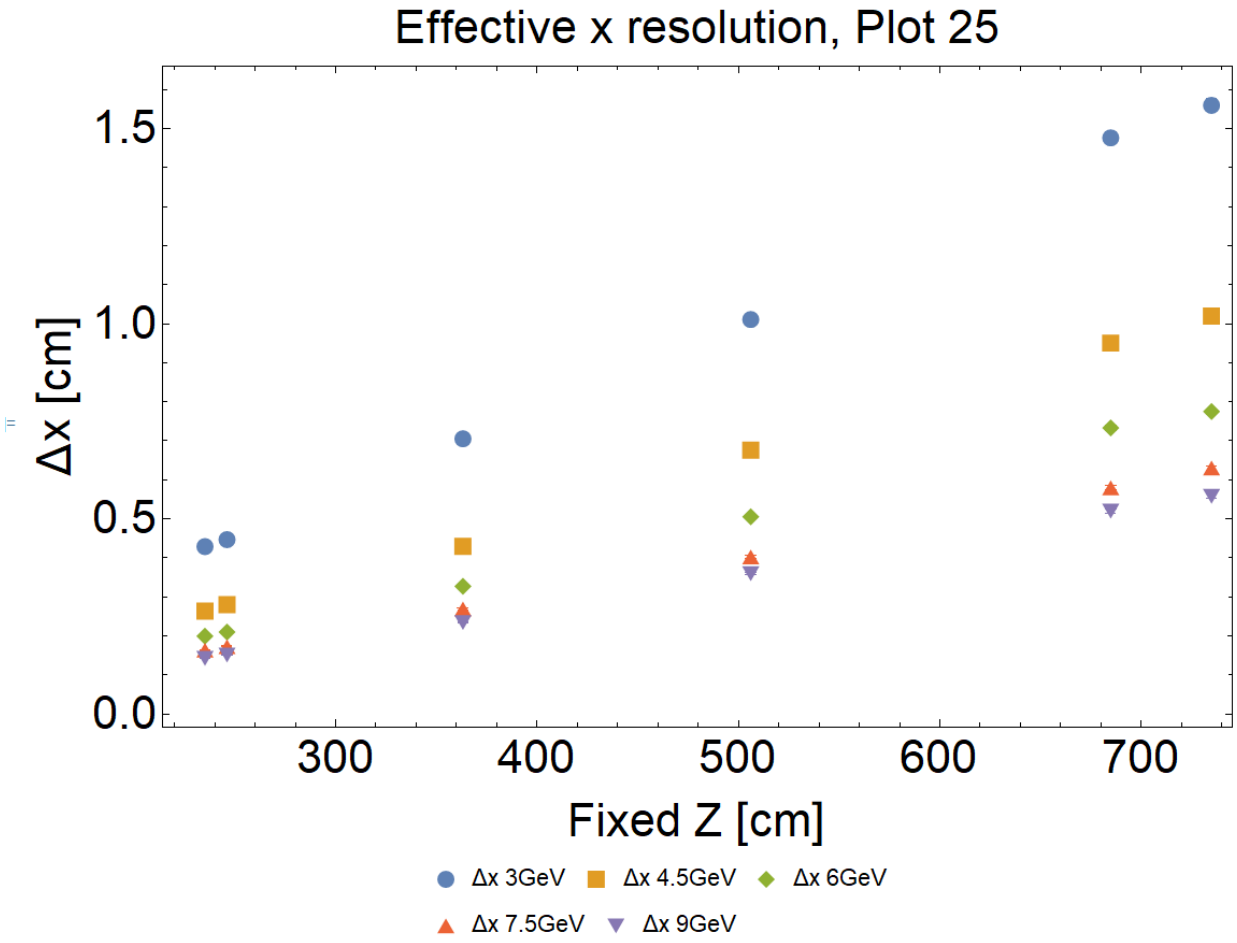

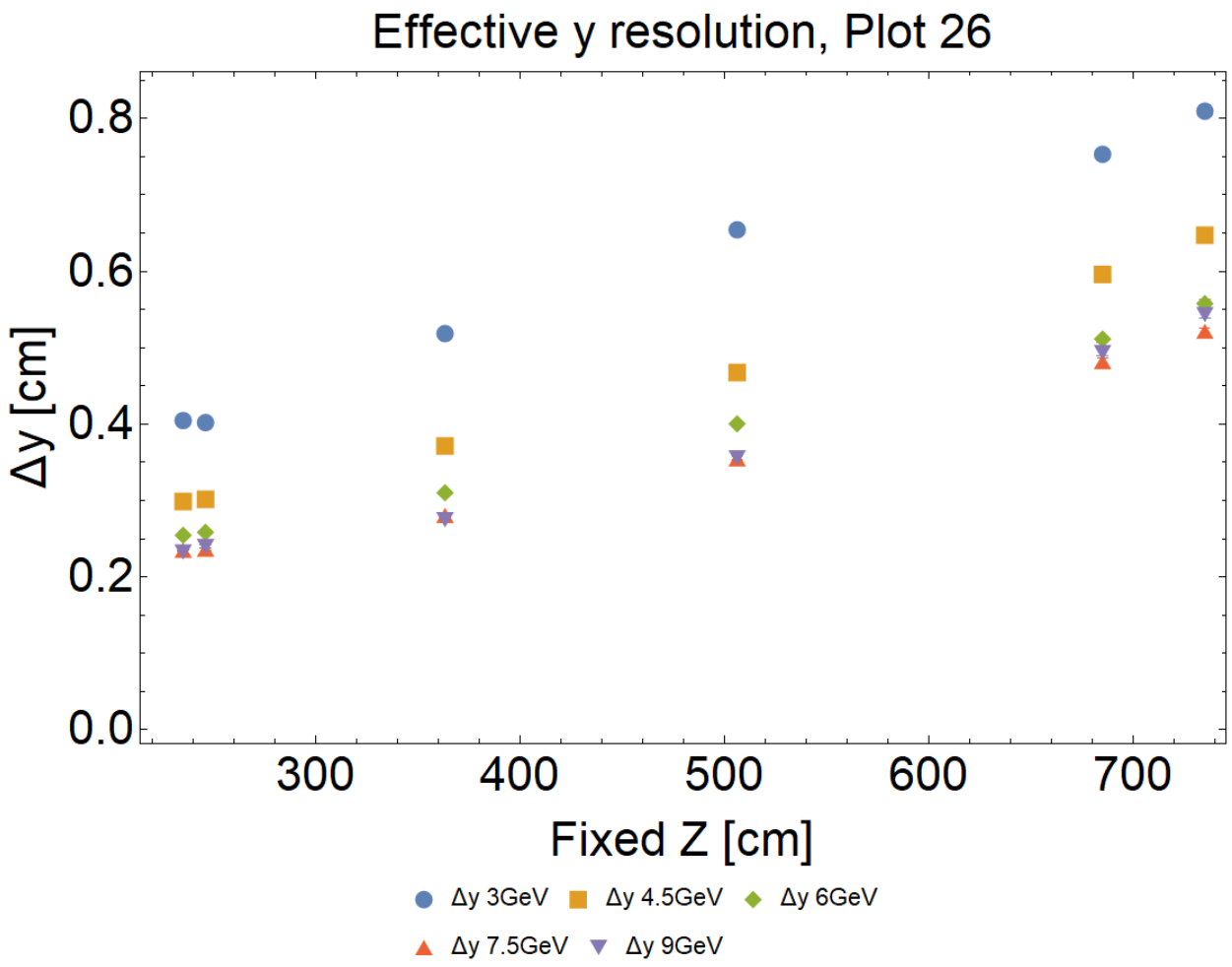
Effective y resolution, Plot 26
Δy [cm]
0.0
0.2
0.4
0.6
0.8
300
400
500
600
700
Fixed Z [cm]
Δy 3GeV
Δy 4.5GeV
Δy 6GeV
Δy 7.5GeV
Δy 9GeV

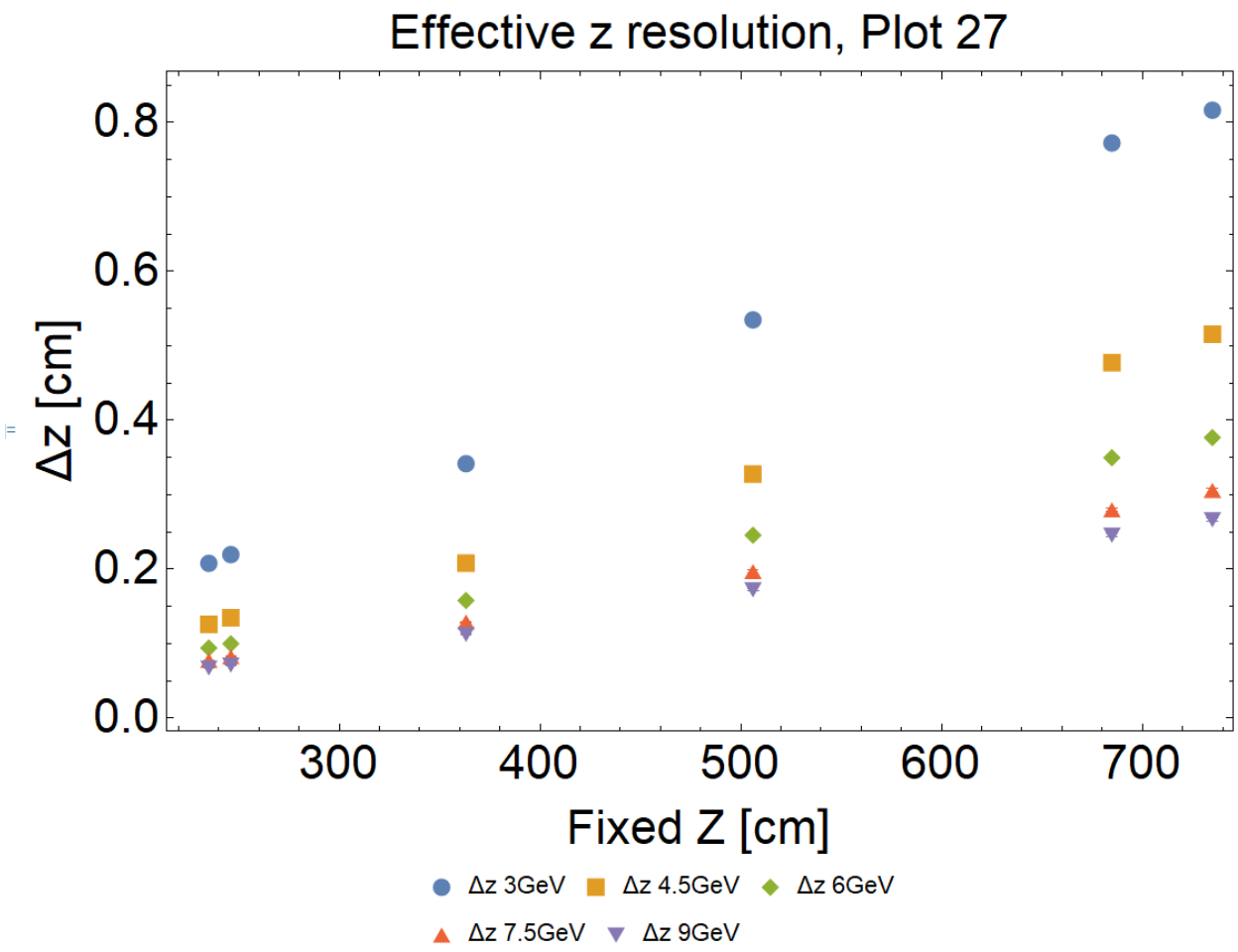
Effective z resolution, Plot 27
Δz [cm]
0.0
0.2
0.4
0.6
0.8
300
400
500
600
700
Fixed Z [cm]
Δz 3GeV
Δz 4.5GeV
Δz 6GeV
Δz 7.5GeV
Δz 9GeV

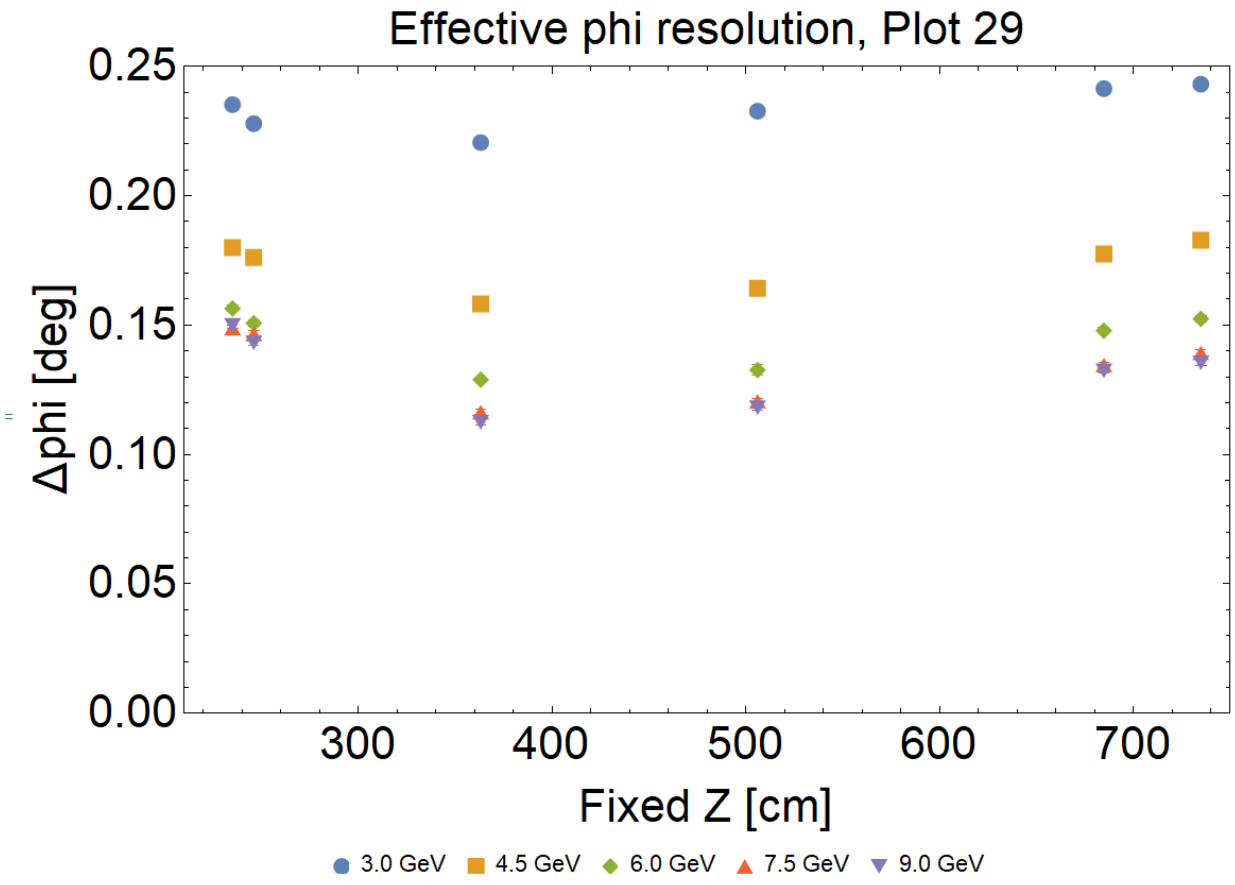
Effective phi resolution, Plot 29
0.25
0.20
0.15
0.10
0.05
0.00
Δphi [deg]
300
400
500
600
700
Fixed Z [cm]
3.0 GeV
4.5 GeV
6.0 GeV
7.5 GeV
9.0 GeV

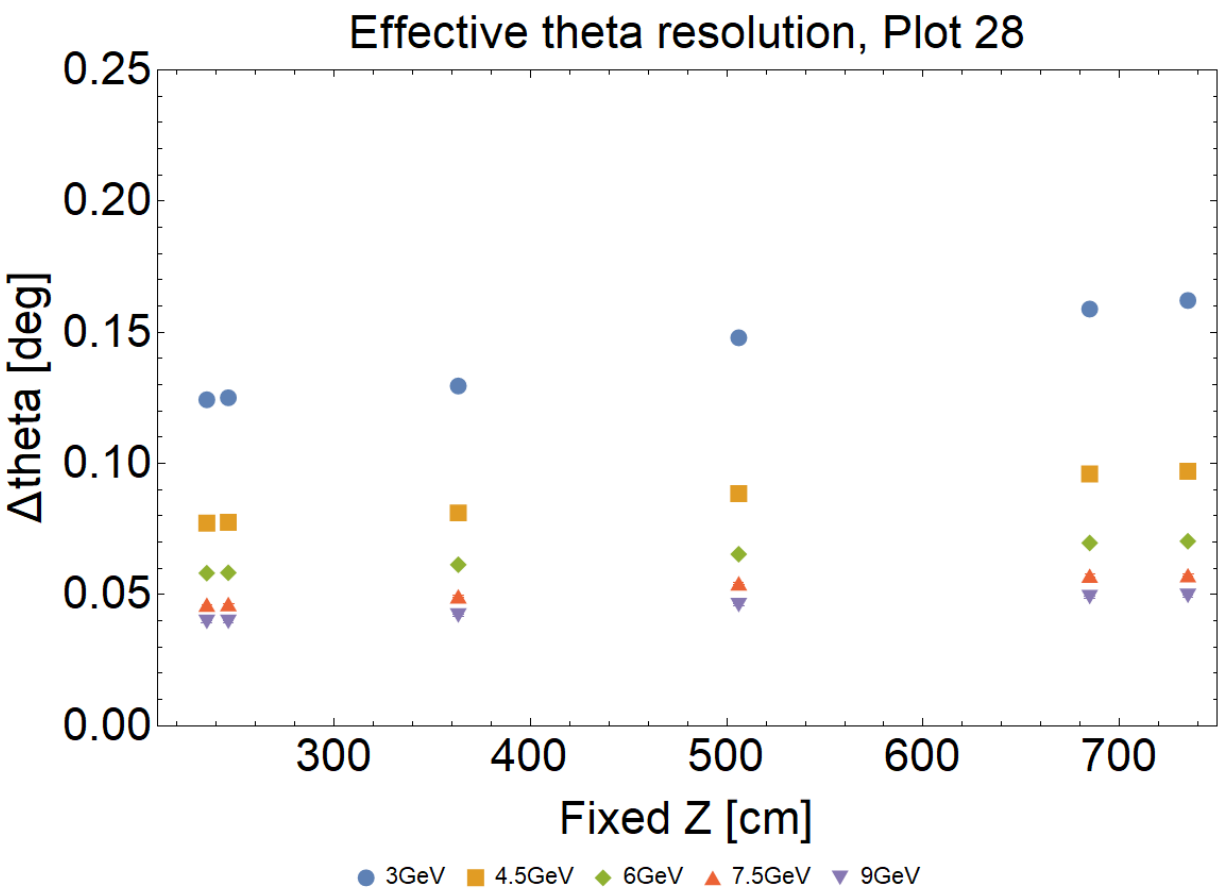
Effective theta resolution, Plot 28
Δtheta [deg]
0.25
0.20
0.15
0.10
0.05
0.00
300
400
500
600
700
Fixed Z [cm]
3GeV
4.5GeV
6GeV
7.5GeV
9GeV

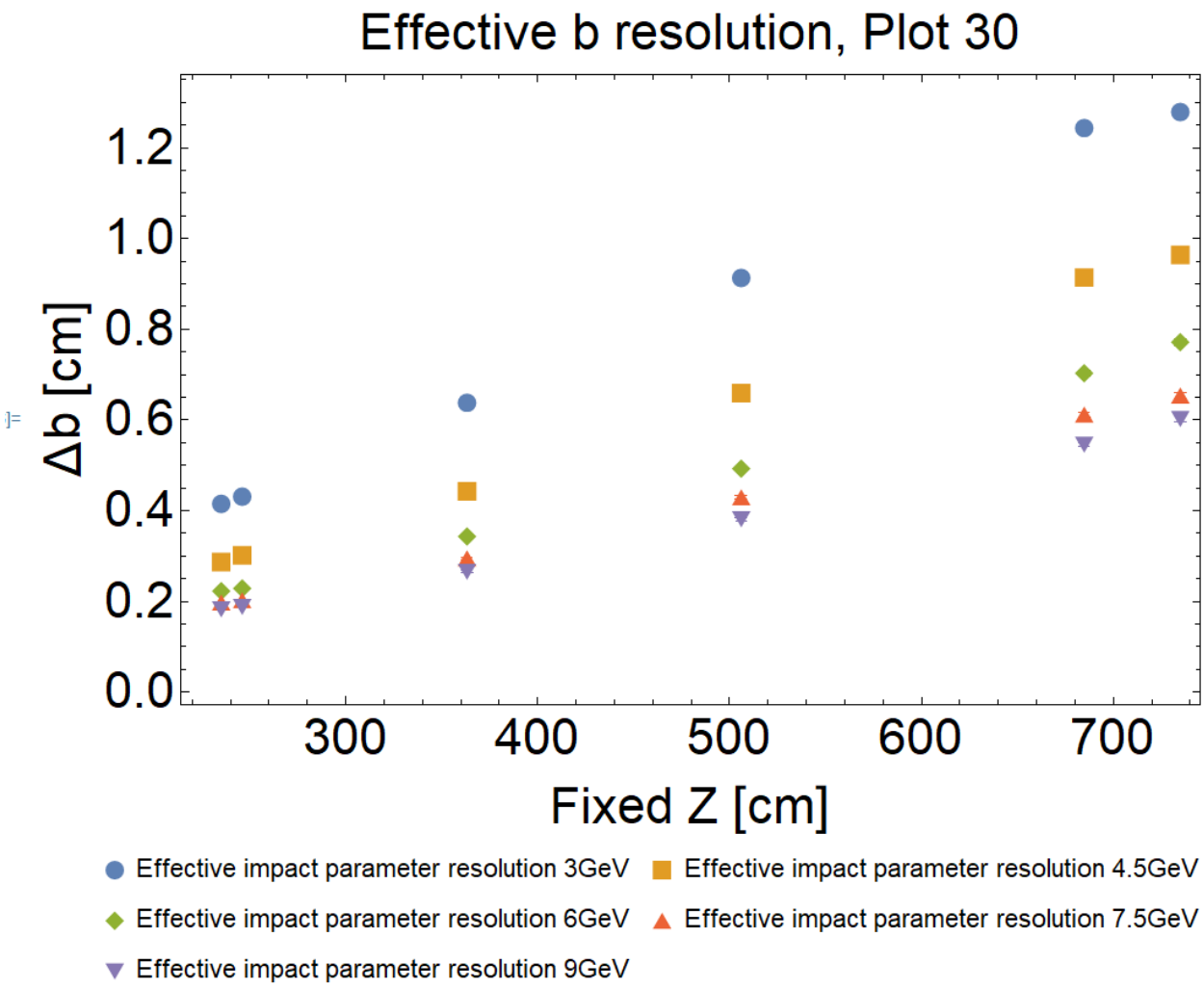
Effective b resolution, Plot 30
Δb [cm]
1.2
1.0
0.8
0.6
0.4
0.2
0.0
300
400
500
600
700
Fixed Z [cm]
Effective impact parameter resolution 3GeV
Effective impact parameter resolution 4.5GeV
Effective impact parameter resolution 6GeV
Effective impact parameter resolution 7.5GeV
Effective impact parameter resolution 9GeV

B.6 Plots of Events Created with Different Detector Geometries

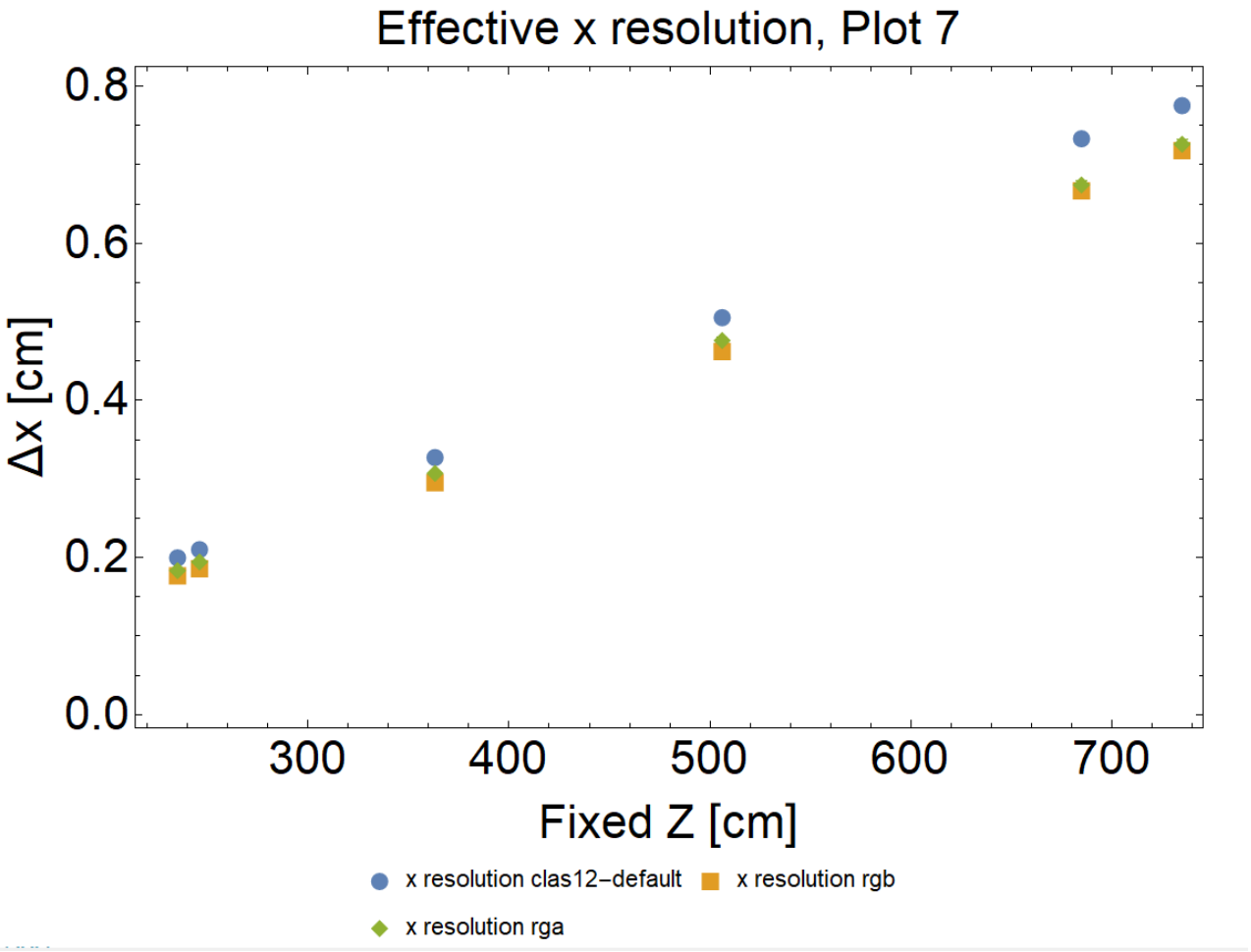

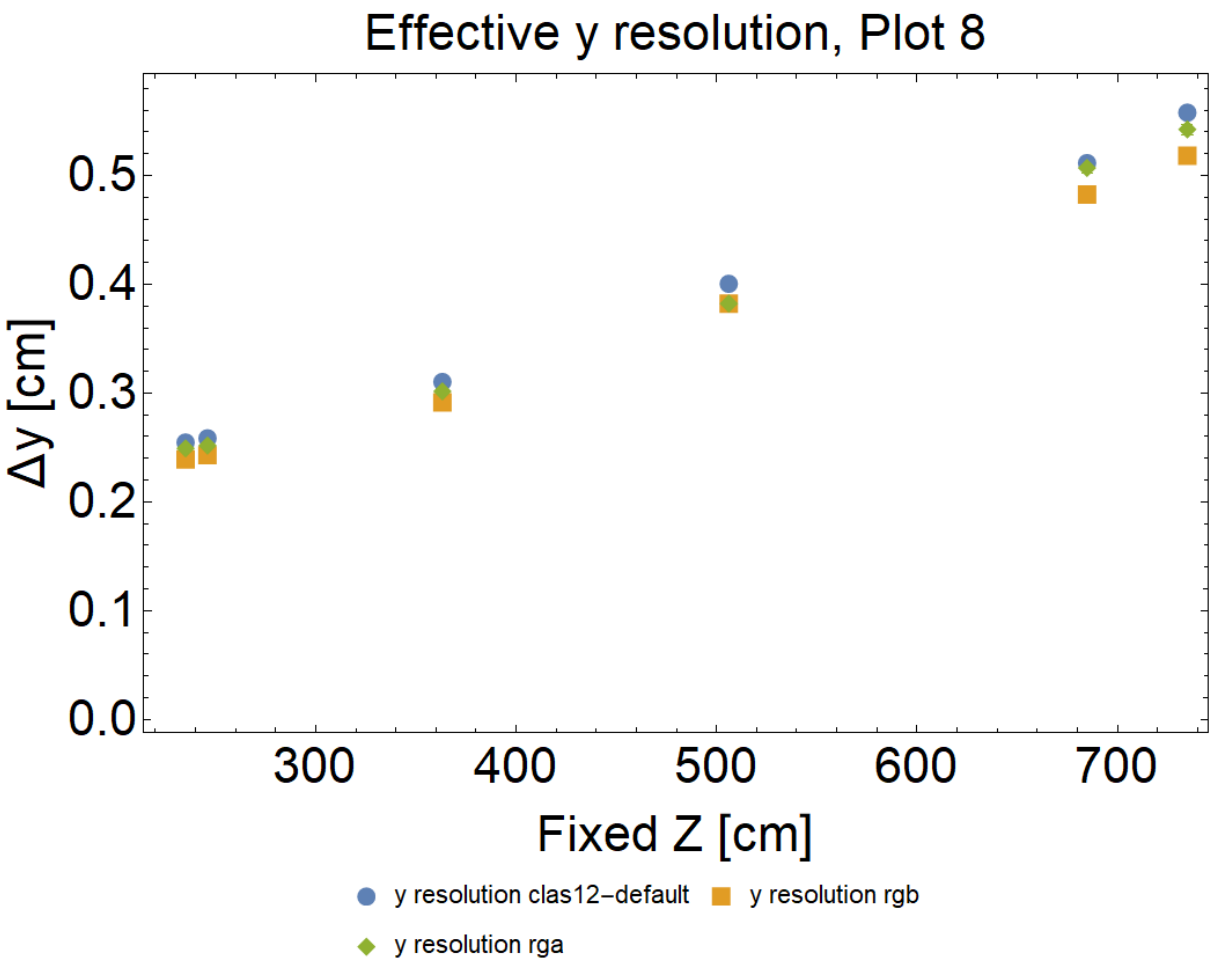
Effective y resolution, Plot 8
Δy [cm]
0.0
0.1
0.2
0.3
0.4
0.5
300
400
500
600
700
Fixed Z [cm]
y resolution clas12−default
y resolution rgb
y resolution rga

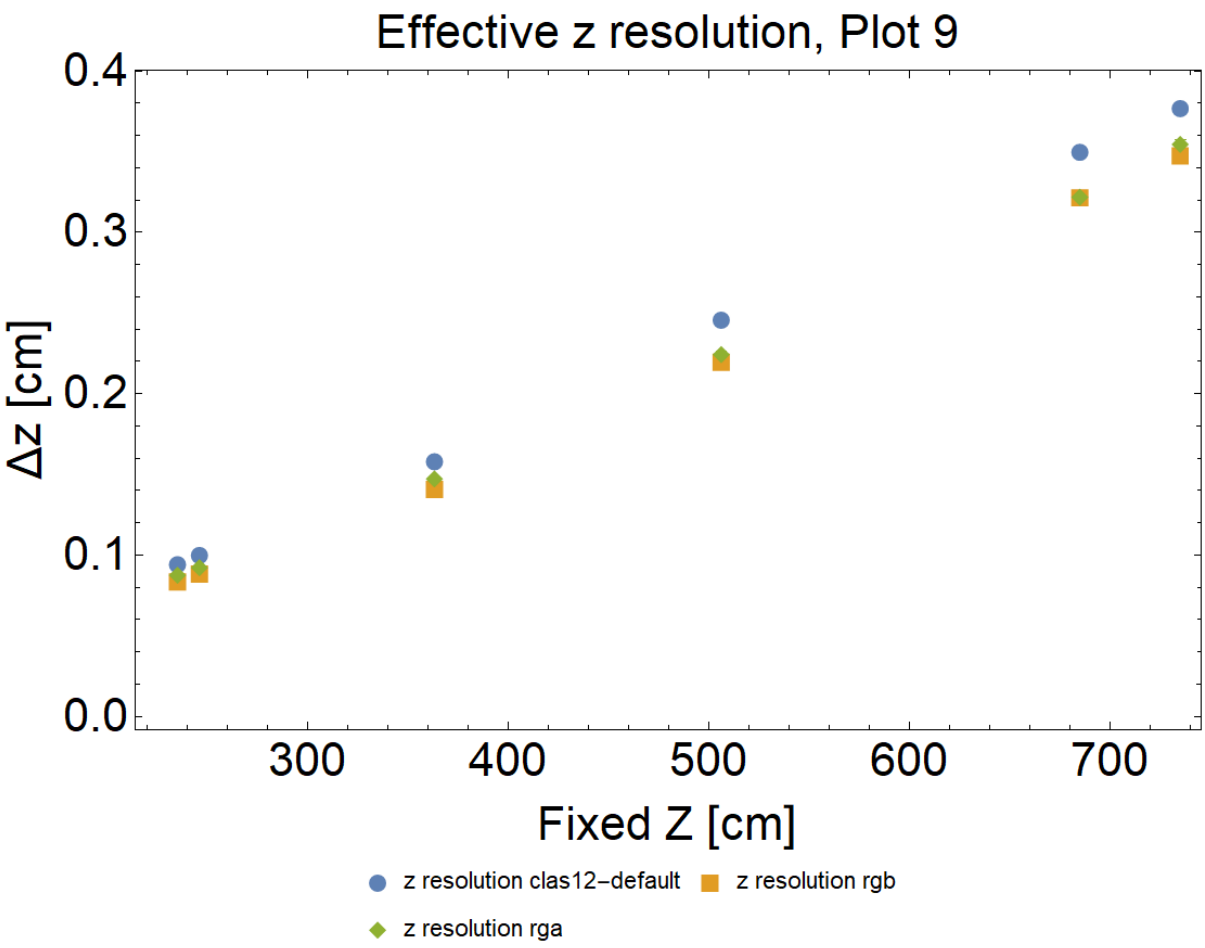
Effective z resolution, Plot 9
0.4
0.3
0.2
0.1
0.0
Δz [cm]
300
400
500
600
700
Fixed Z [cm]
z resolution clas12−default
z resolution rgb
z resolution rga

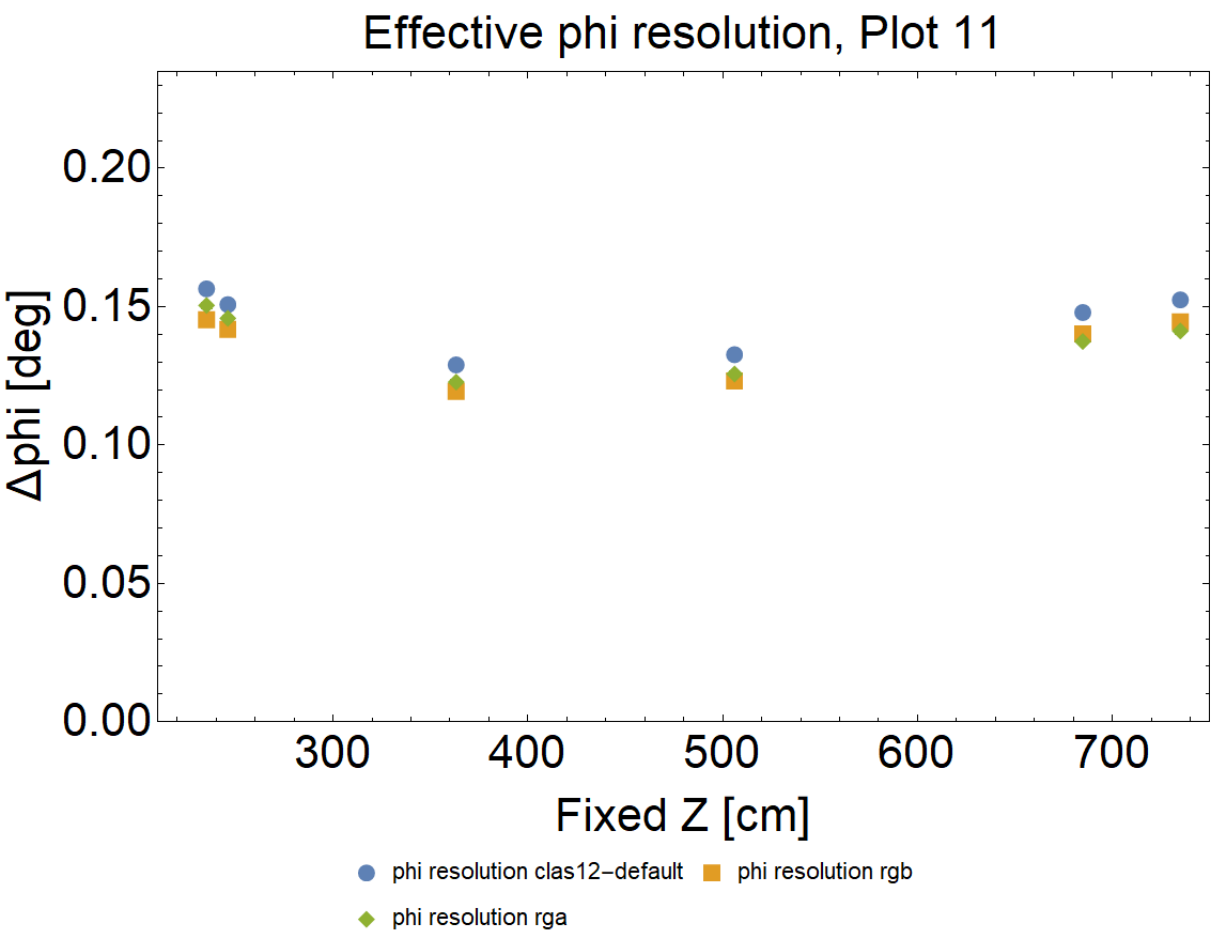
Effective phi resolution, Plot 11
Δphi [deg]
0.20
0.15
0.10
0.05
0.00
300
400
500
600
700
Fixed Z [cm]
phi resolution clas12−default
phi resolution rgb
phi resolution rga

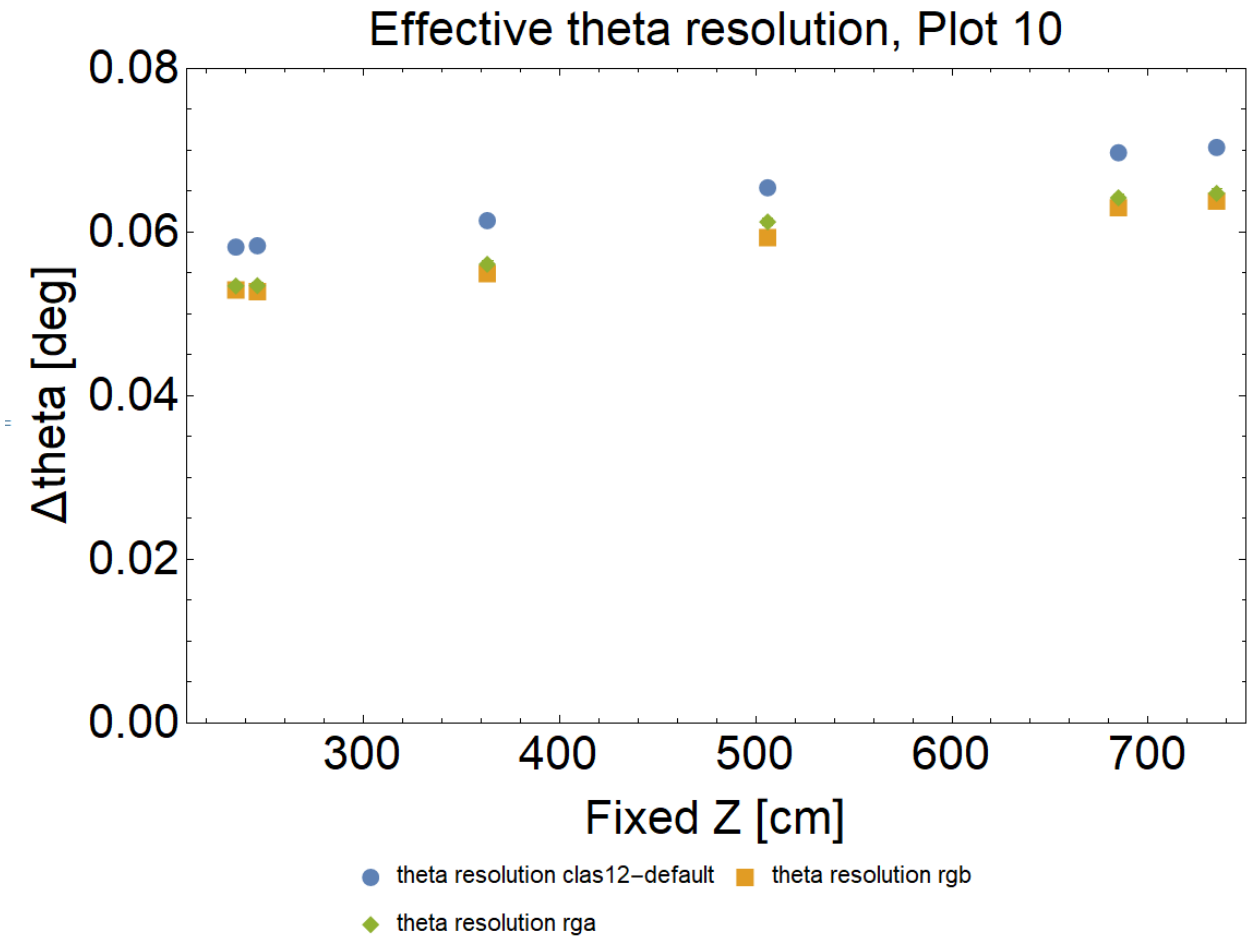
Effective theta resolution, Plot 10
0.08
0.06
0.04
0.02
0.00
Δtheta [deg]
300
400
500
600
700
Fixed Z [cm]
theta resolution clas12−default
theta resolution rgb
theta resolution rga

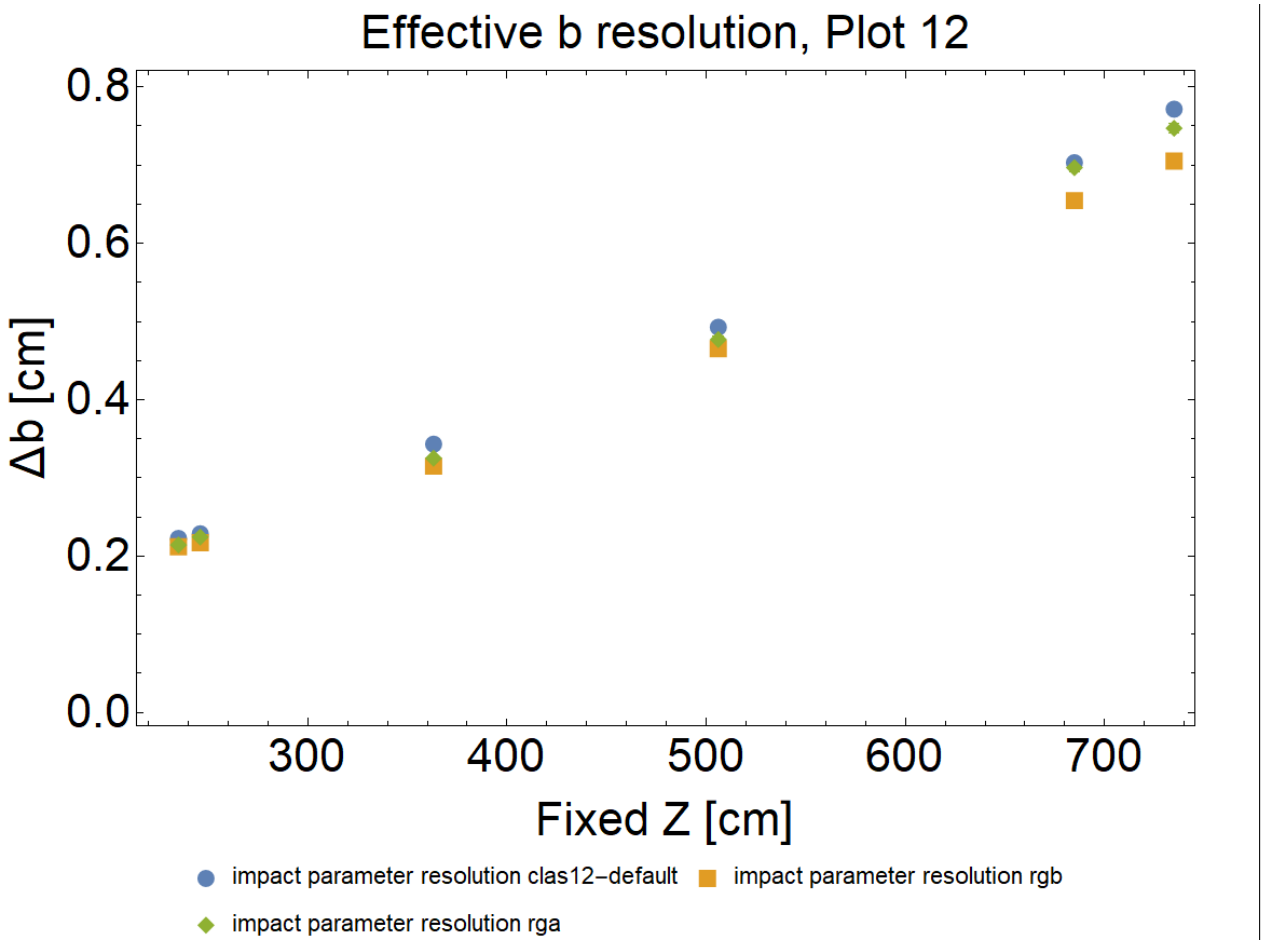
Effective b resolution, Plot 12
0.8
0.6
0.4
0.2
0.0
Δb [cm]
300
400
500
600
700
Fixed Z [cm]
impact parameter resolution clas12−default
impact parameter resolution rgb
impact parameter resolution rga

B.7 Plots of Events Created with a Reversed Torus Polarity

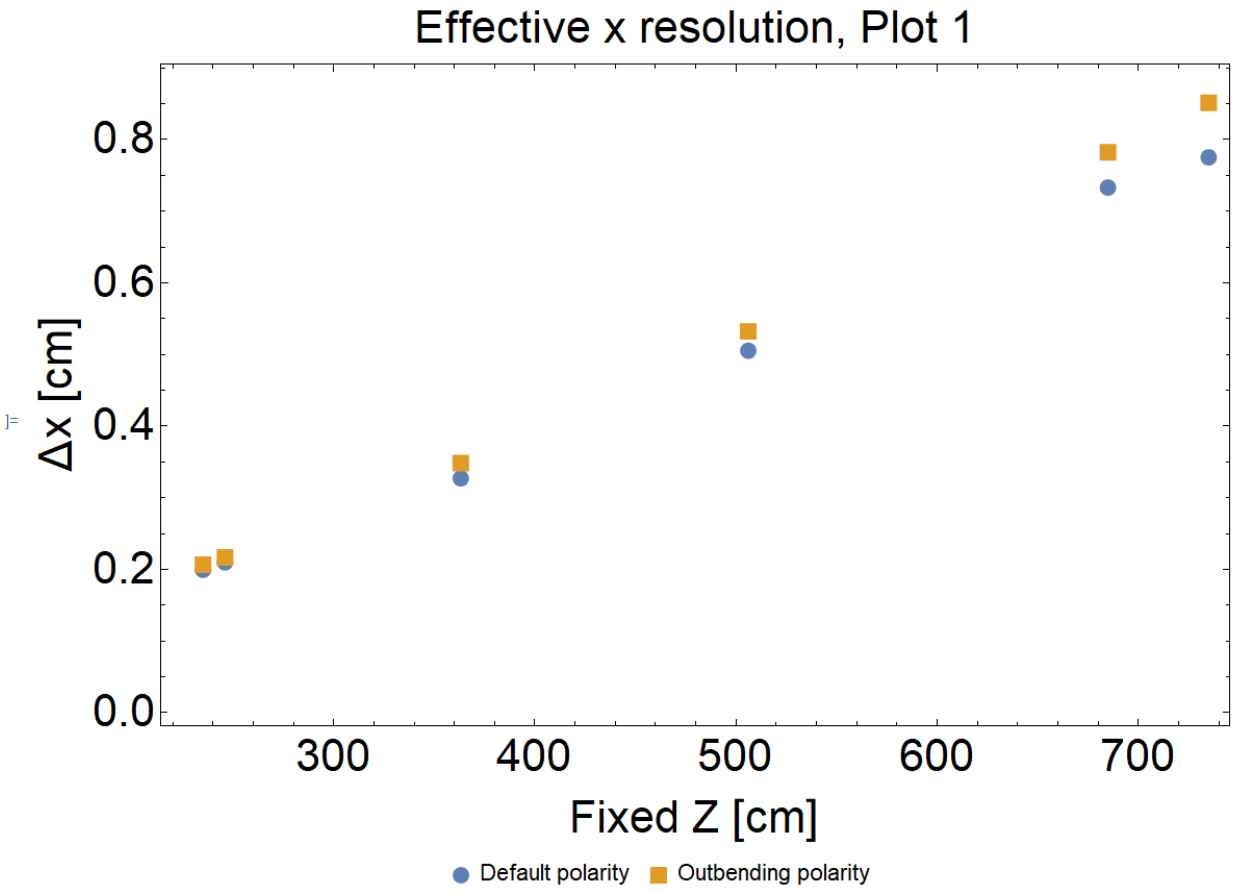

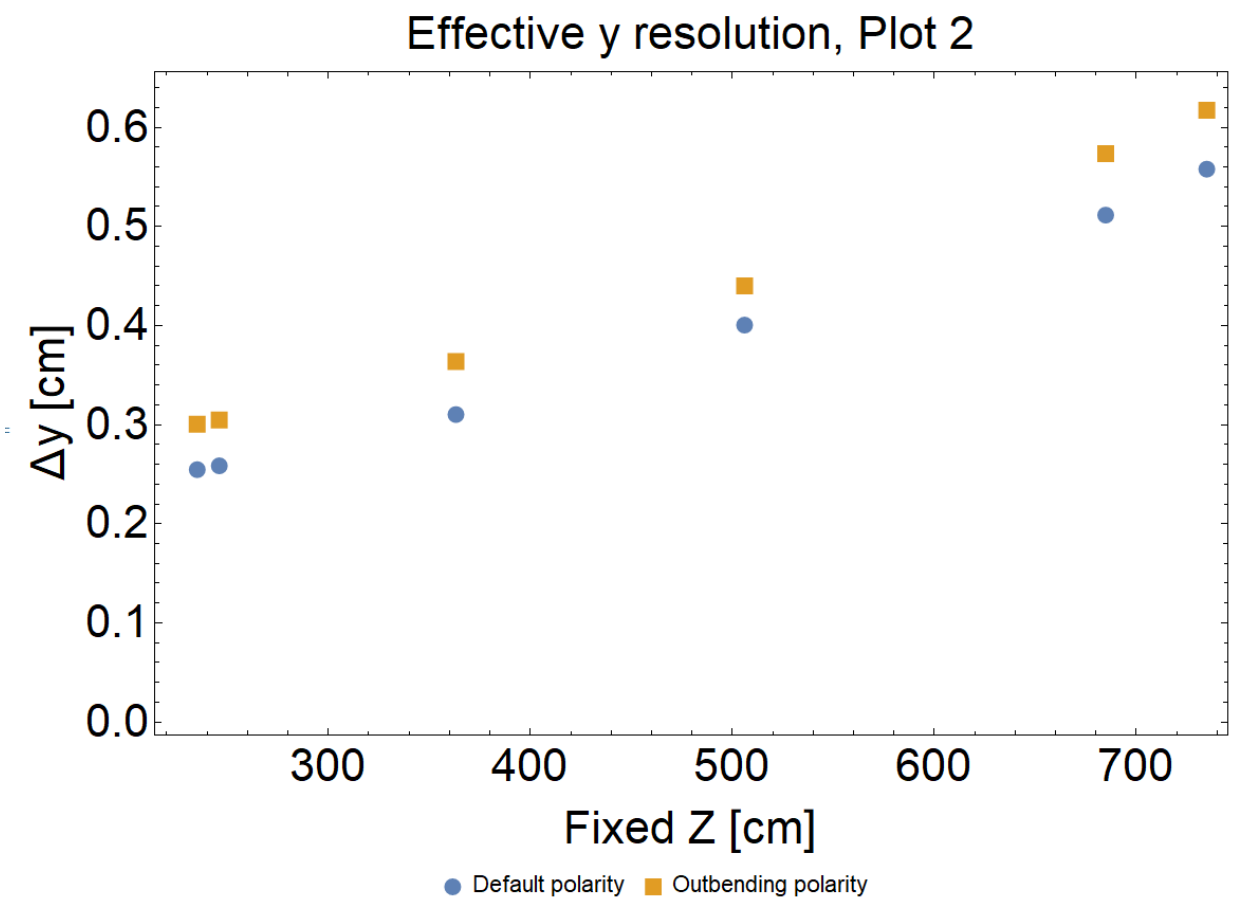
Effective y resolution, Plot 2
Δy [cm]
0.0
0.1
0.2
0.3
0.4
0.5
0.6
300
400
500
600
700
Fixed Z [cm]
Default polarity
Outbending polarity

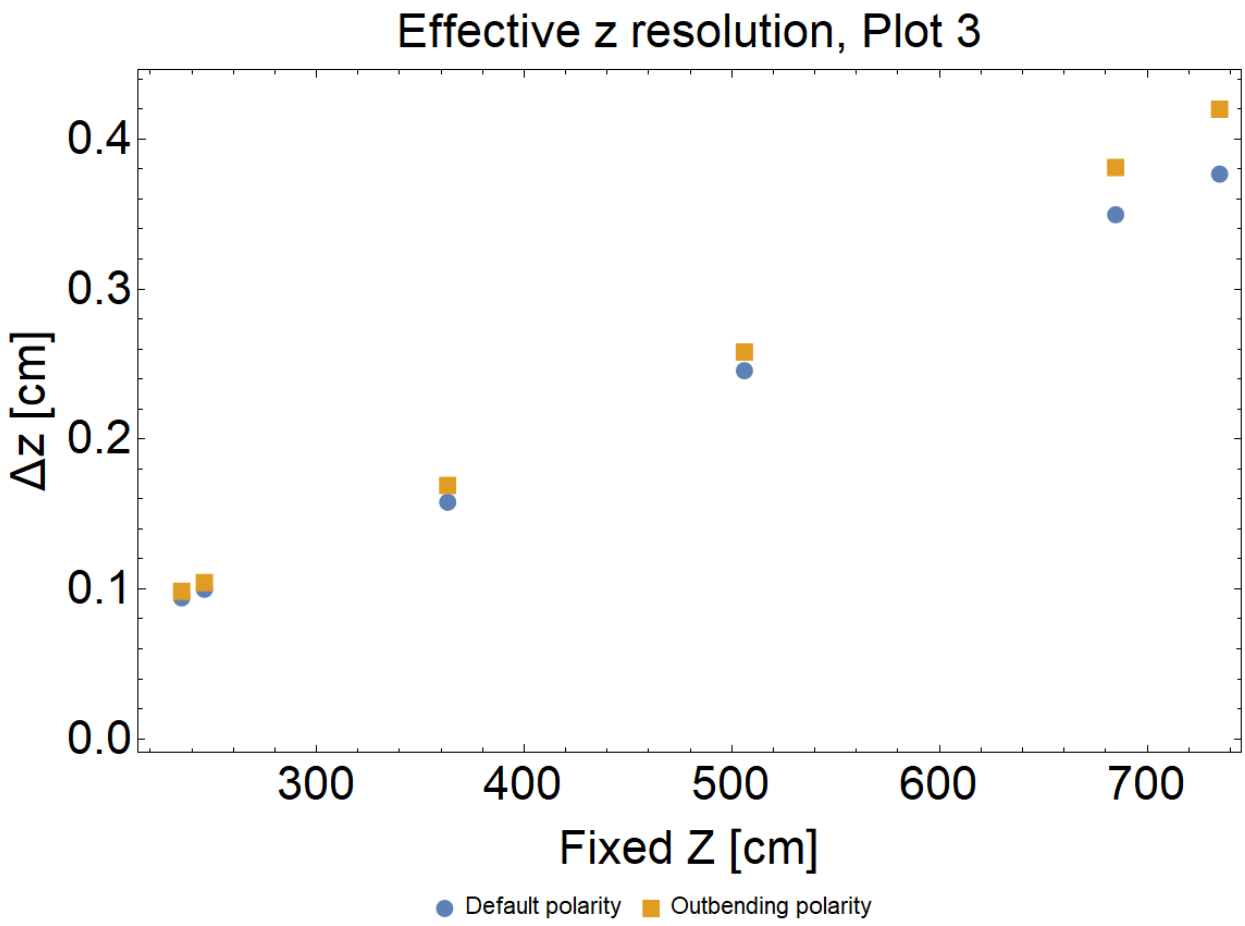
Effective z resolution, Plot 3
Δz [cm]
0.0
0.1
0.2
0.3
0.4
300
400
500
600
700
Fixed Z [cm]
Default polarity
Outbending polarity

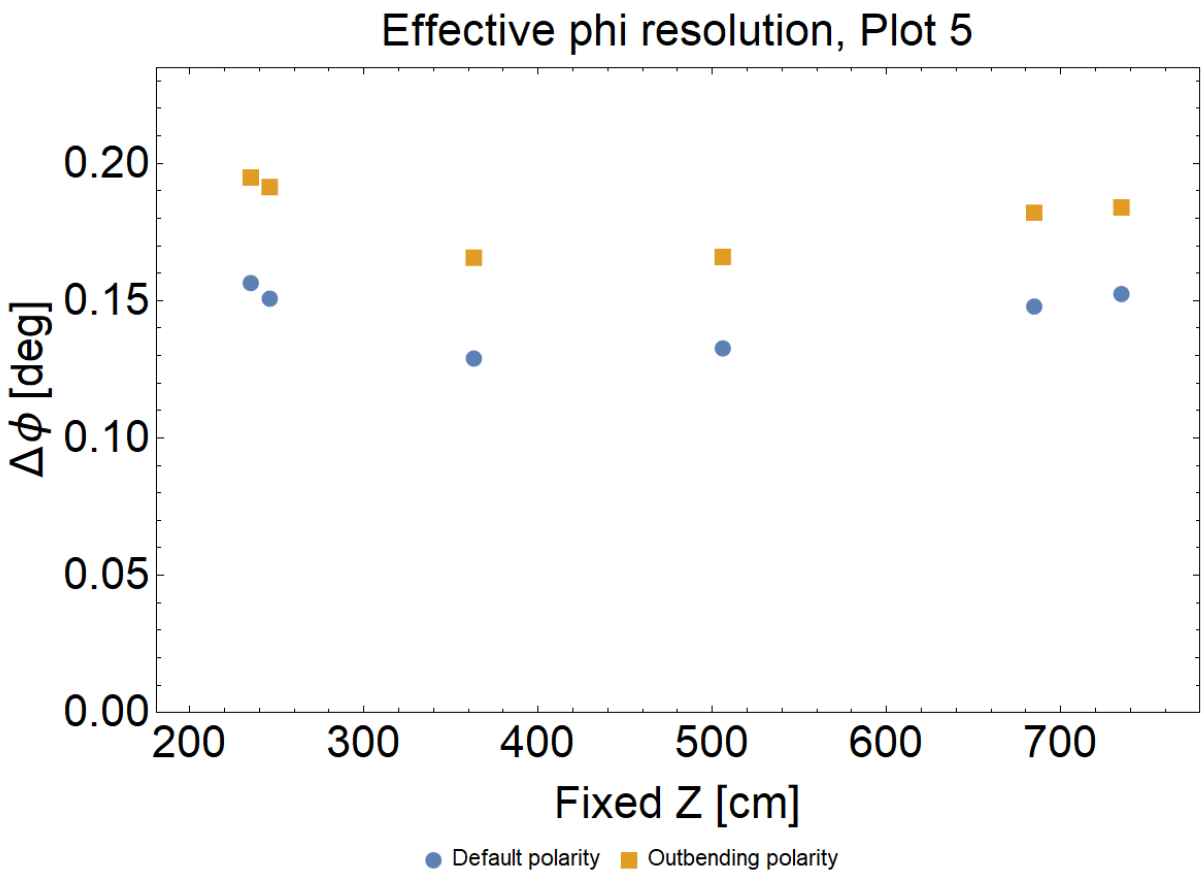
Effective phi resolution, Plot 5
0.20
0.15
0.10
0.05
0.00
Δϕ [deg]
200
300
400
500
600
700
Fixed Z [cm]
Default polarity
Outbending polarity

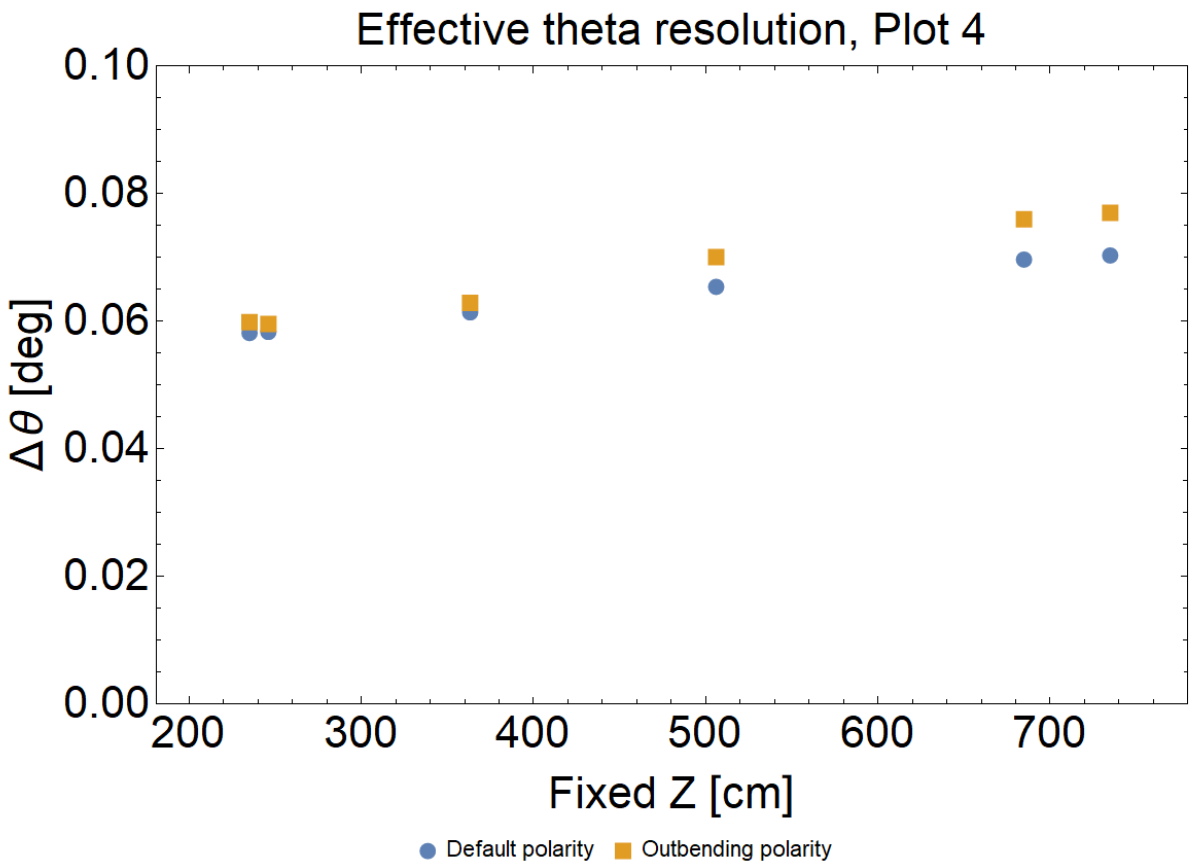
Effective theta resolution, Plot 4
0.10
0.08
0.06
0.04
0.02
0.00
Δθ [deg]
200
300
400
500
600
700
Fixed Z [cm]
Default polarity
Outbending polarity

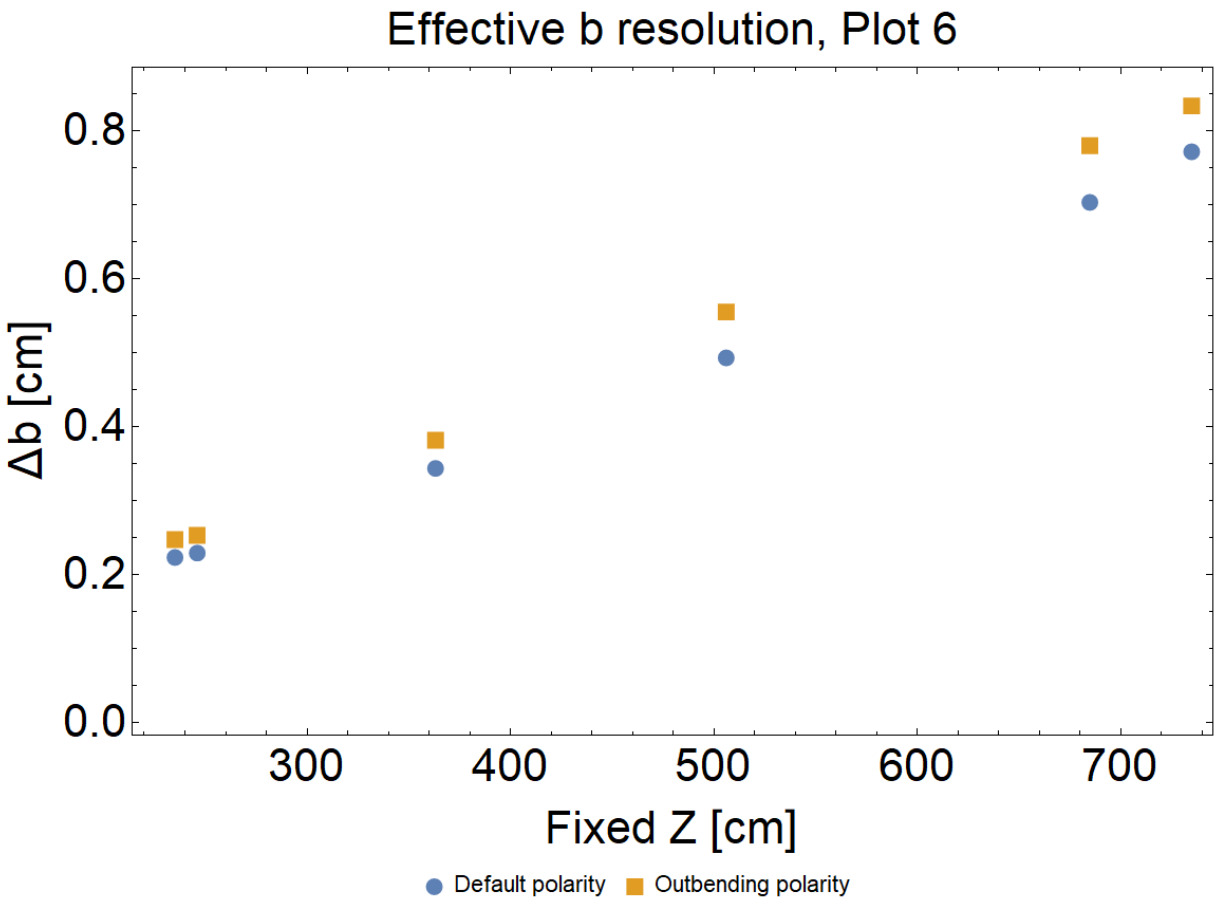
Effective b resolution, Plot 6
Δb [cm]
0.0
0.2
0.4
0.6
0.8
300
400
500
600
700
Fixed Z [cm]
Default polarity
Outbending polarity

B.8 Plots of Events with Merged Beam Background Files

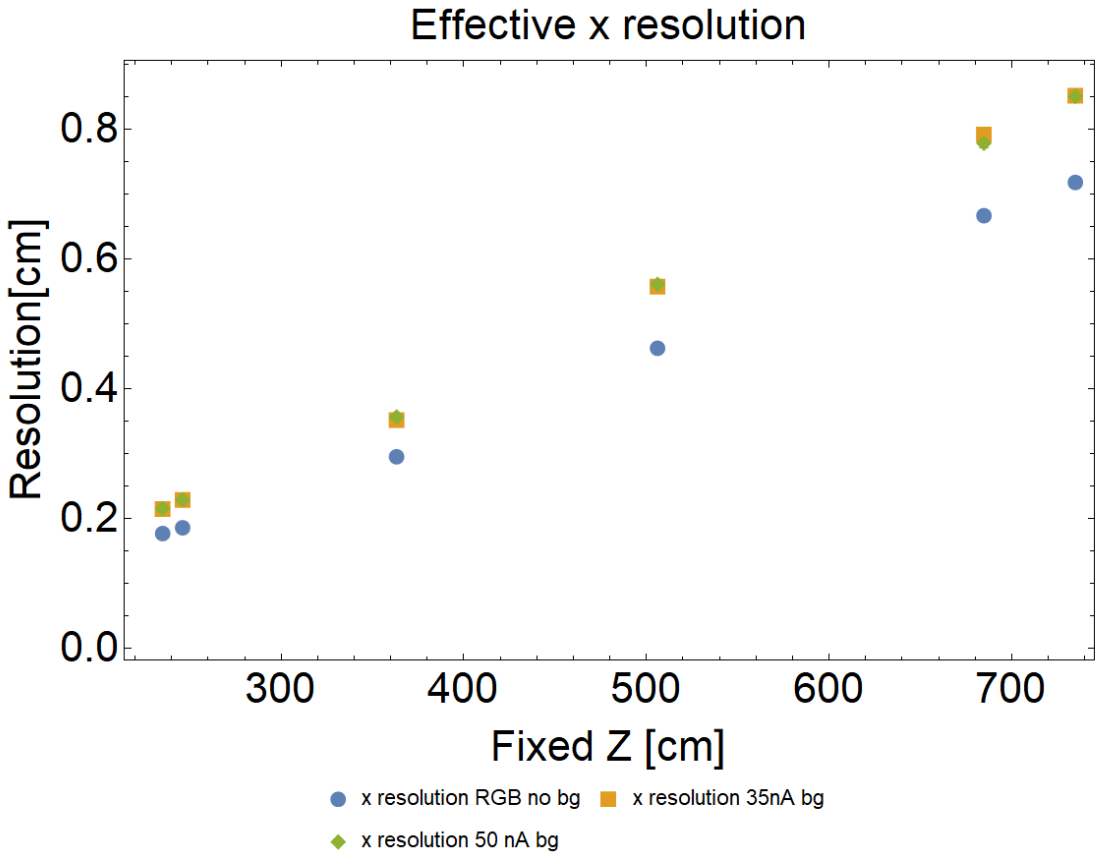

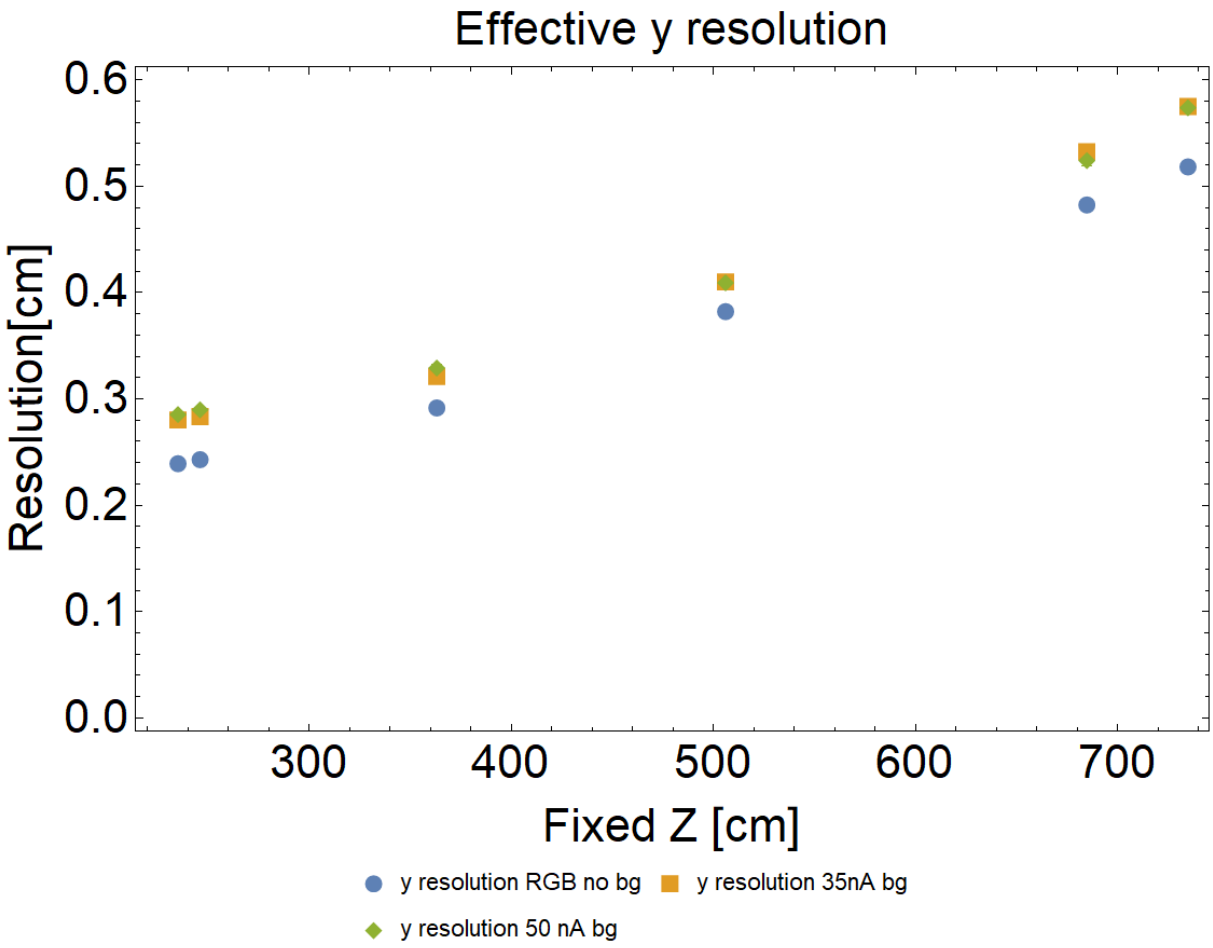
Effective y resolution
Resolution[cm]
0.0
0.1
0.2
0.3
0.4
0.5
0.6
300
400
500
600
700
Fixed Z [cm]
y resolution RGB no bg
y resolution 35nA bg
y resolution 50 nA bg

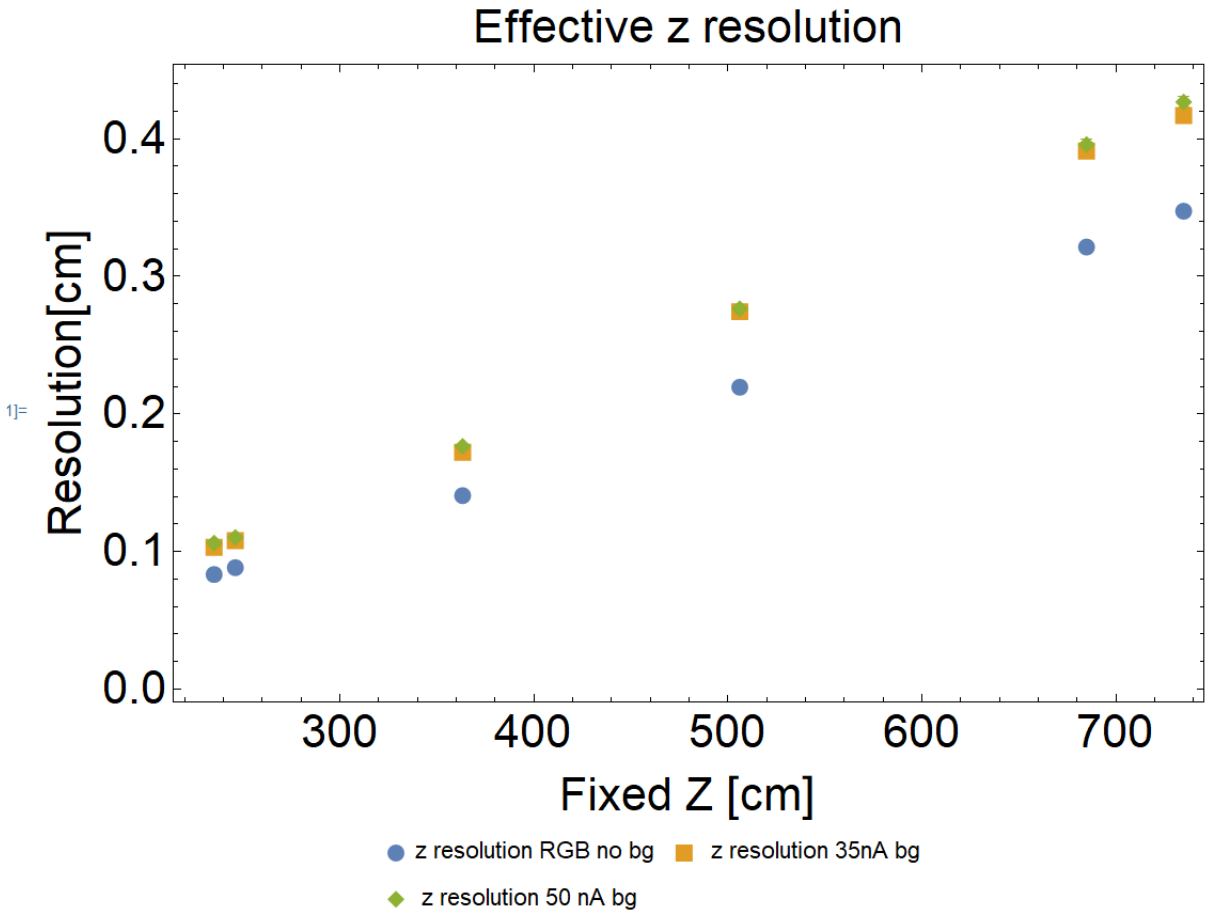
Effective z resolution
Resolution[cm]
0.0
0.1
0.2
0.3
0.4
300
400
500
600
700
Fixed Z [cm]
z resolution RGB no bg
z resolution 35nA bg
z resolution 50 nA bg

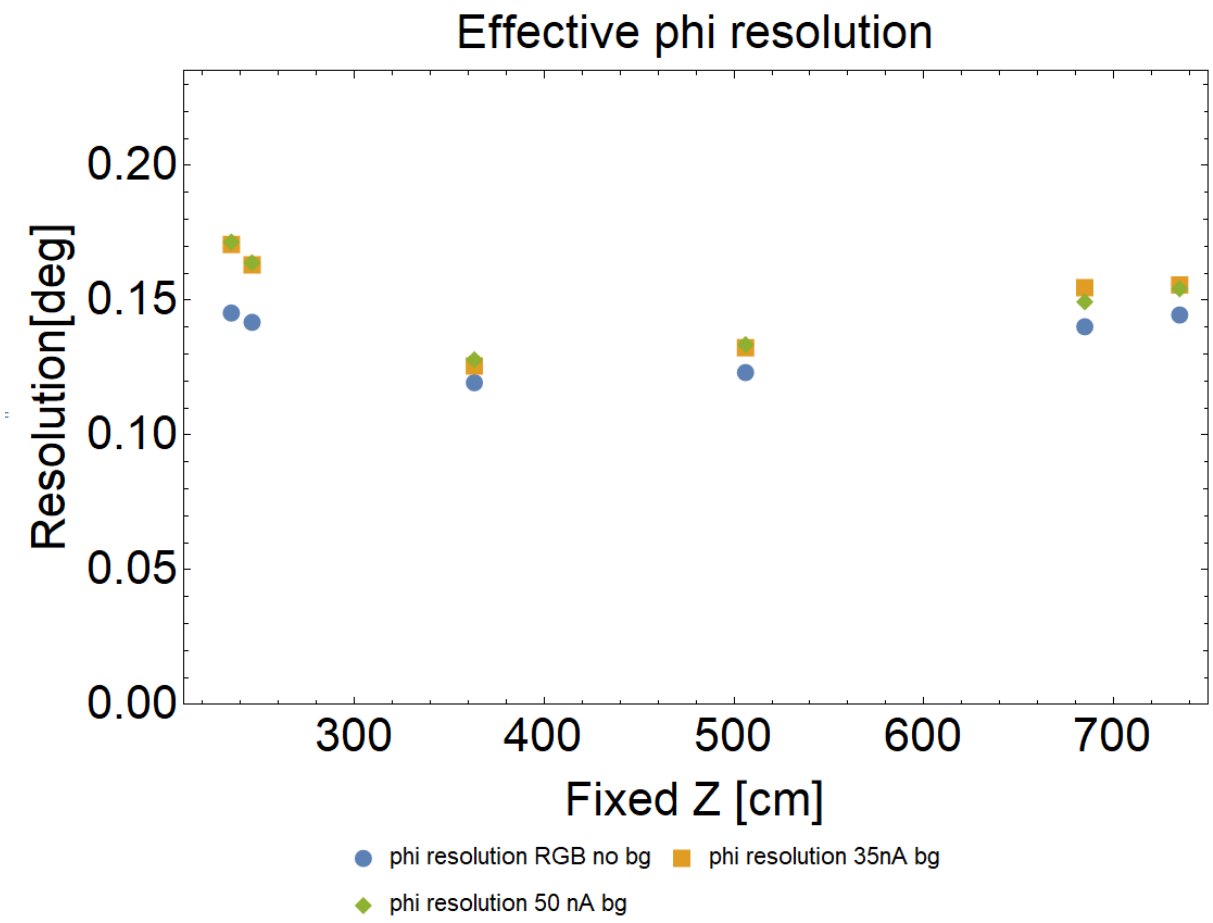
Effective phi resolution
Resolution[deg]
0.20
0.15
0.10
0.05
0.00
300
400
500
600
700
Fixed Z [cm]
phi resolution RGB no bg
phi resolution 35nA bg
phi resolution 50 nA bg

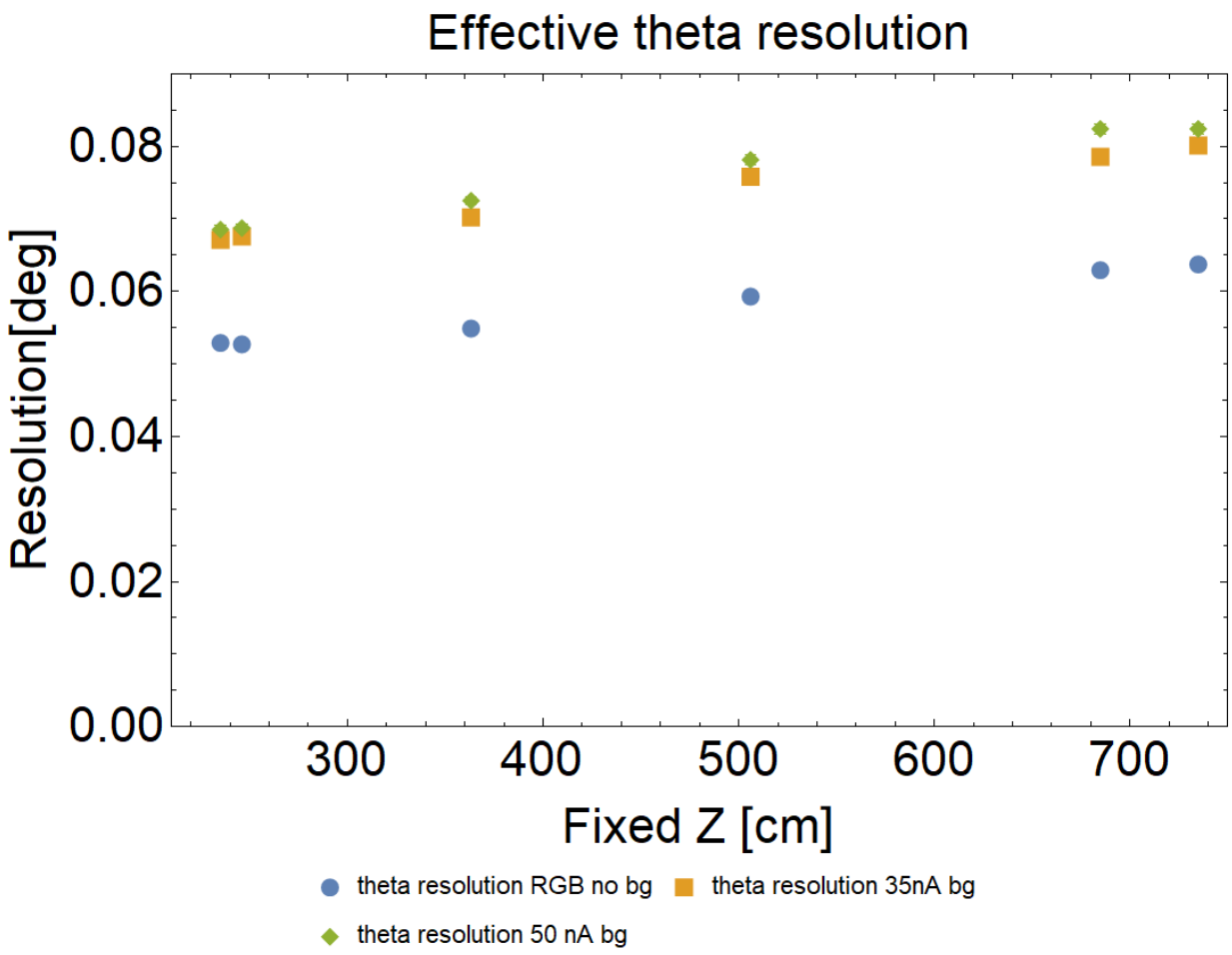
Effective theta resolution
Resolution[deg]
0.00
0.02
0.04
0.06
0.08
300
400
500
600
700
Fixed Z [cm]
theta resolution RGB no bg
theta resolution 35nA bg
theta resolution 50 nA bg

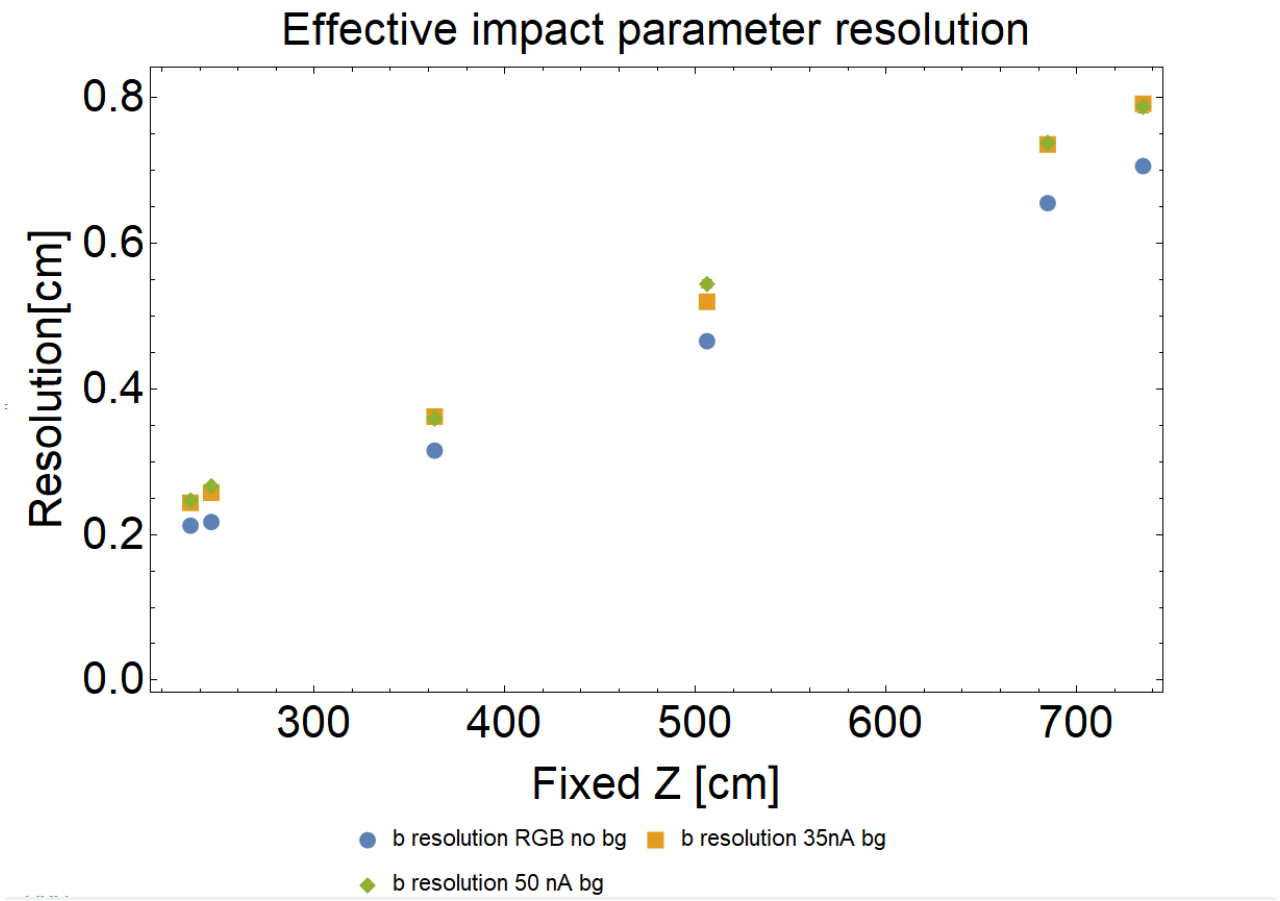
Effective impact parameter resolution
Resolution[cm]
0.0
0.2
0.4
0.6
0.8
300
400
500
600
700
Fixed Z [cm]
b resolution RGB no bg
b resolution 35nA bg
b resolution 50 nA bg